

Divergence-Free Diffusion Models for Incompressible Fluid Flows

Wilfried Genuist^{a,b}, Éric Savin^a, Filippo Gatti^b, Didier Clouteau^b

^aDTIS, ONERA, Université Paris-Saclay, Palaiseau, 91120, France

^bLMPS-Laboratoire de Mécanique Paris-Saclay, Université Paris-Saclay, ENS Paris-Saclay, CentraleSupélec, CNRS, Gif-sur-Yvette, 91190, France

Abstract

Generative diffusion models are extensively used in unsupervised and self-supervised machine learning with the aim to generate new samples from a probability distribution estimated with a set of known samples. They have demonstrated impressive results in replicating dense, real-world contents such as images, musical pieces, or human languages. This work investigates their application to the numerical simulation of incompressible fluid flows, with a view toward incorporating physical constraints such as incompressibility in the probabilistic forecasting framework enabled by generative networks. For that purpose, we explore different conditional, score-based diffusion models where the divergence-free constraint is imposed by the Leray spectral projector, and autoregressive conditioning is aimed at stabilizing the forecasted flow snapshots at distant time horizons. The proposed models are run on a benchmark turbulence problem, namely a Kolmogorov flow, which allows for a fairly detailed analytical and numerical treatment and thus simplifies the evaluation of the numerical methods used to simulate it. Numerical experiments of increasing complexity are performed in order to compare the advantages and limitations of the diffusion models we have implemented and appraise their performances, including: (i) in-distribution assessment over the same time horizons and for similar physical conditions as the ones seen during training; (ii) rollout predictions over time horizons unseen during training; and (iii) out-of-distribution tests for forecasting flows markedly different from those seen during training. In particular, these results illustrate the ability of diffusion models to reproduce the main statistical characteristics of Kolmogorov turbulence in scenarios departing from the ones they were trained on.

Keywords: Computational fluid dynamics, Kolmogorov flow, Scientific machine learning, Diffusion models, Score-based generative models, Stochastic differential equations.

1. Introduction

1.1. Context and aim of the paper

This research is concerned with the construction of numerical solutions \mathbf{u}^* of the incompressible Navier-Stokes Equations (NSE) given some input parameters ξ^* , namely find \mathbf{u}^* such that:

$$\mathbf{u}^* = \text{NSE}(\xi^*). \quad (1)$$

The parameters ξ^* are the initial conditions, the boundary conditions, the viscosity, the external forcing, the friction coefficient if any, *etc...* We must stress at the outset that no rigorous mathematical definition exists so far of what “solutions” of Navier-Stokes equations could be, since the problem of “solving” the latter remains broadly open [1, 2]. The main known results for three-dimensional flows are that weak solutions of finite energy exist for all times but may not be unique. On the other hand, strong solutions of finite enstrophy are unique but exist only for short times; see for example [3] for a recent account on these fundamental topics. Now beyond those theoretical considerations, and for the purpose of obtaining numerical solutions satisfying (or approximating) (1), we may have access to different types of data:

- A set of S input parameters $\{\xi_s\}_{s=1}^S$: then Eq. (1) may be solved for each ξ_s by classical numerical methods in computational fluid dynamics (CFD) [4, 5, 6] and reduced basis methods [7], for example, may be used to obtain \mathbf{u}^* for new input parameters ξ^* .
- Input parameters are random with a known probability measure μ_{in} on a suitable probability space: then one may construct the pushforward measure of the solutions of (1) and sample from it, given the input parameters $\xi^* \sim \mu_{\text{in}}$, or resort to collocation or spectral methods such as the polynomial chaos expansion [8], for example. The formulation of Navier-Stokes equations as stochastic differential equations with random driving forces has also relevance in various engineering and geo-physical applications, among others. From a mathematical point of view, this formulation allows to prove properties such as the continuous dependence on initial data or the convergence to equilibrium; see *e.g.* [9] and references therein.
- A set of S input-output observations $\{\xi_s, \mathbf{u}_s\}_{s=1}^S$: this is a supervised learning framework, as widely adopted in scientific machine learning [10]. It has been addressed by numerous authors using *e.g.*, Gaussian process regression [11], physics-informed neural networks [12, 13], or operator networks [14, 15, 16, 17], to name only a few of the recent advances in this direction. In this regard, CFD has benefited from the important developments in high-performance computing and experimental measurement capabilities achieved in the last decades, resulting in ever increasing volumes of data for data-driven problem solving approaches [18, 19].
- A set of S output observations $\{\mathbf{u}_s\}_{s=1}^S$: this is an unsupervised learning framework, where the objective is to infer \mathbf{u}^* following the very probability distribution of which these observations are assumed to be known samples. Generative adversarial networks (GANs) [20], variational auto-encoders (VAEs) [21], or denoising diffusion probabilistic models (DDPMs) [22, 23],

among others, aim at computing and sampling complex, multi-modal and possibly conditional distributions on (very) high-dimensional sets. Unsupervised problems actually need to be somehow conditioned to be solved, so that they become supervised. The aforementioned generative models for example train themselves after initialization with labeled training data, and are thus coined self-supervised. Extracting lower-dimensional representations from experimental data and large-scale simulations is another way of learning flow features that may be mapped back to the higher-dimensional set of actual flows in order to infer new realizations thereof. Proper orthogonal decomposition, or principal component analysis, was for example introduced in the context of turbulence in [24].

The aim of the paper is to address (1) from the perspective of self-supervised learning using autoregressive diffusion models. In the continuation of earlier work in [25], past predictions from generative diffusion networks are used to condition the inference of solutions at future time steps—hence the terminology autoregressive from *e.g.* [26]. The issue of how to account for physical constraints in diffusion models is further addressed. Incompressible flows with divergence-free velocity fields are more particularly considered.

1.2. Related works

The rapid growth in computational power and advances in theoretical and numerical analysis have made accurate fluid mechanics simulation a central challenge in modern science and engineering. For a long time, this challenge has been addressed with CFD, which relies on the numerical solution of the governing Partial Differential Equations (PDE) using finite difference, finite volume, or spectral discretizations, enabling high-fidelity approaches such as Direct Numerical Simulation (DNS) and reduced-cost strategies as Large Eddy Simulation (LES) [4, 5, 6, 27, 28]. While these methods provide strong theoretical guarantees and physical interpretability, their high computational cost and limited scalability have driven the rise of physics-based machine learning, or scientific machine learning, as a complementary paradigm [18, 19, 29, 30, 31]. By embedding physical principles, conservation laws, and PDE structure directly into the learning or generative pipeline, scientific machine learning aims to preserve the underlying physics and interpretability while lowering the computational cost of classical solvers through statical patterns, offering new pathways for efficient, data-informed fluid flow prediction and analysis.

While several existing machine learning approaches aim for a unified modeling frameworks that jointly encode physical constraints and inference, such formulations can become restrictive or difficult to scale for high-dimensional data [13, 32]. In contrast, diffusion and score-based generative models [22, 23, 33] offer a flexible probabilistic alternative, particularly well suited to learning high-dimensional distributions and enabling conditional generation under uncertainty. Their foundations trace back to the interpretation of generative modeling as a thermodynamic process, where data are progressively corrupted by noise and subsequently reconstructed by reversing the diffusion dynamics [22]. This perspective was made practical by denoising diffusion probabilistic models [23], which introduced a simple discrete-time objective that scales to high-dimensional data while maintaining excellent sample quality [34, 35]. In parallel, score-based modeling reframed generation as learning the gradient of the log-density (*i.e.* the score-function) via denoising score-matching [36], later unified with diffusion models through continuous-time Stochastic Differential Equations (SDE) [33]. This unification clarified that diffusion models admit both stochastic reverse-time dynamics, grounded in classical results on reverse diffusion [37, 38], and deterministic probability flow Ordinary Differential Equations (ODE), enabling accurate log-likelihood computation and flexible sampling trade-offs [35, 39, 40]. Novel work has substantially improved the efficiency, stability, and controllability of diffusion models. Variational formulations recast diffusion as latent-variable models with learnable noise schedules [41], while improved parameterizations and noise discretizations have led to better likelihoods and higher-fidelity samples [42]. Conditioning strategies such as classifier-free guidance [43] enable conditional generation using a single model, eliminating the need for separately trained classifiers. A broad range of alternative conditional generation techniques has since been explored (see *e.g.* [26, 44]). Other works have pursued key design choices, including samplers and noise schedules, and have shown that many empirical improvements arise from theoretical considerations rather than from architectural novelty alone [40]. Finally, acceleration methods such as implicit sampling [35], progressive distillation [45], and consistency-based training [46] further reduce inference cost, often at the expense of theoretical guarantees.

Beyond mere sample generation, diffusion models have been extended to sequential and temporal data, where output consistency is crucial. Early adaptations introduced conditional diffusion for time-series forecasting, explicitly modeling uncertainty over missing values [47, 48]. Autoregressive diffusion models demonstrated that diffusion can be integrated into sequential forecasting pipelines, capturing complex temporal dependencies while retaining probabilistic outputs [25, 26, 44, 49]. In parallel, diffusion models have been increasingly interpreted through the lens of stochastic control and optimal transport. Schrödinger bridge formulations connect diffusion training to entropy-regularized transport between data and noise distributions, providing a formal framework for conditional generation, interpolation, and control [50]. These ideas underpin modern approaches to inverse problems and extend beyond temporal modeling. Furthermore, score-based posterior sampling enables efficient reconstruction without retraining, extending diffusion models to ill-posed inverse problems with strong empirical performance [51, 52]. While recent work has begun to establish robustness guarantees [53], conditional time-series diffusion models often lack explicit enforcement of governing physical laws and flexible architecture.

The relevance of diffusion models to physics-based systems has therefore attracted growing attention, particularly for complex dynamical systems governed by PDEs. In fluid mechanics and geophysical forecasting, operator learning methods such as Fourier Neural Operators and large-scale graph-based models have demonstrated impressive predictive skills at unprecedented scales [54, 55, 56, 57]. However, these approaches are fundamentally deterministic and may struggle to represent uncertainty, multi-modality, and rare events contrary to diffusion models. Recent work has shown that diffusion can generate high-fidelity turbulent flows and perform super-resolution by leveraging spectral decompositions and multi-scale priors [58, 59]. Autoregressive conditional diffusion models have further enabled long-horizon flow simulation, but stability, error accumulation, and physical consistency remain open challenges [26, 44]. To address these issues, several physics-informed diffusion models incorporate PDE constraints either during training or sampling. Approaches such as Pi-Fusion and residual diffusion enforce physics through soft penalties or corrective steps [60, 61]. While these methods improve physical plausibility, they typically rely on approximate enforcement and do not guarantee exact conservation laws. This limitation echoes broader challenges in physics-informed machine learning, where soft constraints can lead to optimization stiffness and poor generalization [32, 62].

A broad and complementary line of research seeks to improve learning efficiency and stability by embedding geometric, structural, and physical priors directly into model architectures. Approaches such as equivariant networks with respect to symmetry groups [63], geometric deep learning frameworks [64], and energy-preserving neural dynamics [65] demonstrate that explicitly respecting underlying structures can significantly enhance data efficiency and robustness of the model. Within generative modeling, these ideas have motivated extensions of diffusion processes to manifolds and function spaces, enabling sampling over constrained geometries and infinite-dimensional objects such as PDE solution spaces [66, 67, 68, 69]. In parallel, structure-preserving constraints, most notably divergence-free conditions for incompressible flows, have been enforced through architectural mechanisms such as divergence-free neural fields and PDE-constrained convolutional operators [70, 71]. Despite the diversity of these techniques, existing methods remain fragmented: manifold-based diffusion typically relies on soft or approximate constraints and involves substantial computational overhead due to discretization [66, 72], while architectural approaches enforce physical structure but are seldom integrated into current diffusion frameworks. To our knowledge, no diffusion-based model unifies autoregressive temporal modeling, principled diffusion design (*e.g.* EDM-style noise and sampling schedules [40]), and hard architectural enforcement of divergence-free constraints as contemplated in this work. Autoregressive diffusion models capture temporal dependencies without strict physical guarantees [49], whereas physics-informed diffusion approaches incorporate constraints only approximately through penalty terms [60, 61], highlighting a clear gap between geometric rigor, physical fidelity, and scalable generative modeling.

1.3. Objective and main contributions

Bridging this gap, the present work develops a theoretically grounded, physics-aware generative framework for incompressible fluid dynamics, focusing on the integration of divergence-free constraints within a diffusion model in order to address (1). Rather than pursuing an exhaustive empirical comparison across machine learning network architectures, we build upon a strong diffusion modeling baseline [40] and compare several design choices for incompressible-flow enforcement. The evaluation prioritizes the statistical accuracy of reconstructed flows under decaying turbulence, as well as the coherence of flow structures. While many generative models and operator learning approaches achieve strong empirical performance in data driven settings, their application to physics constrained problems typically requires problem specific design choices and fine tuning. To avoid confounding such effects, we adopt the canonical two-dimensional Kolmogorov flow, widely used in the machine learning literature (see *e.g.* [61, 69, 73, 74, 75, 76] and more) as a controlled and flexible benchmark that is expected to generalize to a broad class of turbulence problem while providing a simple framework, enabling to explore new modeling ideas and further development.

The main contribution of this work is the construction of a diffusion-based generative framework for fluid dynamics time series that unifies modern diffusion design with strict divergence-free structure. More specifically, we have (i) leveraged state-of-the-art diffusion principles for stability and sampling efficiency, following the EDM framework [40]; (ii) incorporated autoregressive temporal modeling to enable time-coherent forecasting; and (iii) enforced divergence-free constraints through spectral projection, leveraging the Leray decomposition as a finite-dimensional prior in a relevant functional setting. In particular, the proposed framework is designed for diffusion-based modeling of fluid systems, emphasizing a fast and modular structure that can be readily adapted to a wide range of other problems. We present numerical experiments designed to progressively challenge our approach in terms of accuracy, consistency, and statistical faithfulness.

1.4. Outline of the paper

The paper is structured as follow. In Sect. 2, we provide the building blocks of the model (1) with applications to two-dimensional Kolmogorov flows. The Leray projection is introduced as well as the Fourier-Galerkin approximation of solutions. The construction of the dataset used to train the various diffusion models developed in this work is also depicted. The EDM generative framework is recalled in Sect. 3. Unconditional diffusion models are first outlined. Auto-regressive diffusion models are then introduced as conditional versions of the former. Based on this formulation, several divergence-free approaches are proposed in Sect. 4, encompassing both hard and soft constrained methods. They draw inspiration from a range of established methods in physically constrained and physics-informed machine learning [13, 40, 66, 71, 77, 78]. We compute and analyze in Sect. 5 the performance of the hard and soft constrained methods with various numerical experiments. We discuss the advantages and limitations of their implementation in generative modeling, and further emphasize the value of physically informed generative approaches for accurate statistical turbulence reconstruction. Some conclusions and perspectives are finally drawn in Sect. 6.

Besides, several intermediate developments are diverted to appendices. Details of the numerical implementation of the Fourier-Galerkin method are gathered in Appendix A. Details on the implementation of the EDM framework and its training objective are gathered in Appendix B. The correctors of diffusion models implemented to mitigate stiff artifacts in long-horizon rollouts and regulate the energy level in auto-regressive predictions are outlined in Appendix C. The machine learning configuration and corresponding training and sampling hyperparameters are summarized in Appendix D, while the model design and architecture are described in Appendix E. The construction of divergence-free diffusion processes is elaborated in Appendix F. Plots of additional numerical experiments are gathered in Appendix G, Appendix H, and Appendix I.

2. Incompressible Navier-Stokes equations and dataset generation

We first introduce in Sect. 2.1 the incompressible Navier-Stokes equations written as non-linear ordinary differential equations in an *ad hoc* functional setting. This is classically done in terms of the Leray projector on the set of divergence-free, finite energy functions, the linear Stokes operator, and the bilinear convection operator [1, 2]. Then in Sect. 2.2 we consider periodic boundary conditions on the torus and a Fourier-Galerkin spectral method [4] to compute solutions \mathbf{u}^* of Eq. (1) for an arbitrary set of parameters ξ^* in this setting. This allows us to construct in Sect. 2.3 the dataset used to train and test the various generative diffusion models developed in this work.

2.1. Incompressible Navier-Stokes equations

In the deterministic setting, the incompressible Navier-Stokes equations serve as the fundamental model for viscous fluid flows. They are well-posed in two dimensions under standard regularity conditions for which global existence and uniqueness of weak solutions are established. However in three dimensions only global existence of the latter has been proved so far; see [3] and references therein. Let d be the spatial dimension, we study an incompressible flow in a d -dimensional bounded medium $\mathcal{O} \subset \mathbb{R}^d$:

$$\begin{cases} \partial_t \mathbf{u} + (\mathbf{u} \cdot \nabla) \mathbf{u} = -\frac{1}{\varrho} \nabla p + \nu \Delta \mathbf{u} + \mathbf{f}, \\ \nabla \cdot \mathbf{u} = 0, \end{cases} \quad (2)$$

where $\mathbf{u}(\mathbf{r}, t)$ stands for the velocity field, $p(\mathbf{r}, t)$ stands for the pressure field, $\mathbf{r}, t \in \mathcal{O} \times [0, \mathcal{T}]$ for some final time $\mathcal{T} > 0$, ϱ is the fluid density, and ν is its kinematic viscosity. Also ∇ is the gradient vector, $\Delta = \nabla \cdot \nabla$ is the Laplacian operator, and $\mathbf{a} \cdot \mathbf{b}$ is the usual dot product of two vectors \mathbf{a} and \mathbf{b} . The motion of the fluid is triggered by the initial condition $\mathbf{u}(\mathbf{r}, 0) = \mathbf{u}_0(\mathbf{r})$ and the density $\mathbf{f}(\mathbf{r}, t)$ of the external and/or friction forces acting on $\mathcal{O} \times [0, \mathcal{T}]$. In our case, friction forces of the form $\mathbf{f} = -\alpha \mathbf{u}$ can be seen as a crude representation of three-dimensional effects on two-dimensional flows, for example air friction on a thin layer of soap, or layer-layer friction in stratified fluids; see *e.g.* [79, 80]. In geophysical fluid dynamics, they are referred to as Ekman damping, or Ekman drag [81], which will be the model considered here. Next we introduce the Leray projector \mathcal{P} formally defined by [1, 2]:

$$\mathcal{P}\mathbf{v} = \mathbf{v} - \nabla \Delta^{-1}(\nabla \cdot \mathbf{v}), \quad (3)$$

where $\mathbf{v} \in L^2(\mathcal{O}, \mathbb{R}^d)$, say, the set of \mathbb{R}^d -valued square-integrable functions on \mathcal{O} . It has the properties $\mathcal{P} \circ \mathcal{P} = \mathcal{P}^2 = \mathcal{P}$ (hence it is indeed a projector); $\nabla \cdot \mathcal{P}\mathbf{v} = 0$; $\mathcal{P}\mathbf{v} = \mathbf{v}$ whenever $\nabla \cdot \mathbf{v} = 0$; and $\mathcal{P}\nabla\phi = 0$ for any scalar potential ϕ , in particular $\mathcal{P}\nabla p = 0$. Thus, it is the orthogonal projection of functions in $L^2(\mathcal{O}, \mathbb{R}^d)$ onto the subset \mathcal{H} of such functions which are in addition divergence-free (or solenoidal). The functional set \mathcal{H} also embeds boundary conditions on $\partial\mathcal{O}$, such as a vanishing velocity on an aerodynamic profile in external flows, or walls in internal flows. Applying \mathcal{P} to the Navier-Stokes equations (2) yields [1]:

$$\begin{cases} \frac{d\mathbf{u}}{dt} + \nu \mathcal{A}\mathbf{u} + \mathcal{B}(\mathbf{u}) = \mathcal{P}\mathbf{f}, \\ \mathbf{u}(0) = \mathbf{u}_0 \in \mathcal{H}, \end{cases} \quad (4)$$

where we have introduced the linear Stokes operator \mathcal{A} defined by:

$$\mathcal{A}\mathbf{u} = \mathcal{P}(-\Delta \mathbf{u}),$$

and the bilinear convective operator \mathcal{B} defined by:

$$\mathcal{B}(\mathbf{u}, \mathbf{v}) = \mathcal{P}((\mathbf{u} \cdot \nabla) \mathbf{v}), \quad \mathcal{B}(\mathbf{u}) = \mathcal{B}(\mathbf{u}, \mathbf{u}).$$

As a result of the Leray projector and its properties, the pressure gradient is no longer needed in (4), and we have $\mathcal{P}\mathbf{u} = \mathbf{u}$ since \mathbf{u} is divergence-free. We also assume that \mathbf{u}_0 is, by default, divergence-free. Once the velocity field \mathbf{u} is known from Eq. (4), one may recover the pressure p from a Poisson equation but solving it is out of the range of this paper. With reference to Eq. (1), the parameters ξ^* in Eq. (4) are the initial condition \mathbf{u}_0 , the driving load \mathbf{f} , and the kinematic viscosity ν , while the boundary conditions are enforced by the choice of \mathcal{H} . Since our objectives are mainly to focus on the enforcement of the divergence-free physical constraint in generative diffusion models, we choose to solve (4) for periodic boundary conditions. This setting allows us to use a Fourier-Galerkin spectral method, of which numerical analysis is well established [4]. It is also advantageous to study the symmetries and conservation properties of the solutions of Eq. (4) [82]. The Fourier-Galerkin approach is outlined in the next section.

2.2. Fourier-Galerkin approximation

One thus considers periodic boundary conditions in the space variable $\mathbf{r} \in \mathcal{O} = [0, L]^d$, for some spatial period $L > 0$, such that:

$$\mathbf{u}(\mathbf{r} + \mathbf{n}L, t) = \mathbf{u}(\mathbf{r}, t),$$

for all times $t \geq 0$, all $\mathbf{r} \in \mathcal{O}$, and all signed integers $\mathbf{n} = (n_1, \dots, n_d) \in \mathbb{Z}^d$. Then Eq. (4) is reduced to a finite-dimensional system through a Galerkin projection most conveniently carried out in the Fourier basis [4], which leverages the periodicity and spectral structure of (4). A suitable orthonormal basis of $L^2(\mathcal{O}, \mathbb{R}^d)$ is given by the Fourier exponentials $\mathcal{E}_d := \{f_{\mathbf{k}}(\mathbf{r})\}_{\mathbf{k} \in \mathbb{Z}^d}$ (paired with Fourier coefficients):

$$f_{\mathbf{k}}(\mathbf{r}) = e^{i \frac{2\pi}{L} \mathbf{k} \cdot \mathbf{r}}. \quad (5)$$

Then the real-valued, zero-mean velocity field \mathbf{u} admits the Fourier expansion:

$$\mathbf{u}(\mathbf{r}, t) = \sum_{\mathbf{k} \in \mathbb{Z}_*^d} \mathbf{u}_{\mathbf{k}}(t) f_{\mathbf{k}}(\mathbf{r}),$$

where its Fourier coefficients $\mathbf{u}_{\mathbf{k}} \in \mathbb{C}^d$ shall satisfy $\mathbf{k} \cdot \mathbf{u}_{\mathbf{k}} = 0$ (divergence-free condition) and $\overline{\mathbf{u}_{\mathbf{k}}} = \mathbf{u}_{-\mathbf{k}}$ (real-valuedness of \mathbf{u} , $\overline{\mathbf{u}_{\mathbf{k}}}$ standing for the complex conjugate of $\mathbf{u}_{\mathbf{k}}$); also $\mathbb{Z}_*^d = \mathbb{Z}^d \setminus \{\mathbf{0}\}$ (no mean flow). The finite dimensional approximation limits the number of Fourier modes \mathbf{k} to the following subset:

$$\mathcal{K}_N = \left\{ \mathbf{k} \in \mathbb{Z}_*^d; |\mathbf{k}|_{\infty} = \max_{1 \leq i \leq d} |k_i| \leq N \right\},$$

where N stands for the cut-off wavenumber fixed below the Nyquist limit to prevent aliasing. Given some projector $\pi_N = \sum_{\mathbf{k} \in \mathcal{K}_N} \mathbf{f}_\mathbf{k} \otimes \mathbf{f}_\mathbf{k}$, the corresponding finite-dimensional Fourier approximation of Eq. (4) onto the set $\mathcal{H}_N = \text{span}\{\mathbf{f}_\mathbf{k}; \mathbf{k} \in \mathcal{K}_N\} \subset \mathcal{H}$ reads:

$$\begin{cases} \frac{d\mathbf{u}_N}{dt} + \nu \mathbf{A}_N \mathbf{u}_N + \mathbf{B}_N(\mathbf{u}_N) = \mathbf{f}_N, \\ \mathbf{u}_N(0) = \xi_N \in \mathcal{H}_N, \end{cases} \quad (6)$$

for the finite-dimensional Fourier expansion:

$$\mathbf{u}_N(t) = \pi_N \mathbf{u}(t) = \sum_{\mathbf{k} \in \mathcal{K}_N} \mathbf{u}_\mathbf{k}(t) \mathbf{f}_\mathbf{k}.$$

The projected Stokes operator in Eq. (6) is $\mathbf{A}_N = \pi_N \circ \mathcal{A} \circ \pi_N$, the projected convection operator is $\mathbf{B}_N(\cdot) = \pi_N \circ \mathcal{B}(\pi_N \cdot, \pi_N \cdot)$, the projected initial condition is $\mathbf{u}_N(0) = \pi_N \mathbf{u}_0$, and the projected forcing is $\mathbf{f}_N = \pi_N \mathbf{f}$. One may notice that in the Fourier setting, the Leray projection of some field \mathbf{v} reads:

$$\mathcal{P}\mathbf{v} = \sum_{\mathbf{k} \in \mathbb{Z}_*^d} \mathbf{P}_\mathbf{k} \mathbf{v}_\mathbf{k} \mathbf{f}_\mathbf{k}, \quad \mathbf{P}_\mathbf{k} = \mathbf{I} - \hat{\mathbf{k}} \otimes \hat{\mathbf{k}}, \quad (7)$$

where \mathbf{I} is the identity, $\hat{\mathbf{k}} = \frac{\mathbf{k}}{\|\mathbf{k}\|}$ whenever $\mathbf{k} \neq \mathbf{0}$, and $\mathbf{a} \otimes \mathbf{b}$ is the usual tensor product of two vectors \mathbf{a} and \mathbf{b} such that $(\mathbf{a} \otimes \mathbf{b})\mathbf{c} = (\mathbf{b} \cdot \mathbf{c})\mathbf{a}$ for any vector \mathbf{c} . Applying $\mathbf{P}_\mathbf{k}$ to $\mathbf{v}_\mathbf{k}$ amounts to remove the component of $\mathbf{v}_\mathbf{k}$ parallel to \mathbf{k} so that $\mathbf{k} \cdot (\mathbf{P}_\mathbf{k} \mathbf{v}_\mathbf{k}) = 0$. This formulation enables fast, parallelized tensor products (Leray components $\mathbf{P}_\mathbf{k}$ being precomputed) and evades the need to solve a Poisson equation to enforce incompressibility. As a side remark, only half of the spectral modes \mathcal{K}_N are explicitly evolved (according to the lexicographic ordering, *i.e.* $\#\mathcal{K}_N = \frac{1}{2}((2N+1)^d - 1)$), while the remaining half are recovered from the Hermitian symmetry $\bar{\mathbf{u}}_\mathbf{k} = \mathbf{u}_{-\mathbf{k}}$, a property that holds both physically and numerically in machine-learning implementations. The method and the overall simulation procedure are described in Appendix A, along with the choices of external parameters. In particular, an explicit Euler scheme is considered to discretize Eq. (6) in time; see Eq. (A.1).

2.3. Random dataset generation with decaying turbulence

A key issue in this study is to investigate how different strategies for enforcing incompressibility influence the performance of generative diffusion models. To this end, we construct a randomized training set designed to generate two-dimensional ($d = 2$) velocity fields with constant energy across samples. With proper generation, this ensures that the training data are both physically consistent and statistically diverse. The rationale behind this approach is to evaluate the robustness of diffusion models considered in different conditions. In particular, starting from a non-specialized, randomized, and physically viable training set, we assess generalization at three levels:

- In-distribution generalization: predictions on new randomized samples drawn from the same distribution as the training set;
- Temporal generalization (rollouts): predictions over longer time horizons, under relaxed evaluation criteria;
- Out-of-distribution (OOD) generalization: predictions on samples deliberately constructed to deviate from the training set.

As a side note, OOD samples are obtained by introducing symmetries and structural constraints that are absent from the randomized training samples, as later elaborated in Sect. 5.3. The construction of the training set begins with the sampling of a random vorticity ω (a scalar function in two dimensions) according to:

$$\begin{cases} \omega(\mathbf{r}) \sim \mathcal{N}(0, 1), & \mathbf{r} = (x, y), \\ \widehat{\omega}(\mathbf{k}) \sim \mathcal{CN}(0, 1), & \mathbf{k} = (k_x, k_y), \end{cases} \quad (8)$$

where ω is a Gaussian white noise in physical space and $\widehat{\omega}$ is its Fourier transform, corresponding to a complex Gaussian white noise in Fourier space. Throughout the paper $\mathcal{N}(0, \sigma^2)$ stands for the Gaussian distribution on \mathbb{R} with zero mean and standard deviation σ , and $\mathcal{CN}(0, \sigma^2)$ is its complex counterpart. To enforce physical consistency with two-dimensional turbulence, we refer to the numerical evidences of [79], where the turbulent kinetic energy (TKE) spectrum $E(\|\mathbf{k}\|)$ within the inertial range $k_f < \|\mathbf{k}\| < k_\nu$ of direct enstrophy cascade follows:

$$E(\|\mathbf{k}\|) \propto \|\mathbf{k}\|^{-(3+\delta)},$$

with a finite correction $\delta \approx 0.35$ observed even in the simulations with the highest resolution. Here $\ell_f = \frac{\pi}{k_f}$ is the characteristic forcing scale and $\ell_\nu = \frac{\pi}{k_\nu}$ is the characteristic dissipation scale. To achieve this, we propose applying a smooth radial filter $\widehat{\omega}_F(\mathbf{k}) = F(\mathbf{k})\widehat{\omega}(\mathbf{k})$ with:

$$F(\mathbf{k}) = \left(\frac{\|\mathbf{k}\|}{k_f} \right)^{-\frac{\beta}{2}} \left(1 - e^{-\left(\frac{\|\mathbf{k}\|}{k_f} \right)^4} \right) e^{-\left(\frac{\|\mathbf{k}\|}{k_\nu} \right)^8},$$

where the power law $\|\mathbf{k}\|^{-\frac{\beta}{2}}$ enforces the spectral scaling $|F(\mathbf{k})|^2 \sim \|\mathbf{k}\|^{-\beta}$, while the other terms ensure a clean cutoff outside the range $[k_f, k_\nu]$. Since the vorticity spectrum is related to the velocity spectrum by the Biot-Savart law:

$$\widehat{\mathbf{u}}(\mathbf{k}) = \frac{i\mathbf{k}^\perp}{\|\mathbf{k}\|^2} \widehat{\omega}(\mathbf{k}), \quad \mathbf{k}^\perp = (-k_y, k_x), \quad (9)$$

we have that $|\widehat{\omega}(\mathbf{k})|^2 \sim \|\mathbf{k}\|^2 \|\widehat{\mathbf{u}}(\mathbf{k})\|^2$ and a choice of $\beta = 1.35$ yields a TKE spectrum $E(\|\mathbf{k}\|) \sim \|\mathbf{k}\|^{-\beta-2} = \|\mathbf{k}\|^{-3.35}$, consistent with the reported slope in two-dimensional turbulence [79]. While the modes outside the range $[k_f, k_\nu]$ are dissipated, the mean

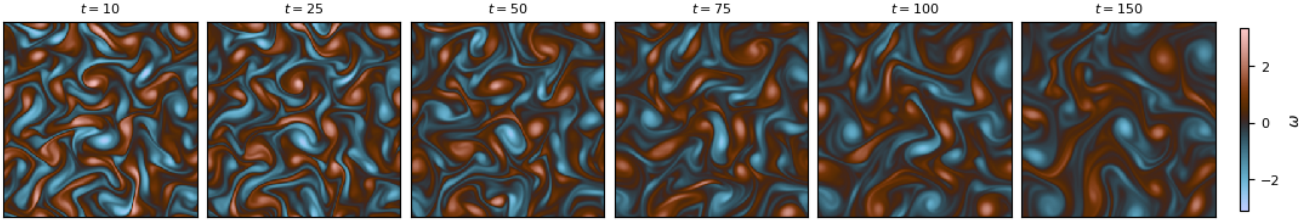


Figure 1: Snapshots of the vorticity field (rollout up to $j_{\max} = 150$).

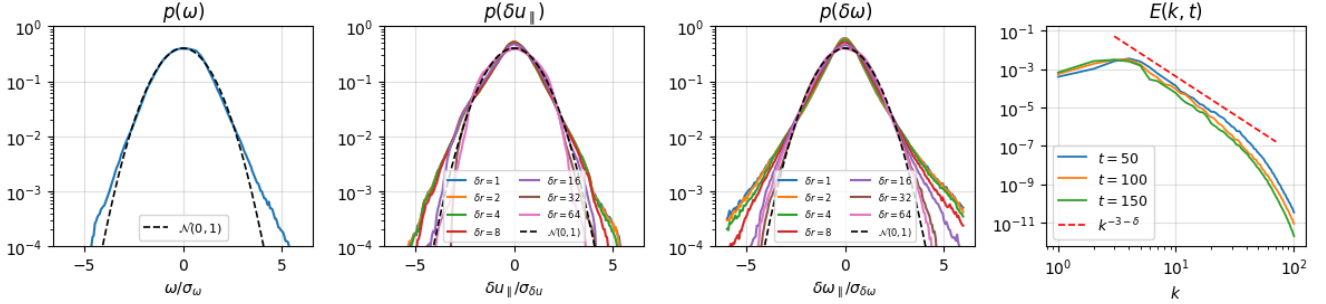


Figure 2: First panel from left to right: empirical density $p_\omega(z; \delta r)$. Second panel: empirical density $p_{\delta u_\parallel}(z; \delta r)$. Third panel: empirical density $p_{\delta \omega_\parallel}(z; \delta r)$. Fourth panel: TKE spectra $k \mapsto E(k)$ from a sampled numerical simulation. The plotted metrics are described in Sect. 5.2.

vorticity is removed by enforcing $\widehat{\omega}_F(\mathbf{0}) = 0$. With the Biot-Savart law, the real-space velocity field \mathbf{u} is retrieved and then rescaled to match a desired amplitude A :

$$\mathbf{u}_{\text{rescaled}} = \frac{A}{u_E} \times \mathbf{u},$$

where $u_E^2 = \langle \|\mathbf{u}\|^2 \rangle = 2E$ is the squared averaged velocity field for $\langle \cdot \rangle$ being the spatial average, and $E = \int_0^{+\infty} E(k) dk$. Besides, we limit ourselves to the externally unforced case considering only a linear friction term $\mathbf{f} = -\alpha \mathbf{u}$ with friction coefficient α . This friction force contributes to damp energy at large scales and makes the inverse energy cascade statistically stationary at late times. In Fourier space, its expansion coefficients are $\mathbf{f}_k(t) = -\alpha_k \mathbf{u}_k(t)$ where:

$$\alpha_k = \begin{cases} \alpha & \text{if } \|k\| \leq k_d, \\ 0 & \text{otherwise,} \end{cases} \quad (10)$$

with $k_d = 2$ targeting large-scale vortices. This damping prevents fast low-frequency energy condensation, below k_d (see Appendix A.2). After a short transient, the field relaxes towards an isotropic regime characterized by smooth yet dynamically active vorticity fields. A toy example of this deterministic, decaying turbulence is given in Figure 1 together with the structure function distributions in Figure 2.

The dataset \mathcal{D} is then constituted as follows. We consider N_{IC} samples of the initial condition (8) and then derive the corresponding initial velocity fields from the Biot-Savart law (9) with the filtered vorticity $\widehat{\omega}_F^i(\mathbf{k})$, $1 \leq i \leq N_{\text{IC}}$. Then for each initial condition we run the forward Euler scheme of Eq. (A.1) up to N_{T} time steps. Among them only N_{T} regularly spaced time instances are kept in \mathcal{D} , which is therefore constituted by $N_{\text{IC}} \times N_{\text{T}}$ frames (snapshots) in \mathbb{R}^n for each component of the velocity field $\mathbf{u} = (u, v)$ in two dimensions, where $n = 2 \times H \times W$ for H and W being the height and width, respectively, of those snapshots. Thus $\mathcal{D} = \{\mathbf{u}_i^{(j)}, 1 \leq i \leq N_{\text{IC}}, 1 \leq j \leq N_{\text{T}}\}$ with $\mathbf{u}_i^{(j)} = \{\mathbf{u}_i^{(j)}(\mathbf{r}_p)\}_{1 \leq p \leq H \times W}$ and:

$$\mathbf{u}_i^{(j)}(\mathbf{r}_p) = \sum_{\mathbf{k} \in \mathcal{K}_N} \mathbf{u}_{i\mathbf{k}}^{(j)} f_{\mathbf{k}}(\mathbf{r}_p),$$

where \mathbf{r}_p is the location of the p -th pixel in \mathcal{O} , and $\{\mathbf{u}_{i\mathbf{k}}^{(j)}, 1 \leq j \leq N_{\text{T}}\}$ is a sub-sampling of the sequence $\{\mathbf{u}_{i\mathbf{k}}^{(j')}, 1 \leq j' \leq N_{\text{T}}\}$ of Fourier coefficients in \mathbb{C}^2 solving Eq. (A.1) with the i -th initial condition (9):

$$\mathbf{u}_{i\mathbf{k}}^{(0)} = \frac{i\mathbf{k}^\perp}{\|\mathbf{k}\|^2} \widehat{\omega}_F^i(\mathbf{k}).$$

Actually sub-sampling is set up past the short transient $j_{\min} > 0$ (which afterwards, is shifted to 0 by numerical convention) after which the two-dimensional vortical structures of the flow start to fully develop towards an isotropic regime, as mentioned above. This delay is considered as the initial time step for both the physical PDE (6) and its generative counterpart outlined in the next section.

3. Diffusion models

In this section the vanilla generative diffusion models used to infer solutions of Eq. (6) from the dataset constructed in Sect. 2.3 are outlined. The objective is to obtain such solutions for initial conditions \mathbf{u}_0^* (the parameters ξ^*) that have not been seen in

the training phase. We start by considering unconditional diffusion in Sect. 3.1 before we turn to conditional diffusion aimed at guiding the generative processes toward physically sound solutions in Sect. 3.2. We note that since those generative processes are transient, here and in the subsequent sections the time variable \vec{t} now refers to the diffusion schedule. The associated forward and backward diffusion processes are denoted by $(\vec{U}_t, t \geq 0)$ and $(\vec{U}_t, t \geq 0)$, respectively. They shall not be confused with the velocity field snapshots $\{(\mathbf{u}^{(j)})^*, 1 \leq j \leq j_{\max}\}$ that we ultimately wish to infer.

3.1. EDM generative framework

Generative models aim to sample $\mathbf{u}^* \in \mathbb{R}^n$ from an unknown data distribution μ_{data} supported on \mathbb{R}^n given a dataset $\mathcal{D} = \{\mathbf{u}_s\}_{s=1}^S$ of S known samples which are assumed to be distributed according to this very distribution, $\mathbf{u}_s \sim \mu_{\text{data}}$. Diffusion models [22, 23, 36, 33] achieve this by corrupting (noising) a clean data sample $\mathbf{u}_0 \sim \mu_{\text{data}}$ in \mathcal{D} through a forward Markov process $(\vec{U}_t, t \geq 0)$ with known transition probabilities $p_{t|0}(\vec{U}_t | \vec{U}_0 = \mathbf{u}_0)$ at the time steps t , and then evaluating a \mathbb{R}^n -valued function $\mathbf{u}, t \mapsto \mathbf{s}(\mathbf{u}, t) := \nabla_{\mathbf{u}} \log p_t(\vec{U}_t = \mathbf{u})$, the so-called Stein's score function, to reverse this process backward in time. However the marginal:

$$p_t(\mathbf{u}) = \int_{\mathbb{R}^n} p_{t|0}(\mathbf{u} | \mathbf{u}_0) \mu_{\text{data}}(\mathbf{d}\mathbf{u}_0)$$

is actually unknown since μ_{data} is unknown, and a parametric neural model $\mathbf{u}, t \mapsto \mathbf{s}_{\theta}(\mathbf{u}, t)$ is trained instead to predict the score function of the corrupted samples \vec{U}_t . Minimizing the resulting denoising score-matching objective yields a reverse-diffusion dynamics capable of generating new samples from μ_{data} , as shown in [22, 23, 33, 36]. The corresponding training objective reads [83]:

$$\theta^* \in \arg \min_{\theta} \int_0^T \lambda(t) \mathbb{E}_{\mathbf{u}_0 \sim \mu_{\text{data}}} \mathbb{E}_{\mathbf{u} \sim p_{t|0}(\mathbf{u} | \mathbf{u}_0)} \left\| \mathbf{s}_{\theta}(\mathbf{u}, t) - \nabla_{\mathbf{u}} \log p_{t|0}(\mathbf{u} | \mathbf{u}_0) \right\|_2^2 dt,$$

to find optimal neural parameters θ^* such that $\mathbf{u}, t \mapsto \mathbf{s}_{\theta^*}(\mathbf{u}, t)$ matches $\mathbf{u}, t \mapsto \mathbf{s}(\mathbf{u}, t)$. Here $t \mapsto \lambda(t)$ is some weighting function, T is the time horizon of the forward noising process, $\|\mathbf{a}\|_2 = (\sum_{k=1}^n a_k^2)^{1/2}$ is the ℓ^2 norm of $\mathbf{a} \in \mathbb{R}^n$, and \mathbb{E} is the ensemble average, or mathematical expectation. Diffusion models with discrete-time Markov chains were first considered in [22, 23, 36] and extended to continuous-time Markov processes solving stochastic differential equations (SDEs) in [33]. Karras et al. [40] have further expanded this SDE generative framework by introducing a general class of Ornstein–Uhlenbeck (OU) processes to improve the vanilla method of [22, 23, 36]. In their so-called EDM formulation the forward process $(\vec{U}, t \geq 0)$ solves:

$$d\vec{U}_t = \frac{\dot{s}(t)}{s(t)} \vec{U}_t dt + s(t) \sqrt{2\sigma(t)\dot{\sigma}(t)} d\vec{W}_t, \quad \vec{U}_0 \sim \mu_{\text{data}}, \quad (11)$$

with time-varying noise and scale functions $t \mapsto \sigma(t)$ and $t \mapsto s(t)$, respectively, such that $s(t) > 0$, with $s(0) = 1$ and $\sigma(0) = 0$. Also $(W_t, t \geq 0)$ is a n -dimensional Wiener process, and $\dot{s} = \frac{ds}{dt}$, $\dot{\sigma} = \frac{d\sigma}{dt}$. The solution of Eq. (11) thus reads:

$$\vec{U}_t = s(t) \left(\vec{U}_0 + \int_0^t \sqrt{2\sigma(\tau)\dot{\sigma}(\tau)} d\vec{W}_{\tau} \right), \quad (12)$$

such that the conditioned random vector $\vec{U}_t | \vec{U}_0$ is Gaussian with conditional expectation and variance given by:

$$\mathbb{E}[\vec{U}_t | \vec{U}_0] = s(t) \vec{U}_0, \quad \mathbb{V}[\vec{U}_t | \vec{U}_0] = (s(t)\sigma(t))^2 \mathbf{I},$$

respectively. Starting from $\vec{U}_0 = \vec{U}_T$, the backward process $\vec{U}_t = \vec{U}_{T-t}$ is then [37, 38]:

$$d\vec{U}_t = \left(-\frac{\dot{s}(t)}{s(t)} \vec{U}_t + 2s(t)^2 \sigma(t)\dot{\sigma}(t) \mathbf{s}(\vec{U}_t, T-t) \right) dt + s(t) \sqrt{2\sigma(t)\dot{\sigma}(t)} d\vec{W}_t. \quad (13)$$

Running Eq. (13) up to $t = T$ yields some frame $\vec{U}_T \sim \mu_{\text{data}}$ to which the desired new sample $\mathbf{u}^* \in \mathbb{R}^n$ is identified. An equivalent deterministic form (in the sense that their solutions have the same marginal distributions at each time step t) is the probability-flow ordinary differential equation (PF-ODE) introduced in [33]:

$$\frac{d\vec{U}_t}{dt} = -\frac{\dot{s}(t)}{s(t)} \vec{U}_t + s(t)^2 \sigma(t)\dot{\sigma}(t) \mathbf{s}(\vec{U}_t, T-t). \quad (14)$$

The score function $\mathbf{s}(\mathbf{u}, t) = \nabla_{\mathbf{u}} \log p_t(\mathbf{u})$ in both Eq. (13) and Eq. (14) is known to explode when $t \rightarrow 0$, as observed in practice for image synthesis in *e.g.* [84]. There it is proposed to stop the backward process at some earlier time $T - \varepsilon$ for a small $\varepsilon > 0$ and consider $\vec{U}_{T-\varepsilon} \sim \mu_{\text{data}}$ instead. A soft probabilistic truncation has been proposed in [85] to replace this hard thresholding. Here the score function is rather parameterized in terms of the denoiser $\mathbb{E}[\vec{U}_0 | \vec{U}_t]$ for Eq. (12), which owing to Tweedie's formula yields [86]:

$$\mathbf{s}(\mathbf{u}, t) = -\frac{\mathbf{u} - s(t)\mathbb{E}[\vec{U}_0 | \vec{U}_t = \mathbf{u}]}{(s(t)\sigma(t))^2}, \quad t > 0.$$

The PF-ODE (14) then reads:

$$\frac{d\vec{U}_t}{dt} = -\left(\frac{\dot{s}(t)}{s(t)} + \frac{\dot{\sigma}(t)}{\sigma(t)} \right) \vec{U}_t + s(t) \frac{\dot{\sigma}(t)}{\sigma(t)} \mathbb{E}[\vec{U}_0 | \vec{U}_t]. \quad (15)$$

Following [40], the foregoing PF-ODE can be further simplified if a constant scale function $s(t) = 1$ is considered. Indeed using the relation $dt = d\sigma/\dot{\sigma}$ in Eq. (15), the latter becomes:

$$\frac{d\tilde{U}_\sigma}{d\sigma} = \frac{1}{\sigma} \left(-\tilde{U}_\sigma + \mathbb{E}[\vec{U}_0|\tilde{U}_\sigma] \right), \quad \sigma > 0. \quad (16)$$

Now the denoiser function $\mathbf{u} \mapsto \mathbb{E}[\vec{U}_0|\mathbf{u}]$ involved in Eq. (15) or Eq. (16) has yet to be constructed for a selected noise schedule σ . It is approximated by a parametric function $\mathbf{D}_\theta(\mathbf{u}; \sigma)$, typically a U-Net [87, 88] of which parameters θ are optimized by considering the following EDM training loss:

$$\mathcal{L}_{\text{EDM}}(\theta) = \mathbb{E}_{\mathbf{u}_0 \sim \mu_{\text{data}}} \mathbb{E}_{\sigma \sim p(\sigma)} \mathbb{E}_{\mathbf{z} \sim \mathcal{N}(\mathbf{0}, \mathbf{I})} [\lambda(\sigma) \|\mathbf{D}_\theta(\mathbf{u}_0 + \sigma\mathbf{z}; \sigma) - \mathbf{u}_0\|_2^2]. \quad (17)$$

Here $p(\sigma)$ stands for the probability distribution considered for sampling the noise schedule σ , $\sigma \mapsto \lambda(\sigma)$ is an associated weighting function. Once the parametric denoiser \mathbf{D}_θ has been trained with optimal parameters θ^* , new samples from μ_{data} are generated by discretizing the PF-ODE (15) with a classical Euler scheme and an additional Heun's second-order correction [89]. Indeed this scheme was shown to offer a good tradeoff between truncation error and the required number of evaluations of the trained denoiser \mathbf{D}_{θ^*} in *e.g.* [90]. Starting from a latent random variable $\tilde{U}_0 \sim \mathcal{N}(\mathbf{0}, (s(T)\sigma(T))^2 \mathbf{I})$, each inference step consists in jointly applying the following backward predictor-corrector iterates over a discrete time schedule $\{t_i\}_{0 \leq i \leq T}$:

$$\begin{cases} \tilde{U}_i \leftarrow \tilde{U}_i + (t_{i+1} - t_i) \tilde{D}_i, \\ \tilde{U}_i \leftarrow \tilde{U}_i + \frac{1}{2} (t_{i+1} - t_i) (\tilde{D}_i + \tilde{D}_{i+1}), \end{cases} \quad (18)$$

where the corrector \tilde{D}_i is:

$$\tilde{D}_i = - \left(\frac{\dot{s}_i}{s_i} + \frac{\dot{\sigma}_i}{\sigma_i} \right) \tilde{U}_i + s_i \frac{\dot{\sigma}_i}{\sigma_i} \mathbf{D}_{\theta^*}(\tilde{U}_i; \sigma_i),$$

and $s_i = s(t_i)$, $\dot{s}_i = \dot{s}(t_i)$, $\sigma_i = \sigma(t_i)$, and $\dot{\sigma}_i = \dot{\sigma}(t_i)$. The second-order correction step in (18) is applied unless $\sigma_{i+1} = 0$. Here in accordance with [40] we choose $s_i = 1$ and $\dot{s}_i = 0$, corresponding to $s(t) = 1$ at all times in the continuous setting. Then we get rid of the discrete time schedule, as well as $\dot{\sigma}$, and according to Eq. (16) the predictor-corrector iterates (18) rewrite:

$$\begin{cases} \tilde{U}_i \leftarrow \tilde{U}_i + (\sigma_{i+1} - \sigma_i) \tilde{D}_i, \\ \tilde{U}_i \leftarrow \tilde{U}_i + \frac{1}{2} (\sigma_{i+1} - \sigma_i) (\tilde{D}_i + \tilde{D}_{i+1}), \end{cases} \quad (19)$$

where again the second-order correction step in (19) is applied unless $\sigma_{i+1} = 0$, and \tilde{D}_i simplifies to:

$$\tilde{D}_i = \frac{1}{\sigma_i} \left(-\tilde{U}_i + \mathbf{D}_{\theta^*}(\tilde{U}_i; \sigma_i) \right). \quad (20)$$

Further details on the implementation of the EDM pipeline are given in Appendix B. The backward iterates of Eq. (19) (or alternatively Eq. (18) if the scale function $t \mapsto s(t)$ is non constant) end up in a sample:

$$\mathbf{u}^* \equiv \tilde{U}_T \sim \mu_{\theta^*}, \quad (21)$$

where μ_{θ} is a parametric approximation of μ_{data} with parameters θ from the EDM pipeline. The extent to which μ_{θ} deviates from μ_{data} in an *ad hoc* measure distance (as well as their supports possibly) is out of the scope of this paper, however this question has been addressed recently in *e.g.* [91] for neural network-based score estimators; see also references therein.

3.2. Auto-regressive conditional generation

The foregoing EDM framework can be extended to the conditional generation of a new sample $\mathbf{u}^* \in \mathbb{R}^n$ from a conditional distribution $\mu_{\text{data}}(\cdot|\mathbf{c})$, where \mathbf{c} stands for the condition imposed to the sampling process *e.g.* observations or labels [43, 92]. This is achieved by considering the \mathbb{R}^n -valued conditional score function $\mathbf{u}, \mathbf{c}, t \mapsto \mathbf{s}(\mathbf{u}, \mathbf{c}, t) := \nabla_{\mathbf{u}} \log p_t(U_t = \mathbf{u}|\mathbf{c})$, with the conditional probability:

$$p_t(\mathbf{u}|\mathbf{c}) = \int_{\mathbb{R}^n} p_{t|0}(\mathbf{u}|\mathbf{u}_0) \mu_{\text{data}}(d\mathbf{u}_0|\mathbf{c}).$$

The backward SDE used to evolve the backward process $(\tilde{U}_t, t \geq 0)$ is the counterpart of Eq. (13) with the above conditional score:

$$d\tilde{U}_t = \left(-\frac{\dot{s}(t)}{s(t)} \tilde{U}_t + 2s(t)^2 \sigma(t) \dot{\sigma}(t) \mathbf{s}(\tilde{U}_t, \mathbf{c}, T-t) \right) dt + s(t) \sqrt{2\sigma(t)\dot{\sigma}(t)} d\tilde{W}_t. \quad (22)$$

Running Eq. (22) up to $t = T$ yields some frame $\tilde{U}_T \sim \mu_{\text{data}}(\cdot|\mathbf{c})$ to which the desired new sample $\mathbf{u}^* \in \mathbb{R}^n$ conditioned on \mathbf{c} is identified. The corresponding conditional denoiser function is $\mathbf{u}, \mathbf{c} \mapsto \mathbb{E}[\vec{U}_0|\mathbf{u}, \mathbf{c}]$ and the conditional PF-ODE is the counterpart of Eq. (15):

$$\frac{d\tilde{U}_t}{dt} = - \left(\frac{\dot{s}(t)}{s(t)} + \frac{\dot{\sigma}(t)}{\sigma(t)} \right) \tilde{U}_t + s(t) \frac{\dot{\sigma}(t)}{\sigma(t)} \mathbb{E}[\vec{U}_0|\tilde{U}_t, \mathbf{c}],$$

or alternatively the counterpart of Eq. (16) if the scale function $s(t)$ is constant:

$$\frac{d\tilde{U}_\sigma}{d\sigma} = \frac{1}{\sigma} \left(-\tilde{U}_\sigma + \mathbb{E}[\vec{U}_0|\tilde{U}_\sigma, \mathbf{c}] \right), \quad \sigma > 0. \quad (23)$$

As for the unconditional case of Sect. 3.1, discrete backward iterates of Eq. (23) of the form (19) end up in a sample:

$$\mathbf{u}^* \equiv \tilde{U}_T \sim \mu_{\boldsymbol{\theta}^*}(\cdot | \mathbf{c}), \quad (24)$$

where $\mu_{\boldsymbol{\theta}}(\cdot | \mathbf{c})$ is now a parametric approximation of $\mu_{\text{data}}(\cdot | \mathbf{c})$ with parameters $\boldsymbol{\theta}$ from the conditional EDM pipeline.

Now in view of our objective to generate rollouts over time of fluid flow velocity fields, a relevant conditioning consists in choosing past predictions to forecast future states. Unlike several learning-based simulators that condition each prediction on long temporal sequences and/or additional auxiliary parameters, as for example [44, 26, 93], we employ a strictly autoregressive formulation in which the next state is generated solely from the knowledge of the immediately preceding one. This design is fundamentally justified by the Markov property of SDEs in finite dimensional Hilbert space of the form (6) when the driving force is a Brownian motion [9, Theorem 3.1]. Owing to this property, conditioning on a single frame is sufficient to encode all information required for physically consistent evolution. Beyond its theoretical grounds, this choice enables efficient next-step generation: the model performs only one forward pass per time step, without maintaining or processing long time histories, and also, enables fast correction mechanisms (see Appendix C). As a result, the autoregressive structure has a low computational cost, allowing the surrogate to run faster than traditional solvers and to support rapid generation although certainly not the best of all [43, 44]. In this sense, the proposed formulation is just a simplification, though a principled and computationally advantageous exploitation of some inherent Markov dynamics. In the remainder of the paper, it is thus implicitly assumed that each future state $\mathbf{u}^{(j+1)}$ of the velocity field at physical time step $j+1$ is generated by conditioning the EDM pipeline with its immediately preceding state $\mathbf{u}^{(j)}$ at physical time step j according to the autoregressive setting:

$$(\mathbf{u}^{(j+1)})^* \sim \mu_{\boldsymbol{\theta}^*}(\cdot | (\mathbf{u}^{(j)})^*). \quad (25)$$

Here we explicitly distinguish the physical time for the evolution of the flow field \mathbf{u} with steps indexed by j , from the diffusion time t of the generative process by the backward SDE (22) (or its PF-ODE counterpart (23) in terms of the noise schedule σ). It is implicit that, to generate a complete flow, one must start from the state $(\mathbf{u}^{(0)})^*$, which is actually provided by the dataset \mathcal{D} itself and serves as the only ground-truth input for generating the entire future trajectory, with the model using its own past predictions as conditioning thereafter.

This setting, in turn, affects the vanilla EDM loss \mathcal{L}_{EDM} of Eq. (17). It is modified to $\mathcal{L}_{\text{EDMc}}$ below so as to train a conditional denoiser $\mathbf{D}_{\boldsymbol{\theta}}(\mathbf{u}, \mathbf{c}; \sigma)$ from paired samples $\mathbf{u}^{(j)}, \mathbf{u}^{(j-1)} \sim \mu_{\text{data}}$ instead of the unconditional training samples $\mathbf{u}^{(j)} \sim \mu_{\text{data}}$ ignoring any time sequencing in the dataset:

$$\mathcal{L}_{\text{EDMc}}(\boldsymbol{\theta}) = \mathbb{E}_{\mathbf{u}^{(j)}, \mathbf{u}^{(j-1)} \sim \mu_{\text{data}}} \mathbb{E}_{\sigma \sim p(\sigma)} \mathbb{E}_{\mathbf{z} \sim \mathcal{N}(\mathbf{0}, \mathbf{I})} [\lambda(\sigma) \|\mathbf{D}_{\boldsymbol{\theta}}(\mathbf{u}^{(j)} + \sigma \mathbf{z}, \mathbf{u}^{(j-1)}; \sigma) - \mathbf{u}^{(j)}\|_2^2]. \quad (26)$$

This leads to several considerations for the design of the denoiser architecture, extending beyond a simple adaptation of the U-Net variants used in baseline diffusion models. Accordingly, our U-Net variant is constructed with the following key principles in mind:

- A conditional architecture enabling controlled conditional generation;
- Circular depthwise-separable convolutions enforcing periodic boundary behavior on each field;
- A low- σ refinement branch that improves high-resolution fidelity in the denoising limit [40];
- Conditional modulation using FiLM (Feature-wise Linear Modulation [94]) parameters derived from the input and the noise schedule σ .

The conditioning is done by concatenation of the current and previous states [25]. Further specifications are given in Appendix E to highlight the adaptation of the U-Net architecture. These issues are however not the main scope of this paper. We rather focus on how to extend the generative framework to account for physical constraints, such as incompressibility of the forecasted flow. The consideration of such a physics-based conditioning is addressed in the next section.

4. Divergence-free constrained diffusion models

Enforcing a divergence-free constraint can be achieved in several ways, ranging from explicit projection operators, *e.g.* the Leray projector \mathcal{P} expressed in Fourier space by Eq. (7), to implicit regularization via divergence-penalizing losses, or by parameterizing the solution space directly through a divergence-free subspace or manifold [1, 2]. Each approach comes with its own trade-offs in terms of numerical stability, approximation quality, and compatibility with machine learning architectures. In Sect. 4.1 the divergence-free condition is enforced by projecting the forward-backward PF-ODE system, while in Sect. 4.2 various settings leveraging the network architecture, its training, or the inference process are proposed.

4.1. Divergence-free manifold

Many machine learning techniques have been proposed to enforce incompressibility, including denoiser-based corrections, adversarial regularization, or divergence-aware architectures (such as convolutional layers adapted to preserve solenoidal structure); see *e.g.* [70, 71, 95, 96, 97, 98]. However, a principled strategy is to constrain the dynamics to evolve strictly within the divergence-free manifold, thereby ensuring physical consistency by construction. Based on Appendix F, we formalize the notion of a divergence-free manifold [66, 99], which provides a formal functional setting for incompressible velocity fields and diffusion modeling. Within this framework, OU noising processes of the form (11) are naturally well-defined. Since the EDM construction is essentially a finite-dimensional OU process equipped with an optimal noise schedule and preconditioning, it can be interpreted as a refined instance of this general setting. For the EDM setup (11)-(14) with the dataset \mathcal{D} of frames in \mathbb{R}^n which are in addition instances

of divergence-free fields projected in a finite-dimensional subset of \mathcal{H} , the drift term vanishes as long as $s(t) = 1$ is chosen, and the diffusion coefficient is linear. This reduces the forward SDE–backward PF-ODE system to a simplified projected form as follows:

$$\begin{cases} d\vec{U}_t = \sqrt{2\sigma(t)\dot{\sigma}(t)}\mathcal{P}d\vec{W}_t, \\ d\vec{U}_t = \frac{\dot{\sigma}(t)}{\sigma(t)}\mathcal{P}\left(-\vec{U}_t + \mathbb{E}[\vec{U}_0|\vec{U}_t]\right)dt, \end{cases} \quad (\mathcal{M})$$

with $\vec{U}_0 \sim \mu_{\text{data}}$ in \mathbb{R}^n . This corresponds to the following forward sampling:

$$\vec{U}_\sigma = \vec{U}_0 + \sigma\mathcal{P}\vec{Z}, \quad \vec{Z} \sim \mathcal{N}(\mathbf{0}, \mathbf{I}_n),$$

where \mathbf{I}_n is the $n \times n$ identity matrix, and a backward inference starting from $\vec{U}_0 = \mathcal{P}\vec{Z}$ with $\vec{Z} \sim \mathcal{N}(\mathbf{0}, \sigma_{\max}^2 \mathbf{I}_n)$ and using the trained denoiser projected on the divergence-free manifold:

$$\mathcal{P}\left(\vec{U}_0 - \mathbb{E}[\vec{U}_0|\vec{U}_\sigma = \mathbf{u}]\right) \simeq \vec{U}_0 - \mathcal{P}\mathbf{D}_{\theta^*}(\mathbf{u}; \sigma),$$

which translate to that very Leray projection dynamics during the whole inference process. The extension of this approach to the conditional setting of Eq. (25) using a conditional denoiser $\mathbf{D}_{\theta^*}(\mathbf{u}, \mathbf{c}; \sigma)$ is straightforward.

4.2. Soft divergence-free enforcement

Other divergence-free methods can be considered and thus compared altogether. Classical machine learning methods contain a number of techniques at their core, designed to address a constraint through optimization. The simplest of them is the training of diffusion models on the divergence-free dataset itself, which serve as the baseline of comparisons (vanilla method). Since diffusion models learn complex data structures, we can evaluate the matching of the divergence-free criteria on prediction made by a properly trained model. Another method that comes to mind is a correction at the model layer [71]. First, the Leray projection can be applied at the output layer of the denoiser model \mathbf{D}_θ of Eq. (B.3):

$$\mathbf{D}_{\theta, \text{div}}(\mathbf{u}; \sigma) = c_{\text{skip}}(\sigma)\mathcal{P}\mathbf{u} + c_{\text{out}}(\sigma)\mathcal{P}\mathbf{F}_\theta(c_{\text{in}}(\sigma)\mathbf{u}, c_{\text{noise}}(\sigma)), \quad (\mathcal{D})$$

such that the divergence-free condition is enforced at the structural design level, and influences the training phase. Again, the extension of this approach (and the proposed subsequent ones) to a conditional denoiser is straightforward.

Second, working with an autoregressive formulation, the Leray projection can be applied at each frame of the autoregressive prediction *i.e.* samples are projected once the inference is made [77], at a physical time step j in the autoregressive pipeline (25). With optimal parameters θ^* from the minimization of the loss (26) the inference at physical time step $j + 1$ reads:

$$(\mathbf{u}^{(j+1)})^* \sim \mu_{\theta^*}(\cdot | \mathcal{P}(\mathbf{u}^{(j)})^*). \quad (\text{SC})$$

This is typically the approach followed in [97] where the generative process is based on stochastic interpolants. It enforces compliance with physical principles by projecting model outputs onto the manifold defined by the underlying laws [99].

Another alternative is to exploit the diffusion modeling sampling architecture by applying a Leray projection as an additional corrector step in the predictor-corrector iterates (19). This correction, which can be seen as the adaptation of [78, 97] within the Leray-projection framework, is aimed towards lower noise levels σ (coarse solver for close-to-clean samples, *e.g.* annealed correction during backward integration):

$$\begin{cases} \vec{U}_i \leftarrow \vec{U}_i + (\sigma_{i+1} - \sigma_i)\vec{D}_i, \\ \vec{U}_i \leftarrow \vec{U}_i + \frac{1}{2}(\sigma_{i+1} - \sigma_i)(\vec{D}_i + \vec{D}_{i+1}), \\ \vec{U}_i \leftarrow (1 - e^{-a\sigma_i})\vec{U}_i + e^{-a\sigma_i}\mathcal{P}\vec{U}_i, \end{cases} \quad (\text{PC})$$

for some parameter $a > 0$ (we fix $a = 10$, which was found to be optimal empirically) and \vec{D}_i given by Eq. (20). Note that the same step of divergence-free correction is applied to the mean-shift corrector iterates (B.2) for a fair comparison.

Finally, one can adopt a PINN-like approach [13] by imposing the divergence-free condition through a residual computation during training:

$$\mathcal{L}(\theta) = \mathcal{L}_{\text{EDM}_c}(\theta) + \lambda_{\text{div}}\mathcal{L}_{\text{div}}(\theta), \quad (\mathcal{L})$$

where:

$$\mathcal{L}_{\text{div}}(\theta) = \mathbb{E}_{\mathbf{u}_0 \sim \mu_{\text{data}}} \mathbb{E}_{\sigma \sim p(\sigma)} \mathbb{E}_{\mathbf{z} \sim \mathcal{N}(\mathbf{0}, \mathbf{I})} [\|(\mathbf{I} - \mathcal{P})\mathbf{D}_\theta(\mathbf{u}_0 + \sigma\mathbf{z}, \mathbf{c}; \sigma)\|_2^2].$$

λ_{div} is a scaling coefficient adaptively calibrated such that the gradient magnitudes of the physical regularization loss \mathcal{L}_{div} and the baseline conditional EDM loss $\mathcal{L}_{\text{EDM}_c}$ are initially comparable:

$$\lambda_{\text{div}} = \frac{\|\nabla_\theta \mathcal{L}_{\text{EDM}_c}(\theta)\|}{\|\nabla_\theta \mathcal{L}_{\text{div}}(\theta)\| + \varepsilon},$$

for some matching parameter $0 < \varepsilon \ll 1$ (typically $\varepsilon = 10^{-7}$ to evade numerical instabilities). This gradient-based normalization ensures that the PINN-like regularization loss contributes meaningfully during the early training phase without dominating the optimization dynamics.

Each of these methods is represented by its own symbol in Table 1: vanilla model (\mathcal{V}) when no divergence-free conditioning is enforced at all (the plain EDM framework of Sect. 3.1), divergence-free diffusion manifold (\mathcal{M}), denoiser architecture correction (\mathcal{D}), sample correction (SC), predictor-corrector iterates (PC), and residual computation (\mathcal{L}). Among them, four require an independent training procedure, namely (\mathcal{V}), (\mathcal{M}), (\mathcal{D}), and (\mathcal{L}). The remaining two evaluations by (SC) and (PC) are derived from the vanilla

Numerical method	Symbol	Description	Strength
vanilla	(\mathcal{V})	Classical diffusion model.	None
div_free_manifold	(\mathcal{M})	Diffusion model on divergence-free manifold.	<i>strict</i>
div_free_denoiser	(\mathcal{D})	Projection at model output level (architectural).	<i>strict</i>
div_free_residual	(\mathcal{L})	Residual computation of divergence.	<i>soft</i>
div_free_autoReg	(\mathcal{SC})	Projection at each frame.	<i>soft</i>
div_free_correction	(\mathcal{PC})	Gradual projection correction.	<i>strict</i>

Table 1: Summary of the proposed divergence-free constraint techniques based on diffusion model structural design.

model (\mathcal{V}) once it has been trained. The strength of divergence-free enforcement is determined by whether it is strictly imposed (up to numerical precision) or statistically dependent (e.g., during a training or heuristic sampling phase). Each training method is allocated the same computational budget (*i.e.* the same total number of optimization steps or epochs) [100], ensuring that all methods are compared under equal resource constraints and can, in principle, converge to their best possible performance under that budget. To maintain fairness, we also use an identical learning-rate scheduler and other hyperparameters (*e.g.* batch size, regularization) across all methods. With this setup, no method is advantaged by allowing more iterations or a more favorable schedule; thus the comparison isolates differences in model architecture, objective, or training algorithm, rather than resources disparity. Further detail on both the training and inference parameters are given in Appendix A.2.

5. Results

In this section, we demonstrate the effectiveness and robustness of the proposed divergence-free diffusion methods across a hierarchy of test scenarios. These tests are designed to progressively challenge the models along two complementary axes: short-term predictive accuracy and long-term physical consistency. The former assesses the ability of the model to reproduce fine-scale flow structures and instantaneous spatial correlations within a limited temporal horizon, while the latter evaluates whether the generated dynamics remain statistically faithful to the reference turbulent regime as time advances or as the test conditions depart from the training distribution. The training and sampling parameters for these numerical tests are gathered in Appendix D.

In-distribution assessment. The first and most straightforward setting is the in-distribution test, where predictions are performed over the same temporal window as the one considered during training, but with unseen initial conditions (8). We typically use three independent realizations of the latter, which we find sufficient for statistical stability. Because this setup closely matches the training regime, we employ stringent pixel-wise metrics such as the relative mean-squared error (MSE), the ℓ^2 norm, and the accuracy of the TKE spectrum $k \mapsto E(k)$.

Rollout predictions. In this setting, the model is evaluated over extended temporal horizons, beyond its training range. While we still report quantitative measures such as the relative ℓ^2 error to gauge possible drift, the focus shifts toward statistical fidelity, whether the generated dynamics preserve relevant physical and turbulence statistics as the rollout progresses.

Out-of-distribution tests. Finally, we consider out-of-distribution (OOD) scenarios, where the model is exposed to initial or physical conditions markedly different from those seen during training. Here, the evaluation is primarily qualitative, supplemented by selected quantitative indicators, to assess the robustness and generalization capacity of the methods.

5.1. In-distribution assessment

Metrics. For the in-distribution assessment, we generate M_{IC} randomly drawn initial conditions (8) and forecast the corresponding velocity field snapshots $(\mathbf{u}^{(j)})^* \in \mathbb{R}^n$ by the different methods proposed in Table 1 up to $M_t = N_t/2$. While the training set actually contains N_t snapshots for each different initial condition, this simple test evaluates the pointwise accuracy in the early phase of the prediction. In addition, for each initial condition the generative process is repeated M_S times, such that $M_{\text{IC}} \times M_S \times M_t$ snapshots in \mathbb{R}^n are indeed generated for each method in Table 1. As a side note, visual (qualitative) assessments will rely on vorticity plot, as it combines the 2-dimensional velocity field in one scalar representation, which simplify the plotting aspect. For $\mathbf{u}(\mathbf{r}, t) = (u(\mathbf{r}, t), v(\mathbf{r}, t))$ being the flow velocity field with $\mathbf{r} = (x, y) \in \mathcal{O} \subset \mathbb{R}^2$, the scalar vorticity field is $\omega(\mathbf{r}, t) = \text{curl} \cdot \mathbf{u}(\mathbf{r}, t) = -\partial_y u(\mathbf{r}, t) + \partial_x v(\mathbf{r}, t)$, where $\text{curl} := (-\partial_y, \partial_x)^\top$. An example is shown on Figure 3, where snapshots $\mathbf{u}^{(j)} \in \mathbb{R}^n$ of the ground-truth solution are displayed together with snapshots $(\mathbf{u}^{(j)})^* \in \mathbb{R}^n$ predicted by the vanilla EDM diffusion model (\mathcal{V}) and the proposed diffusion model on divergence-free manifold (\mathcal{M}) .

Across all methods, the primary objective remains the preservation of the divergence-free condition, while simultaneously ensuring accurate quantitative predictions of the flow fields. The degree of incompressibility is assessed through the spectral divergence error ε_{div} , defined as the normalized scalar product of the inferred velocity field \mathbf{u}^* with its wave vectors in Fourier space:

$$\varepsilon_{\text{div}} = \frac{\sum_{\mathbf{k} \in \mathcal{K}_N} |\mathbf{k} \cdot (\mathbf{u}_{\mathbf{k}}^{(j)})^*|^2}{\sum_{\mathbf{k} \in \mathcal{K}_N} \|\mathbf{k}\|^2 \|(\mathbf{u}_{\mathbf{k}}^{(j)})^*\|^2}, \quad 1 \leq j \leq M_t.$$

A perfectly divergence-free field yields $\varepsilon_{\text{div}} = 0$ (near 10^{-6} with float-32 bits numerical precision), while larger values indicate increasing deviation from the solenoidal subspace. To quantify the accuracy of predictions over the computational domain \mathcal{O} , some classical pixel-wise metrics are used, which are recalled in Appendix G.1. They provide a direct and robust assessment of

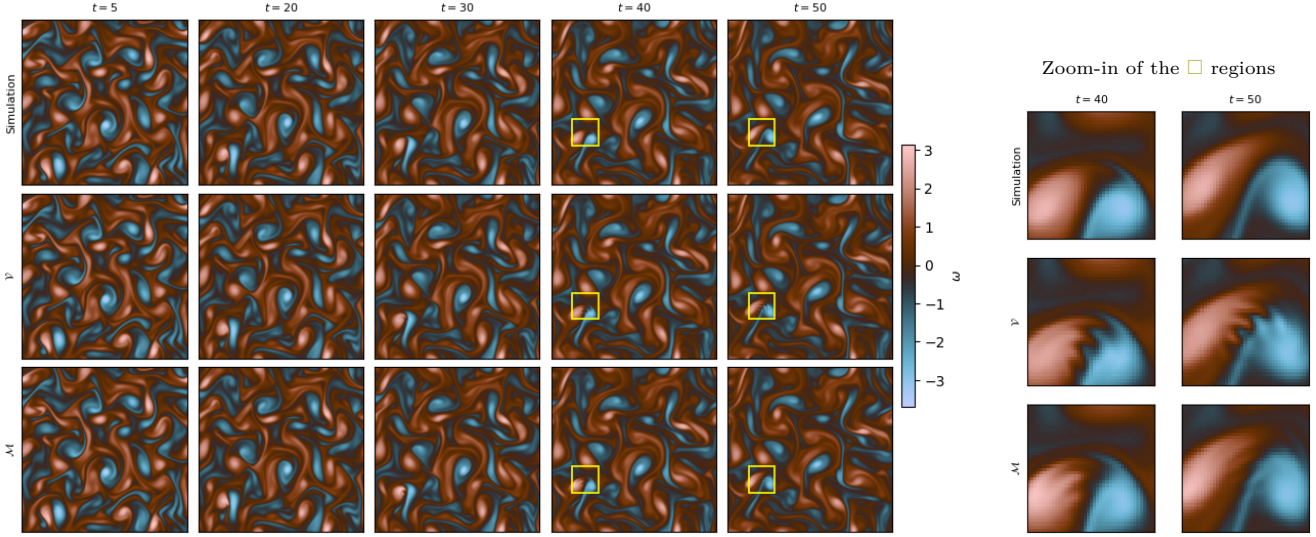


Figure 3: In-distribution assessment. Left panel: snapshots of the ground-truth solution (vorticity, top row) against snapshots inferred by vanilla EDM diffusion model (\mathcal{V}) (middle row) and by diffusion model on divergence-free manifold (\mathcal{M}) (bottom row). Right panel: zoomed-in regions of vorticity.

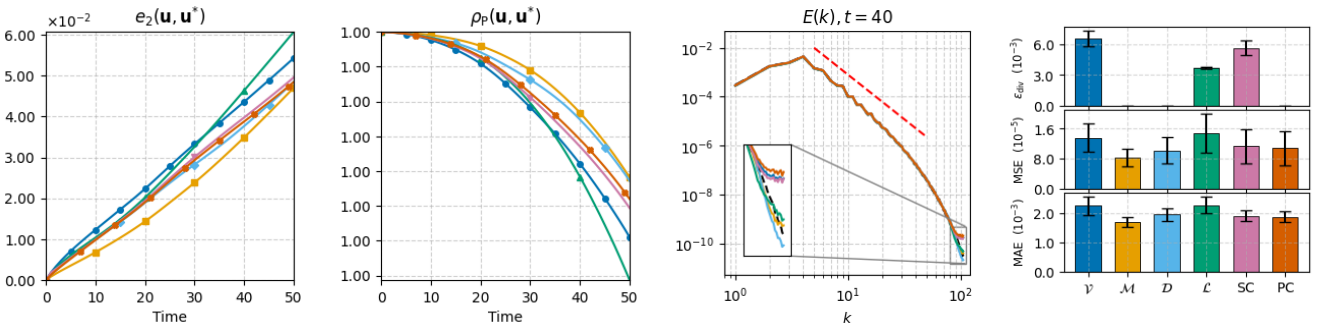


Figure 4: In-distribution assessment. First panel from left to right: relative ℓ^2 error e_2 (lower is better). Second panel: Pearson correlation coefficient ρ_P (higher is better). Third panel: TKE spectra $k \mapsto E(k)$. Fourth panel: ϵ_{div} , MSE and MAE (lower is better). Legends: (\mathcal{V}) \bullet , (\mathcal{M}) \blacksquare , (\mathcal{D}) \blacklozenge , (\mathcal{L}) \blacktriangle , (SC) \blacktriangledown , (PC) \times . TKE slopes legend: --- is ground truth spectrum, --- is $k^{-3-\delta}$ slope.

reconstruction fidelity, which is particularly relevant for short-time, in-distribution evaluations. In addition, two temporal metrics are reported in Figure 4, namely the relative ℓ^2 errors $e_2(\mathbf{u}^{(j)}, (\mathbf{u}^{(j)})^*)$ for different physical time steps j , where:

$$e_2(\mathbf{u}, \mathbf{u}^*) = \frac{\|\mathbf{u} - \mathbf{u}^*\|_2}{\|\mathbf{u}\|_2},$$

and the Pearson correlation coefficients $\rho_P(\mathbf{u}^{(j)}, (\mathbf{u}^{(j)})^*)$, where:

$$\rho_P(\mathbf{u}, \mathbf{u}^*) = \frac{\langle \mathbf{u} - \bar{\mathbf{u}}, \mathbf{u}^* - \bar{\mathbf{u}}^* \rangle}{\|\mathbf{u} - \bar{\mathbf{u}}\|_2 \|\mathbf{u}^* - \bar{\mathbf{u}}^*\|_2},$$

for $\langle \mathbf{a}, \mathbf{b} \rangle$ being the scalar product of vectors $\mathbf{a}, \mathbf{b} \in \mathbb{R}^n$, and $\bar{\mathbf{a}}$ being the component-wise average of $\mathbf{a} \in \mathbb{R}^n$. The relative ℓ^2 error e_2 provides a scale-independent measure of reconstruction quality by normalizing the ℓ^2 norm of the residual with respect to the ℓ^2 norm of the ground truth. Therefore it quantifies the overall proportion of signal energy that is not recovered. Complementarily, the Pearson correlation coefficient ρ_P assesses the linear association between predicted and true values, reflecting how well the model reproduces the underlying trends regardless of absolute scaling. Together, these metrics quantify both magnitude accuracy and relational consistency.

Results. Overall, the methods achieve highly accurate reconstructions across all evaluated settings. As shown in Figure 3, and further detailed in the comprehensive set of experiments in Appendix G.2, the reconstructed fields are almost perfectly aligned with the ground truth and minimal deviations are observed. These additional results corroborate the initial observation that all models recover the coarse-scale structure with minimal error.

However, when inspecting localized regions at higher magnification, some artifacts begin to emerge. In particular, both soft and strict divergence-free constrained approaches of Sect. 4.2 consistently display fine-scale wrinkles or wave-like distortions along regions where the flow exhibits sharp curvature changes. These artifacts, though small in amplitude, indicate a limitation in how well the penalty translates in an autoregressive framework. However, one of the proposed method (\mathcal{M}) effectively suppresses these distortions over time, producing smoother and more physically consistent reconstructions even in the most challenging regions. As a side note, this defect was the only one seen across the M_S runs of the corresponding generative methods, the other ones being not displayed in this study since our goal is to discriminate the methods as sharply as possible.

The pointwise evaluation (*e.g.* e_2 , ε_{div} , MSE and MAE) presented in Figure 4 further reinforces this trend. Across all metrics, (\mathcal{M}) yields the lowest reconstruction errors, demonstrating the clear benefit of enforcing the constraint at the manifold level rather than relying on penalty terms. A general pattern also emerges: the stricter the imposed physical constraint, the better the reconstruction quality, particularly for short time horizons. Indeed, both (\mathcal{M}) and (\mathcal{D}) show consistent spectra near Nyquist regions (*e.g.* magnified zones in Figure 4), (PC) being the exception to the rule.

Nevertheless, the temporal analysis reveals an important nuance. As the evolution time step j increases, (\mathcal{M}) gradually converges toward the behavior of the divergence-free denoiser model (\mathcal{D}) and the soft-constrained methods; see Pearson correlation coefficients ρ_P in Figure 4. In fact, its error growth rate accelerates over longer rollout intervals, suggesting that the advantages observed at early times may diminish as accumulated approximation errors propagate forward. Depending on the task or integration horizon, this effect may ultimately shift the performance ranking. This will be the purpose of the statistical study of rollout evaluation in the next Sect. 5.2. Finally, all methods but (\mathcal{L}) have consistently beaten the vanilla method (\mathcal{V}) , both in terms of accuracy (e_2 error) and divergence-free constraint (ε_{div} report).

5.2. Rollout predictions

Now we study the performances of each method of Table 1 on a longer time horizon, *i.e.* rollout predictions. Since further prediction time steps (in addition to the autoregressive formulation (25)) induce longer error accumulation, we focus on statistical assessment of the fluid velocity structure. We first introduce the longitudinal velocity increment $\delta u_{\parallel}(\mathbf{r}, t; \delta r)$ with spatial increment δr along an arbitrary unit vector \mathbf{e} given by [82, Chapter 6]:

$$\delta u_{\parallel}(\mathbf{r}, t; \delta r) = (\mathbf{u}(\mathbf{r} + \delta r \mathbf{e}, t) - \mathbf{u}(\mathbf{r}, t)) \cdot \mathbf{e}. \quad (27)$$

Likewise, we define the vorticity increment $\delta \omega_{\parallel}(\mathbf{r}, t; \delta r)$ by:

$$\delta \omega_{\parallel}(\mathbf{r}, t; \delta r) = \omega(\mathbf{r} + \delta r \mathbf{e}, t) - \omega(\mathbf{r}, t). \quad (28)$$

Besides, we refer to [82, Chapter 7] to compute the turnover time τ_{ℓ} , or circulation time associated with the scale ℓ , describing the characteristic distortion time: the period over which a structure of size ℓ is substantially deformed by relative motion, *i.e.* its rollout timescale. Taking $\ell \sim L/6$ as an upper-bound estimate, the corresponding large-scale eddy turnover time formally reads (for $\ell \leq L/2 \sim \ell_0$ the integral scale):

$$\tau_{\ell} = \frac{\ell}{u_{\ell}}, \quad u_{\ell} = \sqrt{\mathbb{E}\{(\delta u_{\parallel}(\ell))^2\}},$$

where $\delta u_{\parallel}(\delta r)$ is the longitudinal velocity increment defined above in Eq. (27), where we drop the dependence on t and \mathbf{r} invoking the usual assumptions of statistical time stationarity and spatial homogeneity of a turbulent velocity field \mathbf{u} [9]. Under the loose assumption that:

$$\mathbb{E}\{(\delta u_{\parallel}(\ell))^2\} \approx \mathbb{E}\{\|\mathbf{u}_N(0)\|^2\},$$

where $\mathbf{u}_N(0)$ is as in Eq. (6), we may treat the velocity fluctuations at scale ℓ as being of the same order as the average velocity, thereby allowing larger spatial scales to be effectively taken into account over time. The associated eddy turnover time, which we adopt as the rollout objective, is about $\tau_{\ell} \simeq 7.5$ s. This value is deliberately rounded up (*i.e.*, ceiled) to match $j_{\max} = 150$ (exactly 3/2 of the training dataset final time $N_t = 100$). Choosing a larger time horizon corresponds to a more challenging prediction task and avoids any bias.

5.2.1. Short-horizon rollout accuracy

Metrics. For a given generative method in Table 1 used to infer the velocity field snapshots $(\mathbf{u}^{(j)})^*, j_{\min} \leq j \leq j_{\max}$, the probability density functions (PDF) of the spatial increments (27) and (28) are first computed over all spatial locations \mathbf{r}_p , $1 \leq p \leq H \times W$, of the computational domain \mathcal{O} for each time step j , yielding per-snapshot empirical distributions. These PDFs are then aggregated over the M_{IC} initial conditions, M_{S} runs of the generative method (with different initial noise seeds), and time steps $j_{\min} \leq j \leq j_{\max}$ to form the overall empirical distribution. Aggregation is performed using an empirical mean to obtain a robust estimate that is less sensitive to intermittencies or outlier realizations, preserving the overall trends observed on the plots. For $I = (i-1) \times M_{\text{S}} + s$ with $s = 1, \dots, M_{\text{S}}$, $i = 1, \dots, M_{\text{IC}}$, and $(\mathbf{u}_I^{(j)})^*$ being the corresponding inferred velocity snapshots, the velocity increments (27) read:

$$(\delta u_{\parallel}^I(\mathbf{r}, j; \delta r))^* = ((\mathbf{u}_I^{(j)}(\mathbf{r} + \delta r \mathbf{e}))^* - (\mathbf{u}_I^{(j)}(\mathbf{r}))^*) \cdot \mathbf{e}.$$

Their aggregated empirical PDF then reads:

$$p_{\delta u_{\parallel}}^*(z; \delta r) = \frac{1}{Z} \sum_{j=j_{\min}}^{j_{\max}} \sum_{p=1}^{H \times W} \sum_{s=1}^{M_{\text{S}}} \sum_{i=1}^{M_{\text{IC}}} \delta(z - (\delta u_{\parallel}^I(\mathbf{r}_p, j; \delta r))^*),$$

where $z \mapsto \delta(z)$ stands for the Dirac delta function, and $Z = M_{\text{IC}} \times M_{\text{S}} \times H \times W \times (j_{\max} - j_{\min} + 1)$ is the normalization constant. The empirical PDF $p_{\delta \omega_{\parallel}}^*(z; \delta r)$ of the vorticity increments (28) is defined analogously, as well as the empirical PDF $p_{\omega}^*(z; \delta r)$ of the inferred vorticity snapshots $(\omega^{(j)})^*$ themselves. They are displayed on Figure 6, together with the corresponding empirical PDFs of the ground-truth solutions $\mathbf{u}^{(j)}$ and $\omega^{(j)}$ denoted by $p_{\delta u_{\parallel}}(z; \delta r)$, $p_{\delta \omega_{\parallel}}(z; \delta r)$, and $p_{\omega}(z; \delta r)$, respectively. While PDFs capture the statistical behavior of the fields and thus reflect rollout consistency, they are not visually discriminative. We therefore also report the Kullback–Leibler divergence for quantitative comparison. For each method in Table 1, the discrepancy between the predicted and ground-truth PDFs is quantified via:

$$D_{\text{KL}}(p_{\varphi} \| p_{\varphi}^*; \delta r) = \int p_{\varphi}(z; \delta r) \log \frac{p_{\varphi}(z; \delta r)}{p_{\varphi}^*(z; \delta r)} dz, \quad \varphi \in \{\delta u_{\parallel}, \delta \omega_{\parallel}, \omega\}.$$

The box plot in Figure 6 then displays the divergence $D_{\text{KL}}(p_{\varphi} \| p_{\varphi}^*; \delta r)$ (with median and interquartile range) for each $\varphi \in \{\delta u_{\parallel}, \delta \omega_{\parallel}, \omega\}$ and for all methods in Table 1 with $\delta r = 8$ pixels (with other displacements available in Appendix H). Apart from the density estimation, we also report a range of metrics given in Sect. 5.1 and, as a broader statistical evaluation, the relative amplitude rA , defined in Appendix G.1.

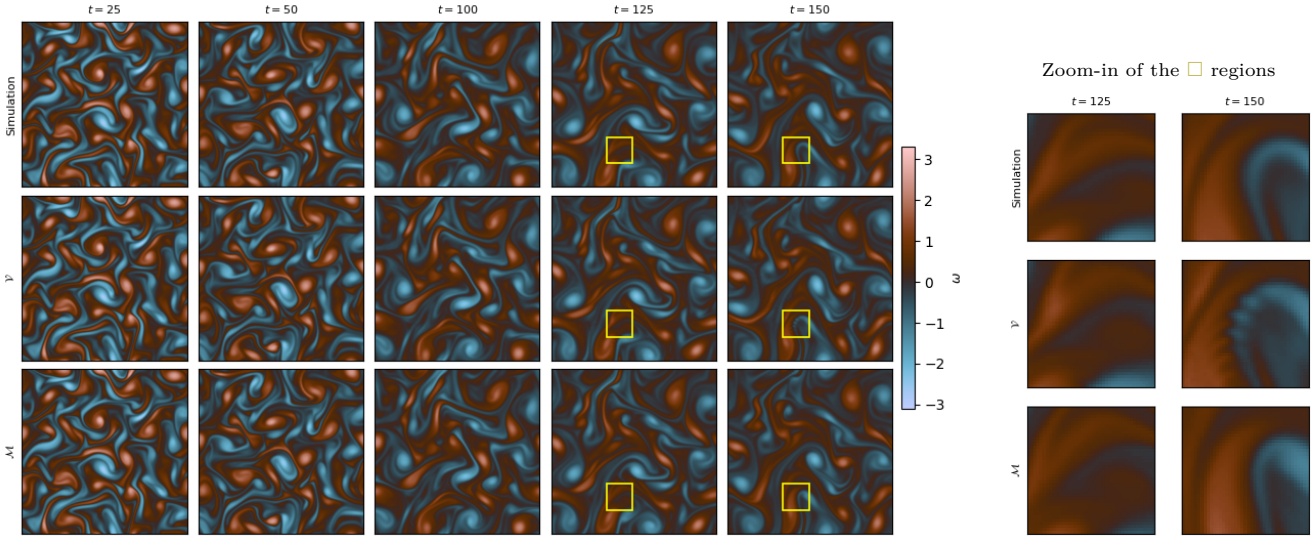


Figure 5: Rollout predictions. Left panel: snapshots of the ground-truth solution (vorticity, top row) against snapshots inferred by vanilla EDM diffusion model (\mathcal{V}) (middle row) and by diffusion model on divergence-free manifold (\mathcal{M}) (bottom row). Right panel: zoomed-in regions of vorticity.

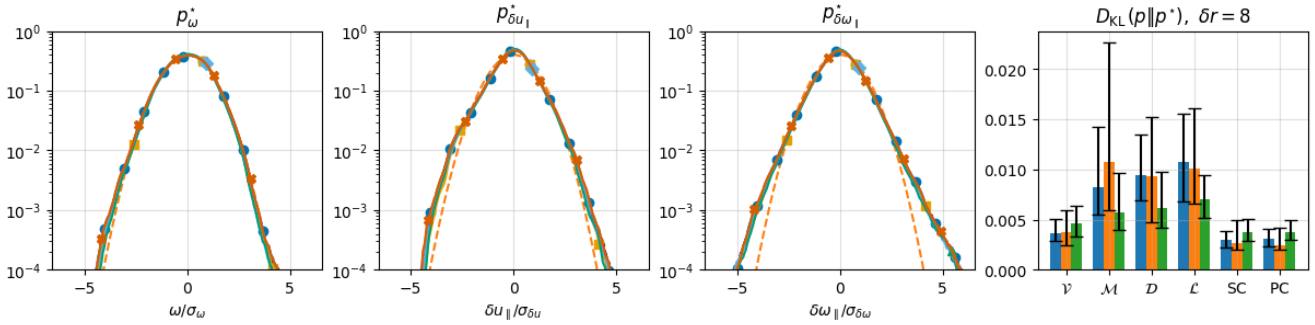


Figure 6: Rollout predictions. First panel from left to right: empirical density $p_\omega^*(z; \delta r)$. Second panel: empirical density $p_{\delta u_\parallel}^*(z; \delta r)$. Third panel: empirical density $p_{\delta \omega_\parallel}^*(z; \delta r)$. Fourth panel: Kullback-Leibler divergence for $\delta r = 8$. Density plots legends: — ground truth, - - - $\mathcal{N}(0, 1)$, (\mathcal{V}) ●, (\mathcal{M}) ■, (\mathcal{D}) ◆, (\mathcal{L}) ▲, (\mathcal{SC}) ▼, (\mathcal{PC}) ✕. Box plot legends: $D_{KL}(p_\omega \parallel p_\omega^*; \delta r)$ ■, $D_{KL}(p_{\delta u_\parallel} \parallel p_{\delta u_\parallel}^*; \delta r)$ ■, $D_{KL}(p_{\delta \omega_\parallel} \parallel p_{\delta \omega_\parallel}^*; \delta r)$ ■. Whiskers indicate the interquartile range.

Results. As shown in Figure 5, we observe the same rippling artifacts that are caused by the same methods (all but (\mathcal{M})). This behavior is expected and, to some extent, satisfactory, as the flow patterns are consistent across time and methods. The same qualitative and quantitative conclusions as in Sect. 5.1 hold in this rollout setting. In particular, these ripples are likely caused by hard or previously unseen configurations. We deliberately choose to display such cases, noting that most samples do not exhibit these anomalies. We address this behavior in the next Sect. 5.2.2, where a correction algorithm is introduced for even longer rollout, where (\mathcal{M}) also suffers from the same fate for large enough time. Again, all methods (apart from this artifact) yield visually consistent samples, as shown in detail in the exhaustive study of Appendix H.

We now turn to the full rollout regime results, where our primary interest lies in statistical properties rather than point-wise errors. Interestingly, the trend reverses (as expected from trends observed in Sect. 5.1): divergence-free methods enforced through the vanilla model (\mathcal{V}) perform better (e.g. (PC) and (SC)). This behavior is consistently observed in the empirical probability density functions shown in Figure 6 across multiple δr scales (see Appendix H). This result may be considered intuitive: as constraints are relaxed, relative to the unconstrained (\mathcal{V}) method, the learned dynamics become statistically more accurate, since a model trained without constraints has more degrees of freedom. In contrast, the more stringent methods (built upon physical constraints) effectively operate at the interface between the training distribution and the out-of-distribution regime encountered toward the end of the rollout, where a softer enforcement of constraints is required to allow for greater flexibility. Overall, this represents a favorable trade-off. Notably, the method of predictor-corrector iterates with gradual Leray projections (PC) achieves both perfect divergence-free behavior, the lowest statistical error (which we further examine in Table 2) and satisfying visual consistency (despite (\mathcal{M}) being the only one free of any artifact).

Finally, we consider more point-wise error metrics. Although not our primary focus, these temporally averaged quantities remain highly informative. The results are summarized in Table 2. As previously noted, methods derived from (\mathcal{V}) achieve excellent performance, exhibiting strong overall results with limited variance across approaches (without undermining the performance of (\mathcal{M}) and (\mathcal{D})). The rA metric further supports the claim made in the previous paragraph: the best amplitude agreement is achieved by (\mathcal{V}), followed by (PC) and (SC). This indicates that (\mathcal{V}) better captures the local mean flow and that its predictions can be corrected at post-training using divergence-free methods. Nevertheless, a clear winner emerges: (PC) consistently outperforms the vanilla baseline and all other approaches in terms of error, while simultaneously enforcing perfect divergence-free constraints. Conversely, (\mathcal{L}) performs poorly across all metrics, consistently under-performing both in in-distribution assessment and in the

rollout evaluation.

Method	MSE	MAE	e_2	ε_{div}	rA
\mathcal{V}	$1.41 \cdot 10^{-4} \pm 1.59 \cdot 10^{-4}$	$7.02 \cdot 10^{-3} \pm 4.69 \cdot 10^{-3}$	$9.09 \cdot 10^{-2} \pm 6.30 \cdot 10^{-2}$	$8.07 \cdot 10^{-3} \pm 2.52 \cdot 10^{-4}$	$1.00 \cdot 10^0 \pm 5.36 \cdot 10^{-3}$
\mathcal{M}	$1.55 \cdot 10^{-4} \pm 1.86 \cdot 10^{-4}$	$7.23 \cdot 10^{-3} \pm 5.44 \cdot 10^{-3}$	$9.20 \cdot 10^{-2} \pm 7.11 \cdot 10^{-2}$	0 ± 0	$9.70 \cdot 10^{-1} \pm 2.01 \cdot 10^{-2}$
\mathcal{D}	$1.83 \cdot 10^{-4} \pm 2.24 \cdot 10^{-4}$	$7.67 \cdot 10^{-3} \pm 5.62 \cdot 10^{-3}$	$1.00 \cdot 10^{-1} \pm 7.70 \cdot 10^{-2}$	0 ± 0	$9.73 \cdot 10^{-1} \pm 1.51 \cdot 10^{-2}$
\mathcal{L}	$2.07 \cdot 10^{-4} \pm 2.58 \cdot 10^{-4}$	$8.25 \cdot 10^{-3} \pm 5.96 \cdot 10^{-3}$	$1.07 \cdot 10^{-1} \pm 8.21 \cdot 10^{-2}$	$5.21 \cdot 10^{-3} \pm 2.63 \cdot 10^{-5}$	$9.68 \cdot 10^{-1} \pm 2.05 \cdot 10^{-2}$
SC	$1.20 \cdot 10^{-4} \pm 1.50 \cdot 10^{-4}$	$6.26 \cdot 10^{-3} \pm 4.44 \cdot 10^{-3}$	$8.20 \cdot 10^{-2} \pm 6.11 \cdot 10^{-2}$	$7.01 \cdot 10^{-3} \pm 2.29 \cdot 10^{-4}$	$1.01 \cdot 10^0 \pm 6.07 \cdot 10^{-3}$
PC	$1.15 \cdot 10^{-4} \pm 1.44 \cdot 10^{-4}$	$6.18 \cdot 10^{-3} \pm 4.38 \cdot 10^{-3}$	$8.04 \cdot 10^{-2} \pm 5.98 \cdot 10^{-2}$	0 ± 0	$1.01 \cdot 10^0 \pm 8.16 \cdot 10^{-3}$

Table 2: Rollout predictions averaged metrics.

5.2.2. Long-horizon structural coherence

Motivated by the observations done in Sect. 5.1 and Sect. 5.2.1, we address the small-scale rippling artifacts observed in the predicted velocity fields. These artifacts appear as spurious high-frequency oscillations on top of on otherwise accurate large-scale flow structures. They likely arise from local overfitting to high-frequency training components and imperfect score estimation at low noise levels. Such effects are amplified in spectral regions with low signal-to-noise ratio and accumulate during iterative rollouts, ultimately limiting prediction horizons. We therefore introduce a transport-based correction that suppresses these oscillations while preserving physically meaningful flow structures, enabling longer and more stable predictions (up to $j = 250$ and possibly more). A detailed analysis of its impact on overall predictive performance is beyond the scope of this paper; instead, we focus on correcting the artifacts observed in Sect. 5.1 and Sect. 5.2.1 for (\mathcal{M}) , which has so far proven to be the most visually consistent method. The full ablation study, presented in Appendix H, nevertheless shows that such artifacts do emerge for sufficiently long time horizons. For completeness, we provide the full construction and intuition in Appendix C.1. It is controlled by two hyperparameters: α_R , which sets how many times the correction is applied; and α_T , which specifies how early in the backward diffusion process the correction begins (larger values apply it earlier, *i.e.* more steps before the final timestep). Together, they control the strength and timing of the correction during the generative process.

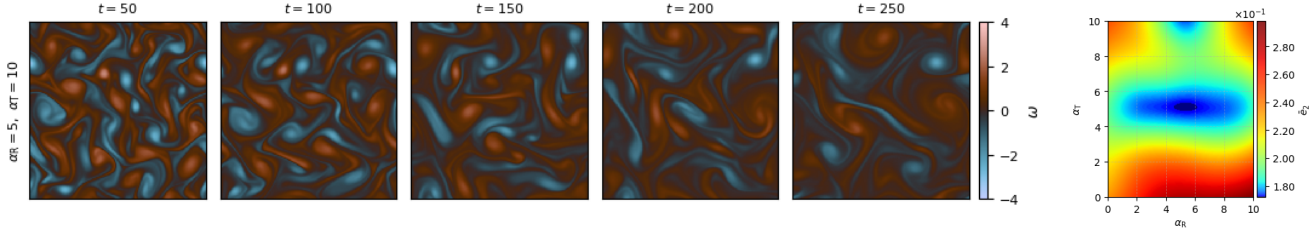


Figure 7: Long rollout prediction. Left panel: snapshots of vorticity inferred by diffusion model on divergence-free manifold (\mathcal{M}) using the transport-based corrector with hyperparameters $\alpha_R = 5$ and $\alpha_T = 10$. Right panel: α_R and α_T parameters and associated averaged e_2 metric.

The hyperparameters α_R and α_T are optimized as follows. Due to the high computational cost of parameter optimization, we restrict the search to a coarse grid of 15 configurations, as illustrated in Figure 7, and report the result according to e_2 . Although ground-truth trajectories are unavailable at such long time horizons, this strategy remains sufficient as clear trends emerge. Overall, the dominant factor governing performance is the step in the reverse ODE at which the correction is applied, controlled by α_T . When α_T is set to an early or intermediate stage of the reverse process, the correction already induces most of the observable improvement, effectively correcting the post-turnover prediction. In this regime, increasing the number of correction iterations (high α_R) yields diminishing returns, since the updates are driven by strong gradients and rapidly saturate.

Interestingly, an outlier configuration arises at larger α_T , which yields the longest stable rollout (see Appendix H) and is the one being shown in Figure 7. This confirms that α_R is not a critical factor as long as a suitable (early or mid) α_T is chosen: the correction has already reoriented the reverse dynamics in a favorable direction. Indeed, most of the modeling precision comes from the late reverse dynamics (or density collapse) [40, 101]. However, pushing the stability horizon further becomes more tricky. In this extreme regime, long rollouts remain achievable, but extending them requires a careful joint balance between an early α_T and the previously selected α_R . Achieving long stability increasingly relies on both consistent internal dynamics and transport correction.

Finally, two additional regimes can be identified. When the overall correction strength is too weak (low $\alpha_R \times \alpha_T$), residual ripples persist in the generated trajectories and may even be amplified. Conversely, when the correction is excessively strong (high $\alpha_R \times \alpha_T$), artifacts re-emerge, as the transport term dominates and suppresses the intrinsic free dynamics of the statistical model (see again Appendix H). At the end, we were able to push predictions up to $2.5 * j_{\text{max}}$ ($j = 250$), with no apparent signs of instability.

5.3. Out-of-distribution (OOD) tests

In these last experiments, the proposed methods are tested on two OOD sets, using the same physical time horizon as the one used during the training phase. This approach enables a clean evaluation of the performances of those methods. Details on the choice of simulation parameters are left to the Appendix A.2.

5.3.1. OOD generation

The two test cases considered to analyze the performances of generative methods for OOD configurations are the following.

Vortex superposition (VS). The initial velocity field $\mathbf{u}_{\text{VS}} = (u, v)$ is imposed directly as pure sinusoids:

$$\mathbf{u}_{\text{VS}} = A_{\text{VS}} \begin{pmatrix} -\sin\left(2\frac{y}{L}\right) \\ \sin\left(3\frac{x}{L}\right) \end{pmatrix}.$$

This yields a solenoidal shear-type vortex field consisting of pure Fourier modes $(0, 2)$ and $(3, 0)$ for u and v , respectively, without randomness but with perfect symmetry. It is commonly used as a simple analytical vortex initial condition for testing. This strong symmetry constraint ensures the model consistency with isotropic dynamics. OOD tests are constructed with arbitrary amplitudes A_{VS} that lie outside the range encountered during training. This deliberate amplitude mismatch makes prediction particularly challenging: even small autoregressive errors can amplify rapidly when the model is forced to operate in a dynamical regime it has never seen.

Perturbed Taylor–Green vortex (TGV). This test case consists in a two-dimensional incompressible velocity field constructed by starting from a canonical Taylor–Green vortex and adding a small, smooth low-frequency perturbation:

$$\mathbf{u}_0 = \begin{pmatrix} \sin(2k_0x) \cos(2k_0y) \\ -\cos(2k_0x) \sin(2k_0y) \end{pmatrix}, \quad k_0 = \frac{2\pi}{L}.$$

Since the pure Taylor–Green vortex is a stationary solution of incompressible flows, we add a random, mostly high-frequency perturbation to the initial field:

$$\mathbf{u}_{\text{TGV}} = A_{\text{TGV}} (\mathbf{u}_0 + \mathcal{P}\boldsymbol{\eta}), \quad \boldsymbol{\eta} \sim \mathcal{N}(\mathbf{0}, \mathbf{I}_n).$$

Here $A_{\text{TGV}} > 0$ is the amplitude of the vortex. This setting, apart from being standard in two-dimensional fluid tests, shows a clear regime transition and vortex-scale change, from low to large wavenumbers, creating localized coherent dynamics along the way. This well supports the OOD claim since it mixes a coherent TGV pattern with high-frequency noise, creating scale combinations the model was not trained on.

5.3.2. OOD results

Metrics. While visual inspection of the vorticity field can provide a qualitative sense of the rotational structures present in the flow, OOD conditions may induce subtle artifacts or distortions. To obtain a more satisfying characterization, one typically turns to other visual vortex identification metrics, among which the Q -criterion [102]:

$$Q = \frac{1}{2}(\boldsymbol{\Omega} : \boldsymbol{\Omega} - \mathbf{D} : \mathbf{D}), \quad (29)$$

where $\mathbf{D} = \nabla \otimes_s \mathbf{u} = \frac{1}{2}(\nabla \otimes \mathbf{u} + (\nabla \otimes \mathbf{u})^T)$ is the symmetric velocity rate tensor, $\boldsymbol{\Omega} = \nabla \otimes_a \mathbf{u} = \frac{1}{2}(\nabla \otimes \mathbf{u} - (\nabla \otimes \mathbf{u})^T)$ is the skew-symmetric rotation rate tensor, and $\mathbf{A} : \mathbf{B} = \sum_{i,j} A_{ij} B_{ij}$. In two dimensions ($d = 2$) one has:

$$\mathbf{D} = \frac{1}{2} \begin{bmatrix} 2\partial_x u & \partial_y u + \partial_x v \\ \partial_y u + \partial_x v & 2\partial_y v \end{bmatrix}, \quad \boldsymbol{\Omega} = \frac{1}{2} \begin{bmatrix} 0 & -\omega \\ \omega & 0 \end{bmatrix}.$$

The Q -criterion balances between the rotation rate and the strain rate and its positive iso-surfaces (or iso-values in two dimensions) display areas (or lines in two dimensions) where the strength of rotation overcomes the strain, highlighting the vortex envelopes. This criterion sharpens the depiction of vortex cores and enhances qualitative observations.

Results. Only the most representative results are shown for compactness. Additional plots of the snapshots inferred with all methods of Table 1 are displayed in Appendix I on Figure I.17 for the VS case, and on Figure I.18 for the TGV case. At first for the VS case, the Q -criterion provides a clearer visual insight into the amplitude distribution of the predicted flow fields, as seen in Figure 8. Overall, our proposed diffusion model on divergence-free manifold (\mathcal{M}) performs best, again. The vorticity field itself offers limited additional insight; however, it clearly demonstrates that symmetry is perfectly preserved, which is a very desirable geometry property, in addition to the divergence-free enforcement. Coherent structures are present across models, although they remain difficult to evaluate qualitatively. The Pearson correlation coefficient ρ_P , displayed alongside temporal averages in Figure 10, breaks this apparent tie and identifies (\mathcal{M}) as the best model, while also highlighting that other models such as (PC) and (SC) should not be overlooked. The atypical ρ_P trend, initially decreasing and then increasing, also highlights the peculiarity of this OOD setting, challenging our initial expectations. One might have expected mildly physically constrained methods, such as (PC), to dominate in this setting. Instead, the strict constrained model achieves the best performances, likely due to the complex symmetry patterns inherent to the VS configuration. In this setup, the vanilla EDM diffusion model (\mathcal{V}) is only outperformed by (\mathcal{M}).

This trend, however, does not hold for the TGV case, which instead supports the claim that softer divergence-free constraints are better suited for OOD generalization (also supported with the previous results), as they allow the model to satisfy physical constraints while retaining a sufficient degree of freedom. In this case, all models successfully capture the high to low wavenumber transition, as illustrated by the Q -criterion in Figure 9. Nevertheless, a clear amplitude disparity across vortices is observed, which is likely responsible for most of the prediction error, rather than strict divergence-free conditioning alone. Consequently, (PC) and (SC) models are favored, as expected, and we finally observe a boost in accuracy in (\mathcal{L}), as seen in Figure 11. In this regime, (\mathcal{L}) achieves the best overall performance, although it is closely matched by (PC) and (SC). Notably, (PC) is the only method that perfectly enforces the divergence-free constraint, which is the primary objective. By contrast, the strict divergence-free models (\mathcal{M}) and (\mathcal{D}) exhibit reduced variability, likely due to overfitting, an effect already discussed in Sect. 5.2, but beyond the scope of the present OOD analysis.

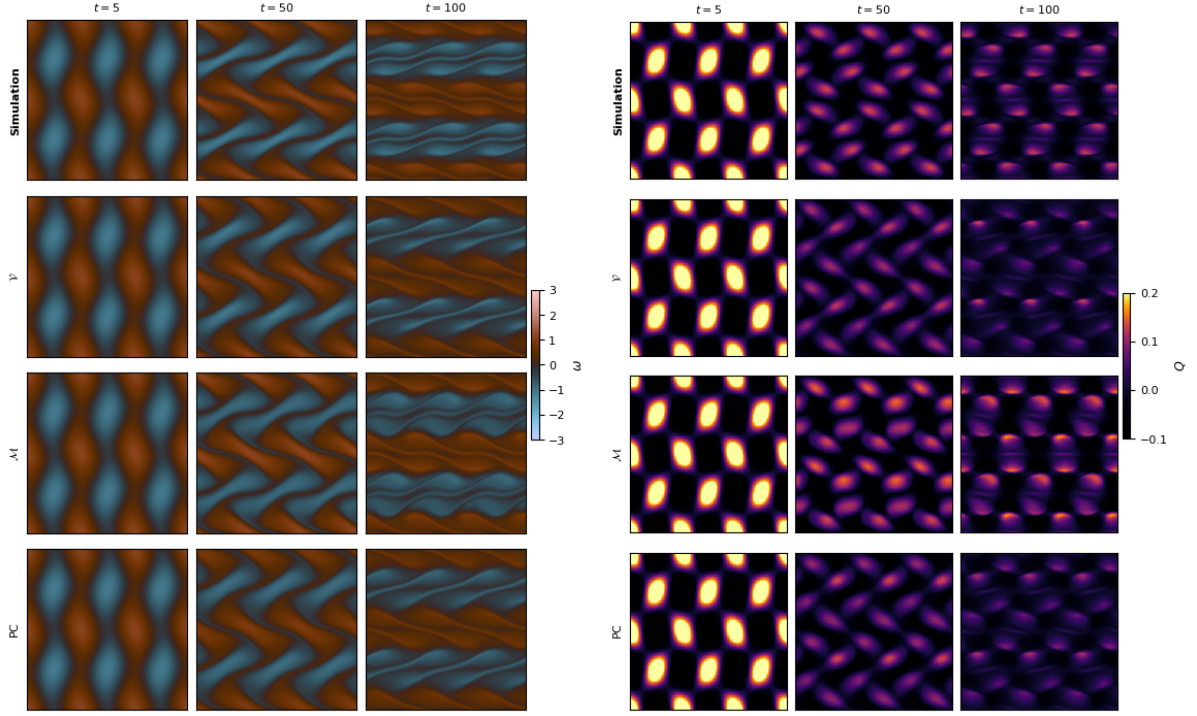


Figure 8: OOD tests on vortex superposition (VS): snapshots of the ground-truth solution (top row) against snapshots inferred by models (\mathcal{V}) , (\mathcal{M}) , and (PC) . Left panel: vorticity field. Right panel: Q -criterion.

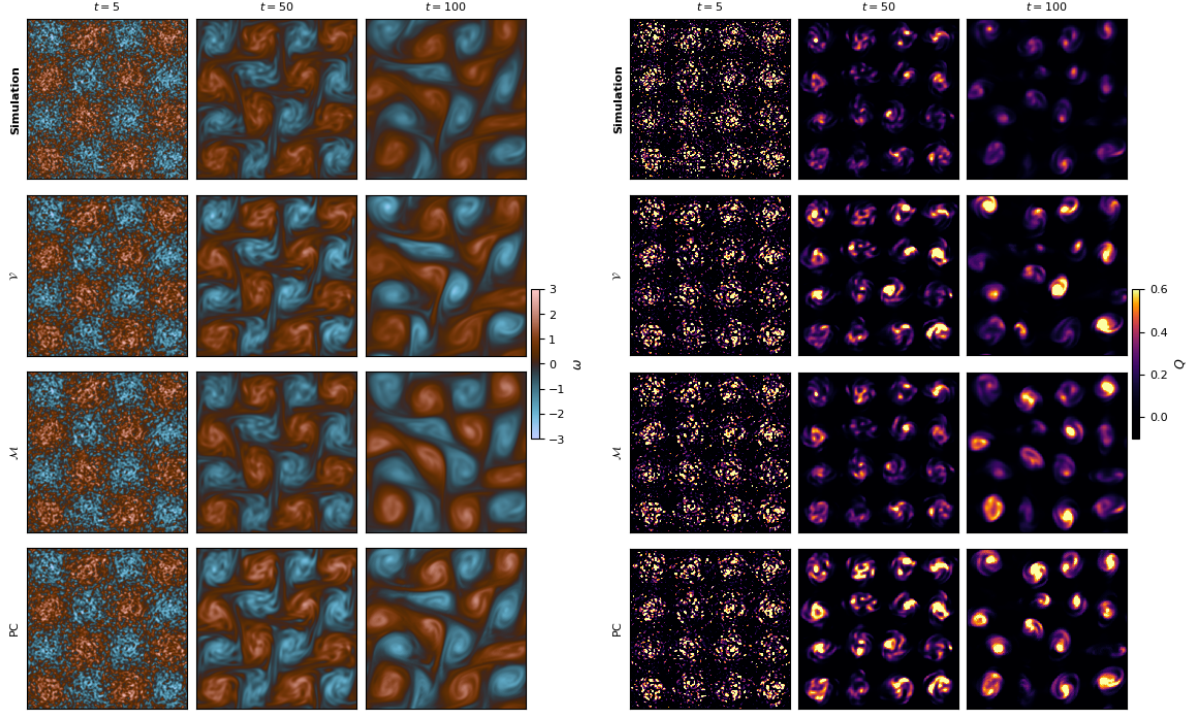


Figure 9: OOD tests on Taylor-Green vortex (TGV): snapshots of the ground-truth solution (top row) against snapshots inferred by models (\mathcal{V}) , (\mathcal{M}) , and (PC) . Left panel: vorticity field. Right panel: Q -criterion.

6. Conclusions and perspectives

In this work, we studied how physical constraints should be embedded into generative diffusion models for incompressible flow prediction, using Kolmogorov turbulence as a controlled yet informative benchmark. Building upon the plain EDM diffusion framework, we systematically compared a spectrum of divergence-free enforcement strategies, ranging from strict manifold-based formulations to soft guidance and post hoc corrections, across in-distribution, rollout, and out-of-distribution regimes.

A first key finding is that enforcing incompressibility at the level of the generative manifold yields the most accurate and physically consistent reconstructions in-distribution. The proposed manifold-based diffusion model (\mathcal{M}) consistently suppresses fine-scale numerical artifacts that arise in penalty-based or autoregressive formulations, achieving the lowest pointwise errors and the cleanest spectral behavior at short and moderate horizons. These results demonstrate that embedding physical constraints directly into the geometry of the generative process is more effective than enforcing them through auxiliary losses or penalties, particularly

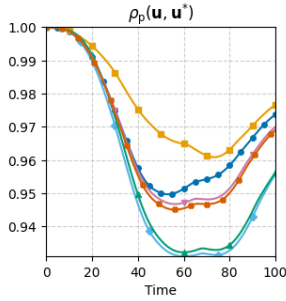


Figure 10: OOD test on vortex superposition (VS). Left panel: Pearson correlation coefficient ρ_P as a function of time. Right table: time-averaged mean-square error MSE, relative ℓ^2 error e_2 , and spectral divergence error ε_{div} . Legends: $(\mathcal{V}) \bullet$, $(\mathcal{M}) \blacksquare$, $(\mathcal{D}) \blacklozenge$, $(\mathcal{L}) \blacktriangle$, $(\text{SC}) \blacktriangledown$, $(\text{PC}) \times$.

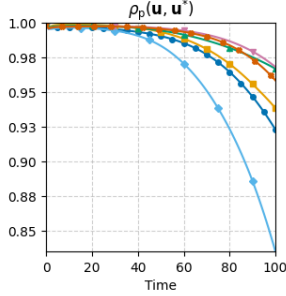


Figure 11: OOD test on Taylor-Green vortex (TGV). Left panel: Pearson correlation coefficient ρ_P as a function of time. Right table: time-averaged mean-square error MSE, relative ℓ^2 error e_2 , and spectral divergence error ε_{div} . Legends: $(\mathcal{V}) \bullet$, $(\mathcal{M}) \blacksquare$, $(\mathcal{D}) \blacklozenge$, $(\mathcal{L}) \blacktriangle$, $(\text{SC}) \blacktriangledown$, $(\text{PC}) \times$.

when local accuracy and structural fidelity are critical. At the same time, our experiments reveal a clear trade-off between strict and soft constraints as predictions are propagated in time or exposed to distributional and statistical metrics. In extended rollouts, the advantages of hard-constrained models gradually diminish as errors accumulate, whereas methods derived from the unconstrained vanilla EDM model, combined with divergence-free correction mechanisms, yield more accurate statistical behavior. In this context, predictor–corrector strategies such as (PC) provide an interesting compromise, achieving perfect incompressibility while preserving amplitude statistics and visual coherence. Out-of-distribution evaluations further confirm that no single constraint strategy dominates across all regimes. For moderately shifted configurations with strong geometric or symmetry constraints, strict manifold-based enforcement remains competitive and can even be advantageous. In contrast, for more severe distribution shifts, softer constraints offer the flexibility required to adapt to unseen dynamics, while overly rigid formulations tend to overfit and lose variability. These observations highlight that the effectiveness of physical constraints comes in pair with the degree of distributional overset encountered during inference.

Taken together, our findings establish a design principle for diffusion-based flow modeling: strict constraints are more effective near the training distribution and at short horizons, where precision and smoothness are critical, while softer constraints, or unconstrained models augmented with principled corrections, become preferable for long-horizon prediction and robust out-of-distribution generalization. Rather than competing paradigms, these approaches are complementary and should be combined depending on the target regime. While the present study is restricted to periodic domains and single-field velocity prediction, the proposed framework is general and extensible. Extending it to non-periodic geometries, coupled multi-field prediction, and more complex physical settings represents a natural next step. More broadly, viewing diffusion models through the lens of probability flow ODEs reveals deep conceptual connections with fluid dynamics itself, offering a promising foundation for future diffusion-based approaches in computational fluid mechanics.

Appendix A. Numerical methodology

Appendix A.1. Galerkin-Fourier simulation of a periodic flow

The simulation of periodic flows allow us to work with the Fourier exponentials basis \mathcal{E}_d of Sect. 2.1, in pair with Fourier expansions of the operators and vector fields [4]. The projected Stokes operator \mathbf{A}_N in Eq. (6) being simply diagonal in \mathcal{E}_d , one may write:

$$\nu \mathbf{A}_N \mathbf{u}_N(t) = -\nu \sum_{\mathbf{k} \in \mathcal{K}_N} \|\mathbf{k}\|^2 \mathbf{u}_{\mathbf{k}}(t) f_{\mathbf{k}}.$$

Besides, the finite-dimensional convective operator can be seen as a convolution within the Fourier domain with the Leray projection (7):

$$\mathbf{B}_N(\mathbf{u}_N)(t) = \sum_{\mathbf{k} \in \mathcal{K}_N} \mathbf{P}_{\mathbf{k}} \left(\sum_{\mathbf{p} + \mathbf{q} = \mathbf{k}} (\mathbf{i} \mathbf{q} \cdot \mathbf{u}_{\mathbf{p}}(t)) \mathbf{u}_{\mathbf{q}}(t) \right) f_{\mathbf{k}}.$$

In this regard, we observe that such a convolution spans a set \mathcal{K}_{2N} , larger than the initial one \mathcal{K}_N of cardinality $\#\mathcal{K}_N = \frac{1}{2}((2N+1)^d - 1)$. Apart from setting N below the Nyquist limit, *e.g.* $N < \frac{L}{2\Delta r}$ for Δr being the spatial discretization step, we must also compute the convective term onto a zero-padded set to support the full-convolution without increasing the number of modes [4, Chapter 3]. We define the zero-padded spectrum of the velocity field \mathbf{u} with Fourier coefficients $\{\tilde{\mathbf{u}}_{\mathbf{k}}\}_{\mathbf{k} \in \mathcal{K}_M}$ with $N_{\text{pad}} = N + \frac{1}{2}N$ and $M = \lceil N_{\text{pad}} \rceil_{\text{even}}$ (rounded to the nearest even integer) by:

$$\tilde{\mathbf{u}}_{\mathbf{k}} = \begin{cases} \mathbf{u}_{\mathbf{k}} & \text{if } \mathbf{k} \in \mathcal{K}_N, \\ \mathbf{0} & \text{if } \mathbf{k} \in \mathcal{K}_M \setminus \mathcal{K}_N. \end{cases}$$

Then the convective term is computed for the padded field $\tilde{\mathbf{u}}_N(t) = \sum_{\mathbf{k} \in \mathcal{K}_M} \tilde{\mathbf{u}}_{\mathbf{k}}(t) f_{\mathbf{k}}$ with formal discrete difference methods. The full time-marching scheme reads at time step $t_j = j\Delta t$, $j \in \mathbb{N}$:

$$\begin{cases} \mathbf{u}_{\mathbf{k}}^{(j+1)} = \mathbf{u}_{\mathbf{k}}^{(j)} - \left((\nu \|\mathbf{k}\|^2 + \alpha_{\mathbf{k}}) \mathbf{u}_{\mathbf{k}}^{(j)} + \langle \mathbf{B}_N(\tilde{\mathbf{u}}_N^{(j)}), f_{\mathbf{k}} \rangle \right) \Delta t, \\ \mathbf{u}_{\mathbf{k}}^{(0)} = \frac{i\mathbf{k}^\perp}{\|\mathbf{k}\|^2} \widehat{\omega}_F(\mathbf{k}), \end{cases} \quad (\text{A.1})$$

i.e. a simple (yet efficient) Euler scheme for $\mathbf{u}_{\mathbf{k}}^{(j)} \simeq \mathbf{u}_{\mathbf{k}}(t_j)$, provided a small timestep $0 < \Delta t \ll \frac{\Delta r^2}{\nu}$ is considered. Here $\widehat{\omega}_F(\mathbf{k})$ is the filtered initial vorticity field in Fourier space sampled according to Eq. (8).

Appendix A.2. Simulation and machine learning parameters

In this appendix, we list the parameters used for the simulation and data-processing throughout the paper. The numerical simulation global parameters are gathered in Table A.3. Parameters for the database generation are gathered in Table A.4.

Symbol	Definition	Value
L	Domain side length	2π
n	Spatial discretization	512^2
N	Frequency cut-off (ℓ^∞ frequency bound)	200
Δt	Time discretization step	1.0×10^{-4}
ν	Kinematic viscosity	5.0×10^{-4}
k_d	Drag force wavenumber (maximum range)	2
α	Friction coefficient	3.75×10^{-4}

Table A.3: Numerical parameters of Fourier-Galerkin simulation scheme.

Symbol	Description	Value
$H \times W$	Spatial resolution of velocity field (subsampled from simulation)	256^2
N'	Frequency cut-off (subsampled from simulation)	$N/2$
$[k_f, k_\nu]$	Initial energy spectrum range	[4, 13]
N_{IC}	Number of random simulation seeds drawn for the training base	10
N_t	Number of frames regularly sampled from a simulation (train set)	100
M_{IC}	Number of random simulation seeds drawn for in-distribution and rollout test base	3
M_{S}	Number of repeated diffusion model generation calls (different noise seeds) for the same task	5
A	Amplitude (in-distribution, rollout, long rollout)	0.25
A_{VS}	Vortex superposition amplitude	0.45
A_{TGV}	Perturbed Taylor-Green vortex amplitude	0.30

Table A.4: Numerical parameters used for dataset and machine learning applications.

Appendix B. EDM framework: training objective and implementation details

Here we give further details on the implementation of the EDM pipeline in Sect. 3.1. We basically follow the framework of [40]. The sampling distribution $\log \sigma \sim \mathcal{N}(\sigma_m, \Sigma^2)$ is considered in the EDM training loss (17) (focusing on intermediate noise levels with $\sigma_m = -1.2$ and $\Sigma = 1.2$). The weighting function is:

$$\lambda(\sigma) = \frac{1}{\sigma^2} + \frac{1}{\sigma_{\text{data}}^2}, \quad (\text{B.1})$$

for σ_{data}^2 being the variance of the data. The sampling procedure (19) is implemented along with:

$$\sigma_i = \left(\sigma_{\max}^{\frac{1}{\rho}} + \frac{i}{T-1} (\sigma_{\min}^{\frac{1}{\rho}} - \sigma_{\max}^{\frac{1}{\rho}}) \right)^{\rho},$$

with $\sigma_T = 0$, fixing $\rho = 7$, $\sigma_{\min} = 2 \cdot 10^{-3}$, and $\sigma_{\max} = 80$ for normalized data. Here ρ controls how much the steps near $\sigma_{\min} = \sigma_{T-1}$ (late backward iterates) are shortened compared to the longer ones near $\sigma_{\max} = \sigma_0$ (early backward iterates).

With this setting, the number of generative discretization steps $\{\sigma_i\}_{1 \leq i \leq T}$ is reduced to as few as $T = 25$, which is about 40 times fewer than some earlier implementations [23, 36, 33]. To achieve accuracy and smoothness comparable to, or even surpassing, the classical approach, we introduce a small number of correction steps near the end of the backward iterates when the denoiser operates at the finest scales. Empirically, we found that the mean-shift corrector is by far the most efficient and robust among the classical options (e.g. Langevin, annealed Langevin, etc.). The following corrector is thus applied for a few iterations towards the end of the backward process:

$$\tilde{U}_i \leftarrow \tilde{U}_i + \eta \left(-\tilde{U}_i + \mathbf{D}_{\theta} \cdot (\tilde{U}_i; \sigma_i) \right), \quad (\text{B.2})$$

where $\eta = 0.05 \times \sigma_i^2/2$, and it is repeated α_R times during the last α_T discrete noise scales σ_i of the backward ODE integration. The above corrector can be interpreted as a deterministic counterpart of the classical Langevin corrector [103]:

$$\tilde{U}_i \leftarrow \tilde{U}_i + \eta \nabla_{\mathbf{u}} \log p_{t_i}(\tilde{U}_i) + \sqrt{2\eta} \tilde{Z}, \quad \tilde{Z} \sim \mathcal{N}(\mathbf{0}, \mathbf{I}),$$

of which purpose is to nudge samples toward high-likelihood regions of the marginal distribution $p_t(\mathbf{u})$.

Alternatively the denoiser is parameterized by a preconditioned neural network \mathbf{F}_{θ} with a noise-dependent skip connection such that:

$$\mathbf{D}_{\theta}(\mathbf{u}; \sigma) = c_{\text{skip}}(\sigma) \mathbf{u} + c_{\text{out}}(\sigma) \mathbf{F}_{\theta}(c_{\text{in}}(\sigma) \mathbf{u}; c_{\text{noise}}(\sigma)). \quad (\text{B.3})$$

Skip connections modulate the denoiser output. Based on the value of the coefficients, either noise or input data can be predicted, as well as any noisy version in between. This choice helps to carefully modulate the amplitude of the noise to be removed at each diffusion time step. The training loss becomes:

$$\mathcal{L}_{\text{EDM}}(\theta) = \mathbb{E}_{\mathbf{u}_0 \sim \mu_{\text{data}}} \mathbb{E}_{\sigma \sim p(\sigma)} \mathbb{E}_{\mathbf{z} \sim \mathcal{N}(\mathbf{0}, \mathbf{I})} \left[\lambda(\sigma) c_{\text{out}}(\sigma)^2 \left\| \mathbf{F}_{\theta}(c_{\text{in}}(\sigma)(\mathbf{u}_0 + \sigma \mathbf{z}); c_{\text{noise}}(\sigma)) - \mathbf{F}_{\text{target}}(\mathbf{u}_0, \mathbf{z}; \sigma) \right\|^2 \right]$$

where the effective training target $\mathbf{F}_{\text{target}}$ is:

$$\mathbf{F}_{\text{target}}(\mathbf{u}_0, \mathbf{z}; \sigma) = \frac{1}{c_{\text{out}}(\sigma)} (\mathbf{u}_0 - c_{\text{skip}}(\sigma)(\mathbf{u}_0 + \sigma \mathbf{z})),$$

and the functions c_{skip} , c_{out} , c_{in} , and c_{noise} are:

$$c_{\text{skip}}(\sigma) = \frac{\sigma_{\text{data}}^2}{\sigma^2 + \sigma_{\text{data}}^2}, \quad c_{\text{in}}(\sigma) = \frac{1}{\sqrt{\sigma^2 + \sigma_{\text{data}}^2}}, \quad c_{\text{out}}(\sigma) = \frac{\sigma \sigma_{\text{data}}}{\sqrt{\sigma^2 + \sigma_{\text{data}}^2}}, \quad c_{\text{noise}}(\sigma) = \frac{1}{4} \log \sigma.$$

The weighting function λ is the one given by Eq. (B.1). These choices ensure that the training inputs of \mathbf{F}_{θ} have unit variance: $\mathbb{V}[c_{\text{in}}(\sigma)(\mathbf{u}_0 + \sigma \mathbf{z})] = 1$; the effective training target $\mathbf{F}_{\text{target}}$ has unit variance alike; c_{skip} minimizes c_{out} , so that the errors of \mathbf{F}_{θ} are amplified as little as possible; and the weighting function $\lambda(\sigma) c_{\text{out}}(\sigma)^2 = 1$ for all noise levels σ . In other words c_{skip} and c_{noise} weight the skip connection and noise levels, respectively, whereas c_{in} and c_{out} scale the input and output magnitudes.

Appendix C. Correctors for diffusion models

Appendix C.1. Mitigating stiff artifacts in long-horizon rollouts

As shown in Sect. 5.1 and Sect. 5.2.1, artifacts arise during backward integration and are amplified by autoregression. We therefore introduce a correction strategy based on predictor–corrector sampling, inspired by transport consistency and gradient filtering in numerical fluid modeling and signal processing. In score-based generative models, predictor–corrector schemes stabilize reverse-time sampling by enforcing consistency with backwards dynamics [33], a principle also supported by multi-step and transport-aware SDE solvers [104]. Related ideas appear in semi-Lagrangian fluid schemes, where past state aligns updates with transport directions [105]. To suppress ripple artifacts, we draw inspiration from total variation denoising [106], and gradient-domain filtering, which attenuate spurious high-frequency oscillations while preserving structure through time displacement [107] (anisotropic diffusion/optical flow techniques). Together, these works motivate our use of past-state projection for transport alignment and gradient smoothing for artifact attenuation.

Observations and prior. Empirically, we observe spatially localized artifacts (or patches) that appear visually *opposed* to the flow, clashing with the expected continuous transport motion. These errors manifest as stripe-like oscillations, visually high-frequency compared to larger coherent structures, and tend to appear at unexpected times during autoregression, where they are further amplified once present. Although localized, they often span a non-negligible portion of the domain and thus cannot be regarded as simple transport errors, but rather as the result of imperfect evaluations. From a physical standpoint, transport equations generate spatially coherent dynamics, with no spurious localized events unless externally forced. In hyper-viscous and decaying regimes, the dynamics are dominated by large-scale structures (*e.g.* the growth of vortices in Figure 5) and evolve smoothly through gradual increments; abrupt, localized stiff bursts violate this behavior. In the diffusion model setting, the learned score is inherently imperfect, and reverse-time integration and autoregressive sampling amplify errors over time, particularly at low noise levels where fine-scale details dominate. However, the combination of diffusion and autoregression provides access not only to past states but also to the underlying dynamics encoded by the score, enabling transport-consistent correction and selective suppression of dynamically inconsistent artifacts.

Key deductions and correction mechanism. If the model is (to a certain extent) accurate and reconstruction is objectively coherent, the instantaneous state increment:

$$\overset{\leftarrow}{\delta}_\sigma^{(j)} := (\overset{\leftarrow}{U}_\sigma | (\mathbf{u}^{(j)})^*)^* - (\mathbf{u}^{(j-1)})^*$$

evaluated at low noise level σ is dominated by the transport direction, with a small residual error. In this regime, the dominant component is low-frequency, while residual noise from imperfect score estimation is typically high-frequency and amplified during reverse integration. Hence, projecting the score via:

$$\Pi_\delta^{(j)} := \frac{\overset{\leftarrow}{\delta}_\sigma^{(j)} \otimes \overset{\leftarrow}{\delta}_\sigma^{(j)}}{\|\overset{\leftarrow}{\delta}_\sigma^{(j)}\|^2 + \varepsilon},$$

with some small $\varepsilon > 0$, aligns the dynamics with the transport-consistent direction encoded by $\overset{\leftarrow}{\delta}_\sigma^{(j)}$ and suppresses incoherent components. This projection is valid once the update becomes transport-dominated, *i.e.*, at sufficiently low noise σ near the end of backward integration of Eq. (23). Furthermore, spurious high-frequency bursts along this direction are detected using the relative gradient growth rather than its absolute magnitude, since sharp structures may be physical. We thus define localized gradient norms:

$$G_\sigma^{(j)} = \left\| \nabla (\overset{\leftarrow}{U}_\sigma | (\mathbf{u}^{(j)})^*)^* - \nabla (\mathbf{u}^{(j-1)})^* \right\|^2, \quad G_{\text{ref}} = \left\| \nabla (\mathbf{u}^{(j-1)})^* \right\|^2,$$

where $\|\cdot\|$ is taken pixel-wise, as well as a smoothed mask $\mathbf{m} := \Gamma[\mathbf{1}(G_\sigma^{(j)} > G_{\text{ref}})]$, where $\mathbf{1}$ is a binary indicator and Γ a smoothing kernel to avoid reintroducing sharp gradients [107]. Then we introduce the second projector:

$$\Pi_G^{(j)} := \mathbf{I} - \gamma \mathbf{m},$$

which selectively attenuate (to a factor $0 < 1 - \gamma < 1$, where γ is set to 0.8) spurious, non-transport high-frequency artifacts without harming coherent structures. Finally, as observed in [40, 46], increasing task difficulty (such as forecasting a long rollout) amplifies the benefit of stochasticity during backward integration. Noise injection introduces controlled thermal energy that enables re-exploration, thereby improving diversity and robustness during this stiff regime. This stochasticity selectively restores effective degrees of freedom without reintroducing numerical instabilities. Overall, the correction step (B.2) now reads (for the backward integration step i on the physical frame j):

$$\overset{\leftarrow}{U}_i \leftarrow \overset{\leftarrow}{U}_i + \eta \cdot \Pi_G^{(j)} \circ \Pi_\delta^{(j)} \circ \mathbf{s}_\theta \cdot (\overset{\leftarrow}{U}_i; \sigma_i) + \sqrt{2\eta} \cdot \Pi_\delta^{(j)} \overset{\leftarrow}{Z}, \quad \overset{\leftarrow}{Z} \sim \mathcal{N}(\mathbf{0}, \mathbf{I}),$$

and it is repeated, just like in Appendix B, α_R times during the last α_T scales. Here $\eta \propto \sigma_i^2/2$ [103], the same parameter as the one used in the mean-shift corrector (B.2), and $\mathbf{s}_\theta(\mathbf{u}; \sigma) = \frac{1}{\sigma^2}(-\mathbf{u} + \mathbf{D}_\theta(\mathbf{u}; \sigma))$. In effect, the dynamics are constrained to a coherent, autoregressive evolution direction. Gradient-based masking selectively damps localized high-frequency tangent modes that persist after projection, while smoothing enforces a locality prior reflecting the localized nature of artifacts. Noise then recovers global flexibility without destabilizing the dynamics.

Appendix C.2. Out-of-distribution energy regulation in autoregressive correction

In order to prevent amplitude blow-up resulting from autoregressive error accumulation, a simple yet effective kinetic-energy corrector can be implemented. Apart from the governing PDE, no additional information is assumed when predicting the system behavior on OOD inputs. The corrector solely enforces consistency with the established physical laws, without introducing any external or non-physical priors. This design is implemented by first computing the energy dissipation rate, ignoring the bilinear convective operator \mathcal{B} which is conservative and does not modify the total kinetic energy. One first has:

$$\begin{aligned} \frac{d\mathbf{u}_k}{dt} &= -\nu \|\mathbf{k}\|^2 \mathbf{u}_k(t) + \mathbf{f}_k(t) + (\text{conservative convective terms}) \\ &= -(\nu \|\mathbf{k}\|^2 + \alpha_k) \mathbf{u}_k(t) \\ &= -d_k \mathbf{u}_k(t), \end{aligned}$$

where α_k is the friction coefficient (10) in Fourier space. Then, take the modal energy $E_k = \frac{1}{2} \|\mathbf{u}_k\|^2$ and compute the instantaneous change in time:

$$\begin{aligned} \frac{dE_k}{dt} &= \mathbf{u}_k \cdot \frac{d\mathbf{u}_k}{dt} \\ &= -d_k \|\mathbf{u}_k\|^2 \\ &= -2d_k E_k, \end{aligned}$$

and therefore, the target modal energy at the time step $j + 1$ from the modal energy $E_{\mathbf{k}}^j = E_{\mathbf{k}}^*(j\Delta t)$ at the time step j is $E_{\mathbf{k}}^{\text{target}} = E_{\mathbf{k}}^j \exp(-2d_{\mathbf{k}}\Delta t)$; here $E_{\mathbf{k}}^* = \frac{1}{2} \|\mathbf{u}_{\mathbf{k}}^*\|$ where \mathbf{u}^* is again the predicted velocity field. Letting:

$$\gamma_{\mathbf{k}} = \sqrt{\frac{E_{\mathbf{k}}^{\text{target}}}{E_{\mathbf{k}}^{j+1}}} ,$$

the corrector step is defined as follows (only targeting deviations of the energy increments with a $\pm 5\%$ rate, potentially keeping defect signature of each method):

$$(\mathbf{u}_{\mathbf{k}}^{(j+1)})^* \leftarrow \text{clip}(\gamma_{\mathbf{k}}, 0.95, 1.05) \times (\mathbf{u}_{\mathbf{k}}^{(j+1)})^*. \quad (\text{C.1})$$

As a side note, the data being normalized prior to being input in the model *i.e.*:

$$\mathbf{u}_{\text{normalized}} = \frac{\mathbf{u} - \bar{\mathbf{u}}}{\|\mathbf{u} - \bar{\mathbf{u}}\|_2} ,$$

where $\bar{\mathbf{u}}$ stands for the empirical average of the data frames in \mathbb{R}^n , which is $\bar{\mathbf{u}} \approx \mathbf{0}$ from isotropy and zero-mean field property, we apply the filtering (C.1) for frames \mathbf{u} in physical units.

Appendix D. Machine learning configuration and hyperparameters

Below is a list of the parameters used for the machine learning experiments, as well as the correctors. As a side note, whenever an optimization is required (training and sampling), the vanilla method (\mathcal{V}) is always optimized on the first prediction frame. Once the vanilla method has reached its optimal parameters, all other methods retain these very parameters. This approach ensures that all comparisons are conducted fairly by prioritizing the baseline model and allows discrepancies relative to the vanilla method to be clearly distinguished.

Machine learning, training phase. While training can be performed on a typical workstation, equipped with a multi-core CPU,

Variable name (numerical)	Description	Value
epochs	Number of training epochs	750
lr	Initial learning rate	3.0×10^{-4}
batch_size_train	Training batch size	12
batch_size_valid	Validation batch size	5
stop	Early stopping patience (iterations)	120
patience	Learning rate scheduler patience	25
factor	Learning rate decay factor	0.75
precision	Numerical precision (bits)	32
clipVal	Gradient clipping threshold	1.0

Table D.5: Training hyperparameters and optimization settings used for experiments.

16–32 GB of system RAM, and a single consumer-grade GPU, the training phase for the multiple models is conducted on a high-performance computing node. This node is equipped with 96 GB of system RAM and two NVIDIA HGX A100 GPUs, each providing 80 GB of HBM2e VRAM.

Machine learning, sampling phase. The sampling phase is executed on a standalone computer, featuring 32GB of system RAM, an

Experiment section	α_R (repetitions)	α_T (tail)
In-distribution (Sect. 5.1)	2	5
Short-horizon rollout (Sect. 5.2.1)	2	5
Long-horizon rollout (Sect. 5.2.2)	5	10
Out-of-distribution (Sect. 5.3)	4	8

Table D.6: Corrector parameters specific to evaluation regimes.

AMD Ryzen 7 3700X processor, and an ASUS NVIDIA GeForce RTX 3090 GPU (24GB of GDDR6X VRAM). The sampling process can also be performed on a more modest workstation, provided that a GPU and at least 16 GB of system RAM are available.

Appendix E. Model design and architecture

In this appendix, we describe the main architectural choices of the neural network which has been implemented, emphasizing its differences from the standard U-Net [87, 88] and its use in an EDM-style framework.

Appendix E.1. Conditional generation

The autoregressive setup enables the generation of a complete, coherent flow time series by requiring each predicted step j to be conditioned on the previous step $j - 1$. This is achieved through the use of a concatenated input:

$$\mathbf{x}_{\text{in}} = \text{Concat} \left[\vec{U}_t | \vec{U}_0 = \mathbf{u}^{(j)}, \mathbf{u}^{(j-1)} \right] \in \mathbb{R}^{B \times 2C \times H \times W} ,$$

where B is the batch size, C is the channel size (or state dimension, $C = 2$ in our case since the fluid medium is the torus \mathbb{T}^2), H and W stand for the height and width of the discretized field, respectively (with $2 \times H \times W = n$ since $\vec{U}_0 \in \mathbb{R}^n$).

Appendix E.2. EDM noise embedding and low- σ refinement

The noise level σ being key to the sample's inner diffusion step and gradient strength, we embed it using log-Fourier features:

$$\mathbf{e}_t = \text{MLP} \left(\left[\log \sigma, (\log \sigma)^2, \sin(\omega_k \log \sigma), \cos(\omega_k \log \sigma) \right]_{k=1, \dots, K} \right),$$

$$\omega_k = \exp(\text{linspace}(\log 0.1, \log 1000, K)),$$

where MLP stands for Multi-Layer Perceptron, which provides stable conditioning across the full noise range. To improve predictions in the low-noise limit, we also apply a gated refinement on the earliest high-resolution skip:

$$\mathbf{y}_{\text{ref}} = \mathbf{y}_{\text{out}} + g(\mathbf{e}_t) \cdot \text{CU}(\mathbf{x}_{\text{skip}}, \mathbf{e}_t),$$

where \mathbf{y}_{out} is the output of the entire U-Net before refinement; \mathbf{x}_{skip} is the tensor taken before downsampling, at the earliest stage of processing (U-net's main down/up-sampling pipeline); g is a learned scalar gate controlling refinement strength; and CU is a small conditional U-Net block. This approach introduces a σ -dependent correction mostly absent from standard U-Net architectures.

Appendix E.3. Condition embedding and periodic boundaries

The noise embedding \mathbf{e}_t (conditioning vector) obtained from σ gets input in each residual block (U-Net's up and down encoder/decoder pipeline), which in turn, are modulated via:

$$\text{Block}(\mathbf{x} | \mathbf{e}_t) = \mathbf{x} + \text{Rem}(\text{DSConv}(\text{SiLU}(\text{FiLM}(\mathbf{x}, \mathbf{e}_t))), \mathbf{e}_t),$$

$$\text{FiLM}(\mathbf{x}, \mathbf{e}_t) = \text{GN}(\mathbf{x}) \cdot (1 + \gamma(\mathbf{e}_t)) + \beta(\mathbf{e}_t),$$

where Rem encapsulate basic linear operations (convolutions and activations), DSConv is a Depthwise Separable Convolution, SiLU is a Sigmoid Linear Unit, GN is a Group Normalization (proven efficient for diffusion) and γ, β are the scale and shift coefficients from the FiLM (Feature-wise Linear Modulation [94]) module learned from \mathbf{e}_t . Classical U-Net blocks use plain Conv-ReLU-Conv, while EDM blocks use FiLM-modulated GroupNorm-SiLU-DSConv. Furthermore, the data being periodic at its boundaries, all 3×3 depthwise (*i.e.*, each channel) convolutions are built with periodic spatial padding:

$$\text{DSConv}(\mathbf{x})_{b,c,i,j} := \mathbf{y}_{b,c}(i, j) = \sum_{u=-1}^1 \sum_{v=-1}^1 w_{c,u,v} \cdot \mathbf{x}_{b,c}((i+u) \bmod [H], (j+v) \bmod [W]),$$

followed by a 1×1 pointwise projection. This ensures wrap-around continuity and avoids boundary artifacts typical of zero padding.

Appendix F. Divergence-free diffusion process

In this section, we provide a simple illustration of how classical diffusion processes can be adapted to the divergence-free manifold, thereby enabling the derivation of the EDM setup of Sect. 4. To this end, we start from the standard infinite-dimensional Ornstein–Uhlenbeck (OU) process and modify it to fit the incompressible flow setting of Sect. 2.1. This adaptation naturally leads to the formulation of a diffusion framework constrained to divergence-free fields, from which the EDM construction follows.

Let \mathcal{U} be a separable Hilbert space with scalar product $\langle \cdot, \cdot \rangle$; for instance, $\mathcal{U} = L^2(\mathcal{O}, \mathbb{R}^d)$ the set of square-integrable \mathbb{R}^d -valued vector fields on the torus $\mathcal{O} = \mathbb{T}^d$, which is precisely the functional setting considered in the framework of Sect. 2.2. Let $\mathcal{G} : \text{Dom}(\mathcal{G}) \subset \mathcal{U} \rightarrow \mathcal{U}$ be a linear operator, we assume that \mathcal{G} generates a strongly continuous semigroup $\{e^{t\mathcal{G}}\}_{t \geq 0}$ on \mathcal{U} . Also let $\mathcal{Q} \in \mathcal{L}(\mathcal{U})$ be a bounded, symmetric, positive non negative operator that is trace-class on \mathcal{U} , then $\mathcal{S} := \sqrt{\mathcal{Q}}$ is a Hilbert–Schmidt operator on \mathcal{U} , so it is an integral operator. Let $(W_t, t \geq 0)$ denote a cylindrical Wiener process on \mathcal{U} defined in some filtered probability space $(\Omega, \mathcal{F}, \{\mathcal{F}_t\}_{t \geq 0}, \mathbb{P})$. The infinite-dimensional Ornstein–Uhlenbeck (OU) process $(U_t, t \geq 0)$ with values in \mathcal{U} is then defined by the SDE:

$$\begin{cases} d\vec{U}_t = \mathcal{G}\vec{U}_t dt + \sqrt{\mathcal{Q}}d\vec{W}_t, \\ \vec{U}_0 \in \mathcal{U}, \end{cases} \quad (\text{F.1})$$

which admits a mild solution [108, 109]:

$$\vec{U}_t = e^{t\mathcal{G}}\vec{U}_0 + \int_0^t e^{(t-s)\mathcal{G}} \sqrt{\mathcal{Q}}d\vec{W}_s. \quad (\text{F.2})$$

It is a Gaussian process in \mathcal{U} conditionally on \vec{U}_0 , with conditional mean and variance:

$$\mathbb{E}[\vec{U}_t | \vec{U}_0] = e^{t\mathcal{G}}\vec{U}_0, \quad \mathbb{V}[\vec{U}_t | \vec{U}_0] = \int_0^t e^{(t-s)\mathcal{G}} \mathcal{Q} e^{(t-s)\mathcal{G}^*} ds, \quad (\text{F.3})$$

respectively. Now introduce the closed subspace \mathcal{H} of \mathcal{U} of divergence-free fields defined by:

$$\mathcal{H} := \{\mathbf{u} \in \mathcal{U}; \nabla \cdot \mathbf{u} = 0\} \subset \mathcal{U},$$

and denote by $\mathcal{P} : \mathcal{U} \rightarrow \mathcal{H}$ the Leray projection operator of Eq. (3), which is the orthogonal projection in \mathcal{U} onto divergence-free fields. It satisfies $\mathcal{P}^2 = \mathcal{P}$ as a projector and is bounded, with range space $\text{Ran}(\mathcal{P}) = \mathcal{H}$. For $\mathbf{u} \in \text{Dom}(\mathcal{G}) \cap \mathcal{H}$ we then define the projected drift operator $\mathcal{A} : \text{Dom}(\mathcal{A}) \subset \mathcal{H} \rightarrow \mathcal{H}$ such that:

$$\mathcal{A}\mathbf{u} := \mathcal{P}(\mathcal{G}\mathbf{u}),$$

and the projected covariance operator $\mathcal{C} : \mathcal{U} \rightarrow \mathcal{H}$ such that:

$$\sqrt{\mathcal{C}}\mathbf{u} := \mathcal{P}(\sqrt{\mathcal{Q}}\mathbf{u}).$$

The OU process constrained to \mathcal{H} thus reads:

$$\begin{cases} d\vec{U}_t = \mathcal{A}\vec{U}_t dt + \sqrt{\mathcal{C}}d\vec{W}_t, \\ \vec{U}_0 \in \mathcal{H}. \end{cases} \quad (\text{F.4})$$

It follows that $\vec{U}_t | \vec{U}_0$ is Gaussian with the same semigroup transition operator as in Eq. (F.2) but restricted to \mathcal{H} , namely $\{e^{t\mathcal{A}}\}_{t \geq 0}$, and:

$$\vec{U}_t = e^{t\mathcal{A}}\vec{U}_0 + \int_0^t e^{(t-s)\mathcal{A}}\sqrt{\mathcal{C}}d\vec{W}_s. \quad (\text{F.5})$$

If $\vec{U}_0 \in \mathcal{H}$, then $\vec{U}_t \in \mathcal{H}$ for all $t \geq 0$ almost surely, since both the drift and covariance operators \mathcal{A} and \mathcal{C} , respectively, remain tangent to \mathcal{H} .

Now let $\{\mathbf{e}_i\}_{i \in \mathbb{N}}$ be an orthonormal basis of \mathcal{H} , and introduce the Galerkin projector $\pi_N : \mathcal{H} \rightarrow \mathcal{H}_N$ onto the finite dimensional subset $\mathcal{H}_N = \text{span}\{\mathbf{e}_{i_1}, \dots, \mathbf{e}_{i_N}\}$ of \mathcal{H} defined by:

$$\pi_N := \sum_{n=1}^N \mathbf{e}_{i_n} \otimes \mathbf{e}_{i_n}, \quad (i_1, \dots, i_N) \in \mathbb{N}^N.$$

The N -th order Galerkin approximation of the divergence-free OU process is then given by:

$$\begin{cases} d\mathbf{U}_t^N = \mathbf{A}_N \mathbf{U}_t^N dt + \sqrt{\mathbf{C}_N} d\vec{W}_t, \\ \mathbf{U}_0^N \in \mathcal{H}_N, \end{cases} \quad (\text{F.6})$$

where $\mathbf{U}_t^N := \pi_N \vec{U}_t$, and the drift operator $\mathbf{A}_N : \mathcal{H}_N \rightarrow \mathcal{H}_N$ and covariance operator $\mathbf{C}_N : \mathcal{U} \rightarrow \mathcal{H}_N$ are defined by:

$$\mathbf{A}_N = \pi_N \mathcal{A} \pi_N^*, \quad \sqrt{\mathbf{C}_N} = \pi_N \sqrt{\mathcal{C}}.$$

The \mathbb{R}^N -valued stochastic process $(\mathbf{U}_t^N, t \geq 0)$ is again an OU process on \mathcal{H}_N , which is conditionally Gaussian with explicit conditional mean and covariance. Galerkin projections have been used to prove the existence of (weak) martingale solutions of SDEs of the form of Eq. (F.4) with continuous non-linear drift and additive or multiplicative noise; see *e.g.* [9] or [108, Chapter 8]. Strong solutions may be constructed alike, which may be approximated by Galerkin expansions in the mean-square sense; see *e.g.* [110]. In summary, the Leray projection ensures that both the drift and diffusion operators remain divergence-free, and that the Galerkin truncation provides a consistent finite-dimensional approximation of the divergence-free OU process. This construction provides with a rigorous basis for the formulation of (latent) diffusion models constrained to incompressible fields.

Appendix G. Additional results: in-distribution assessment

Appendix G.1. Additional metrics

Following the notations introduced in Sect. 5.1, we further consider additional standard error metrics to complement the analysis. In particular, we employ the mean-squared error (MSE) and the mean absolute error (MAE). For completeness, we also report write their relative variants (rMSE and rMAE), which normalize the error with respect to the magnitude of the true values, as well as their relative-root counterparts (rRMSE and rRMAE), providing scale-adjusted measures that facilitate comparisons across models and datasets. These metrics are defined in terms of the ℓ^1 semi-norm $|\cdot|_1$ and the ℓ^2 norm $\|\cdot\|_2$ of vectors of \mathbb{R}^n by:

$$\begin{aligned} \text{MSE} &= \frac{1}{n} \|\mathbf{u} - \mathbf{u}^*\|_2^2, & \text{rMSE} &= \frac{1}{n} \frac{\|\mathbf{u} - \mathbf{u}^*\|_2^2}{\|\mathbf{u}\|_2^2}, & \text{rRMSE} &= \sqrt{\text{rMSE}}, \\ \text{MAE} &= \frac{1}{n} |\mathbf{u} - \mathbf{u}^*|_1, & \text{rMAE} &= \frac{1}{n} \frac{|\mathbf{u} - \mathbf{u}^*|_1}{|\mathbf{u}|_1}, & \text{rRMAE} &= \sqrt{\text{rMAE}}. \end{aligned}$$

The MSE measures the average squared deviation between predictions and true values, penalizing large errors more strongly. In contrast, the MAE computes the average absolute deviation and deals with all errors uniformly, making it less sensitive to outliers. In addition to classical pointwise metrics such as the MSE, we report the relative amplitude rA , which quantifies the agreement between predicted and reference fields in terms of their global ℓ^2 norm:

$$rA = \frac{\|\mathbf{u}^*\|_2}{\|\mathbf{u}\|_2 + \varepsilon},$$

where values closer to 1 indicate better agreement between the predicted and reference amplitudes.

Appendix G.2. Additional plots

In this section, we add a variety of additional plots for the in-distribution results, see Figure G.12. We also add the full predictions, see Figure G.13.

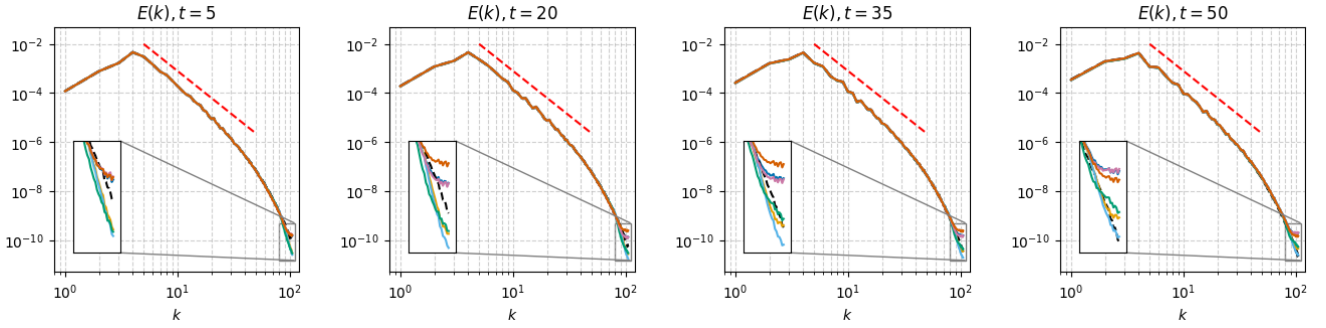


Figure G.12: In-distribution assessment: TKE spectra $k \mapsto E(k)$ at multiple time instances. Legends: — (V), — (M), — (D), — (L), — (SC), — (PC), - - ground truth spectrum, $-k^{-3-\delta}$ slope.

Appendix H. Additional results: rollout predictions

In this section, we add a variety of plots for the rollout results, see Figure H.14 and Figure H.15. We also provide the long rollout test curls (vorticities); see Figure H.16.

Appendix I. Additional results: OOD tests

In this section, we add a variety of plots for OOD results, see Figure I.17 for the VS case and Figure I.18 for the TGV case. Interestingly, in this setting, we can observe a small instability at the beginning of the flow prediction for (L), as seen in Figure I.17, which is probably due to a lack of model accuracy (and thus, residual noise).

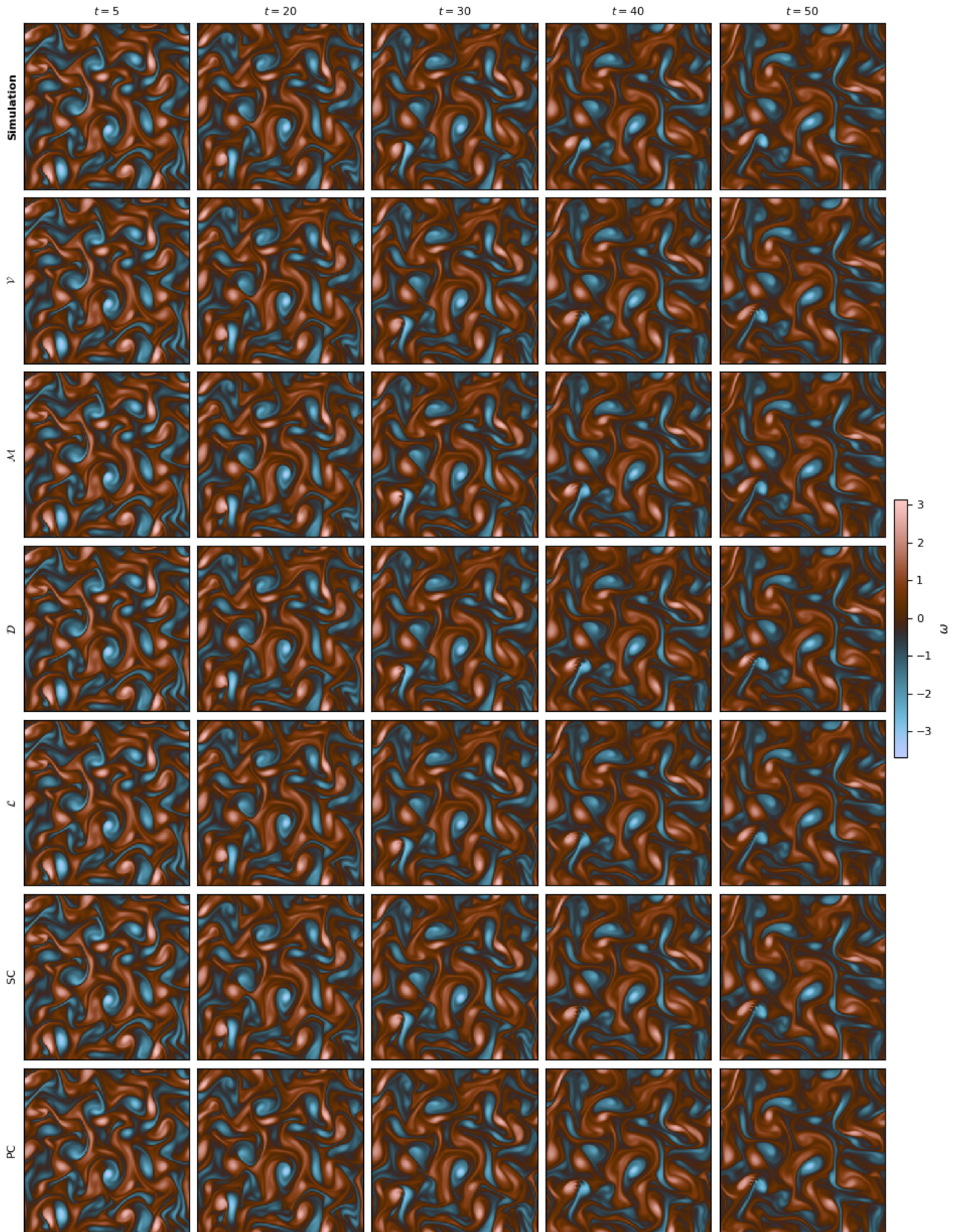


Figure G.13: In-distribution assessment: snapshots of the ground-truth solution (vorticity, top row) against snapshots inferred by all models (v), (M), (D), (L), (SC), and (PC).

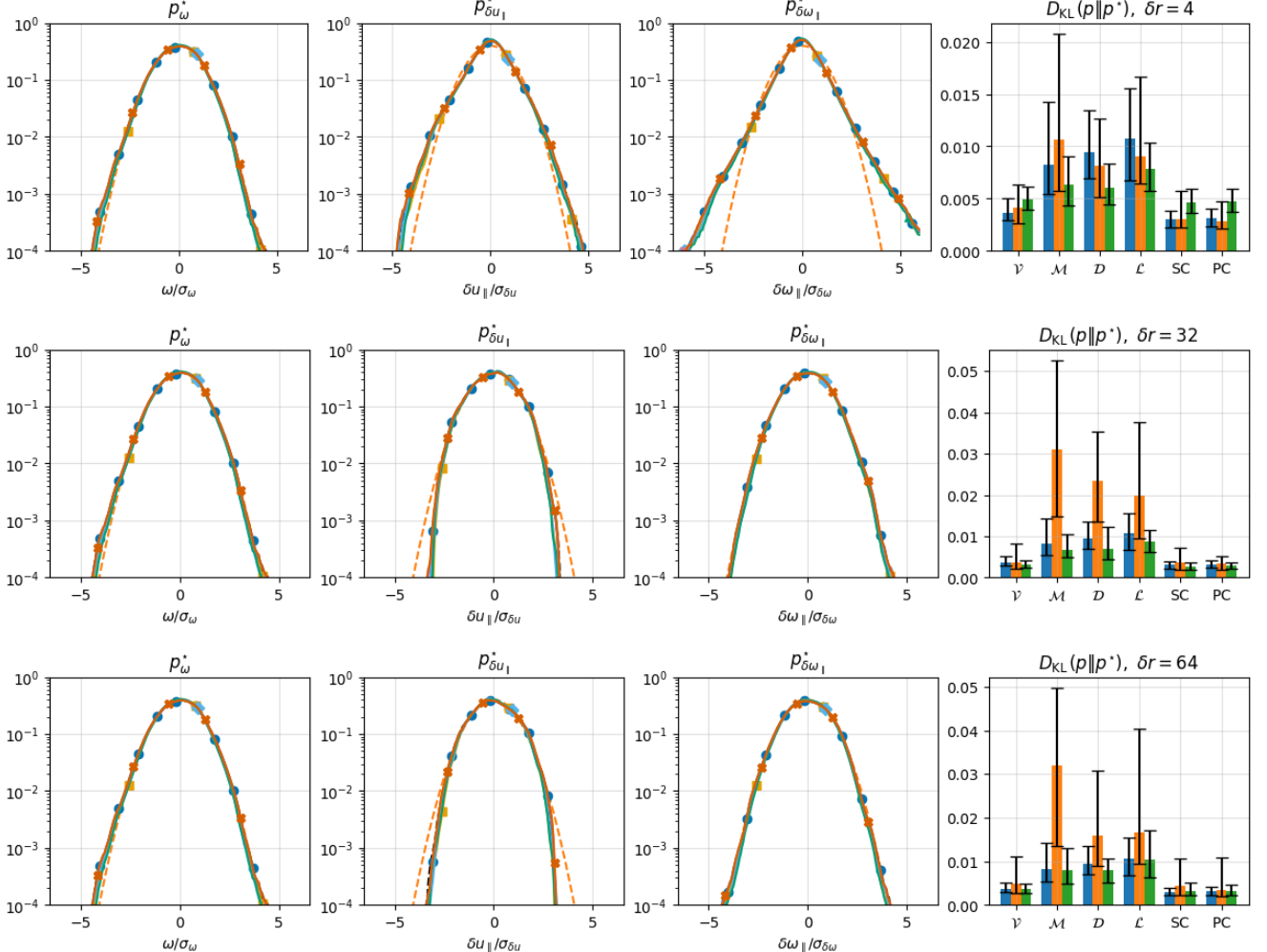


Figure H.14: Rollout predictions: empirical densities for $\delta r = 4$ (top row), $\delta r = 32$ (middle row), and $\delta r = 64$ (bottom row). First panel from left to right: empirical density $p_\omega^*(z; \delta r)$. Second panel: empirical density $p_{\delta u_\parallel}^*(z; \delta r)$. Third panel: empirical density $p_{\delta \omega_\parallel}^*(z; \delta r)$. Fourth panel: Kullback-Leibler divergences. Density plots legends: --- ground truth, - - - $\mathcal{N}(0, 1)$, (V) ●, (M) ■, (D) ◆, (L) ▲, (SC) ▽, (PC) ✕. Box plot legends: $D_{KL}(p_\omega \| p_\omega^*; \delta r)$ ■, $D_{KL}(p_{\delta u_\parallel} \| p_{\delta u_\parallel}^*; \delta r)$ ■, $D_{KL}(p_{\delta \omega_\parallel} \| p_{\delta \omega_\parallel}^*; \delta r)$ ■. Whiskers indicate the interquartile range.

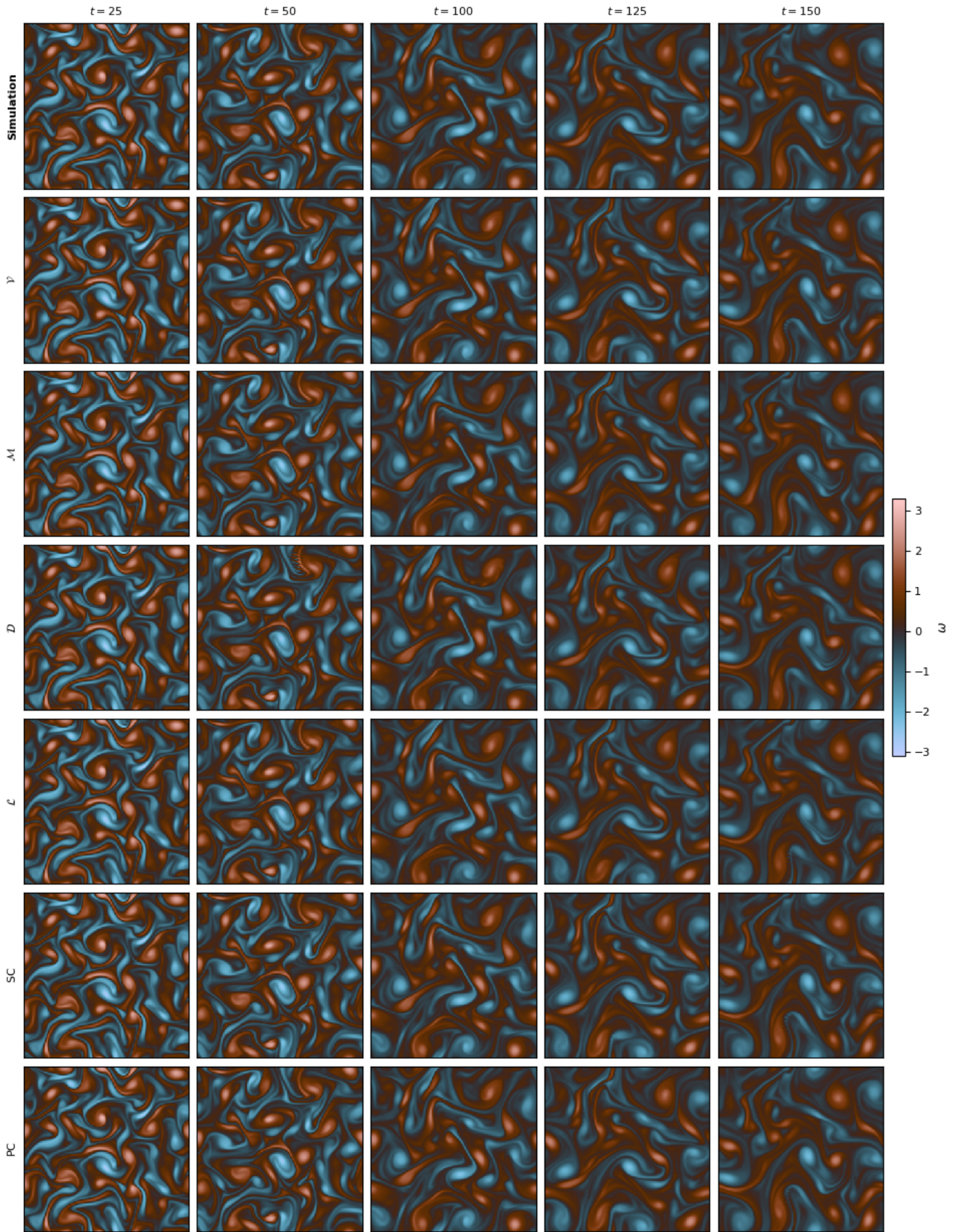


Figure H.15: Rollout predictions: snapshots of the ground-truth solution (vorticity, top row) against snapshots inferred by all models (\mathcal{V}) , (\mathcal{M}) , (\mathcal{D}) , (\mathcal{L}) , (SC), and (PC).

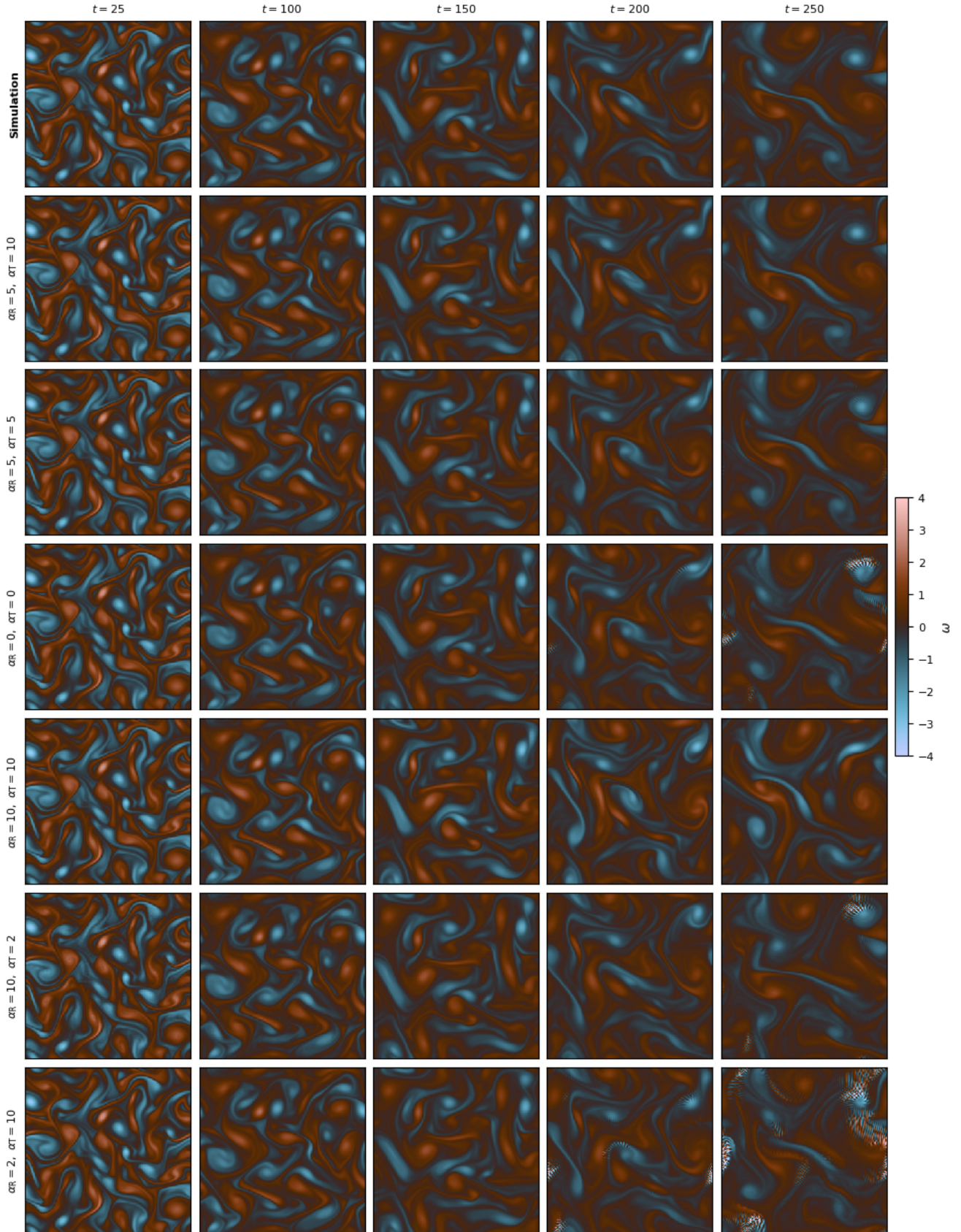


Figure H.16: Long rollout predictions: snapshots of the ground-truth solution (vorticity, top row) against snapshots inferred by diffusion model on divergence-free manifold (\mathcal{M}) using the transport-based corrector with different hyperparameters α_R and α_T . Small-scale rippling artifacts are observable at long horizons for $\alpha_R = \alpha_T = 0$ (forth row), $\alpha_R = 10$ and $\alpha_T = 2$ (sixth row), and $\alpha_R = 2$ and $\alpha_T = 10$ (seventh row).

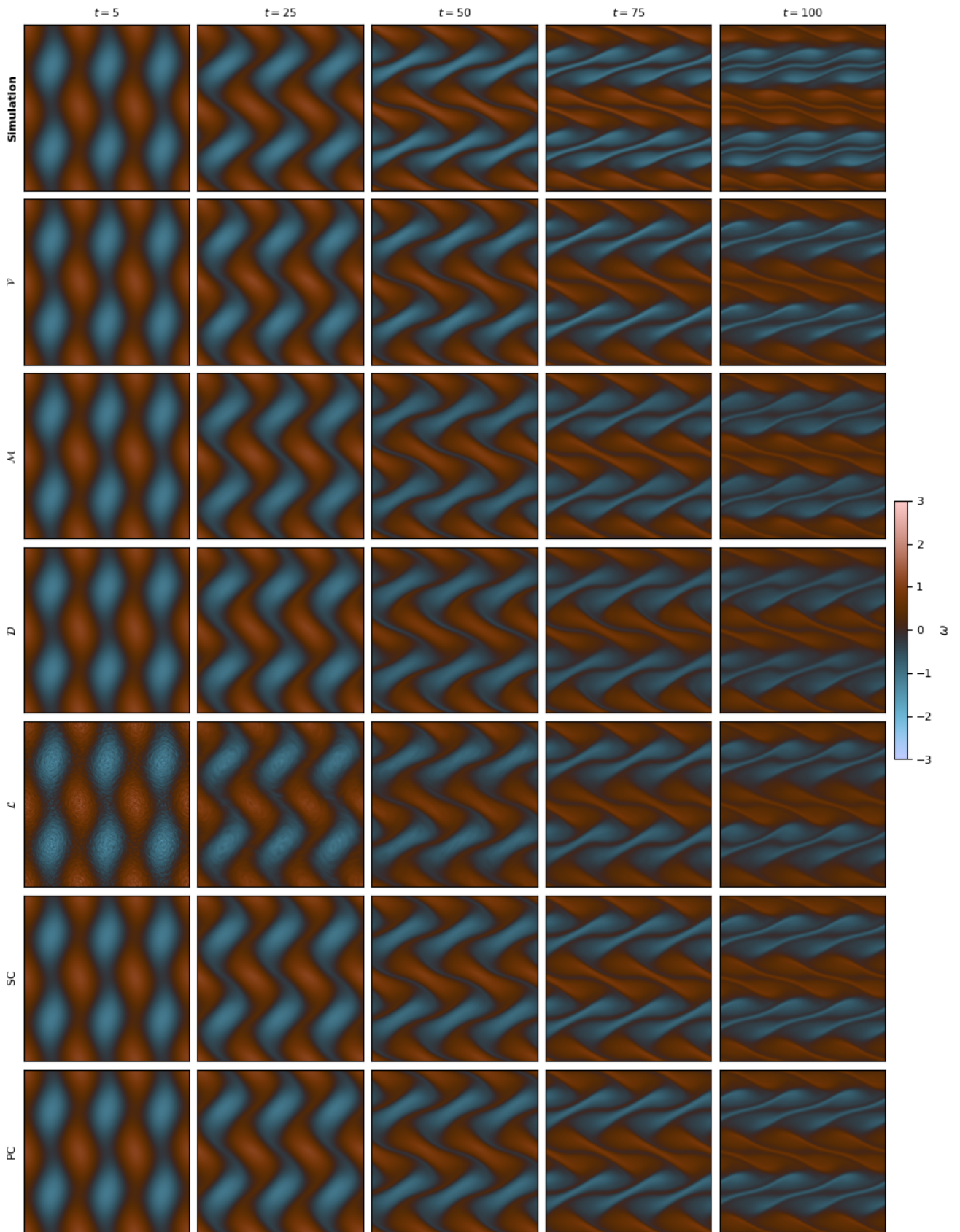


Figure I.17: OOD tests, VS case: snapshots of the ground-truth solution (vorticity, top row) against snapshots inferred by all models ((V) , (M) , (D) , (L) , (SC), and (PC)).

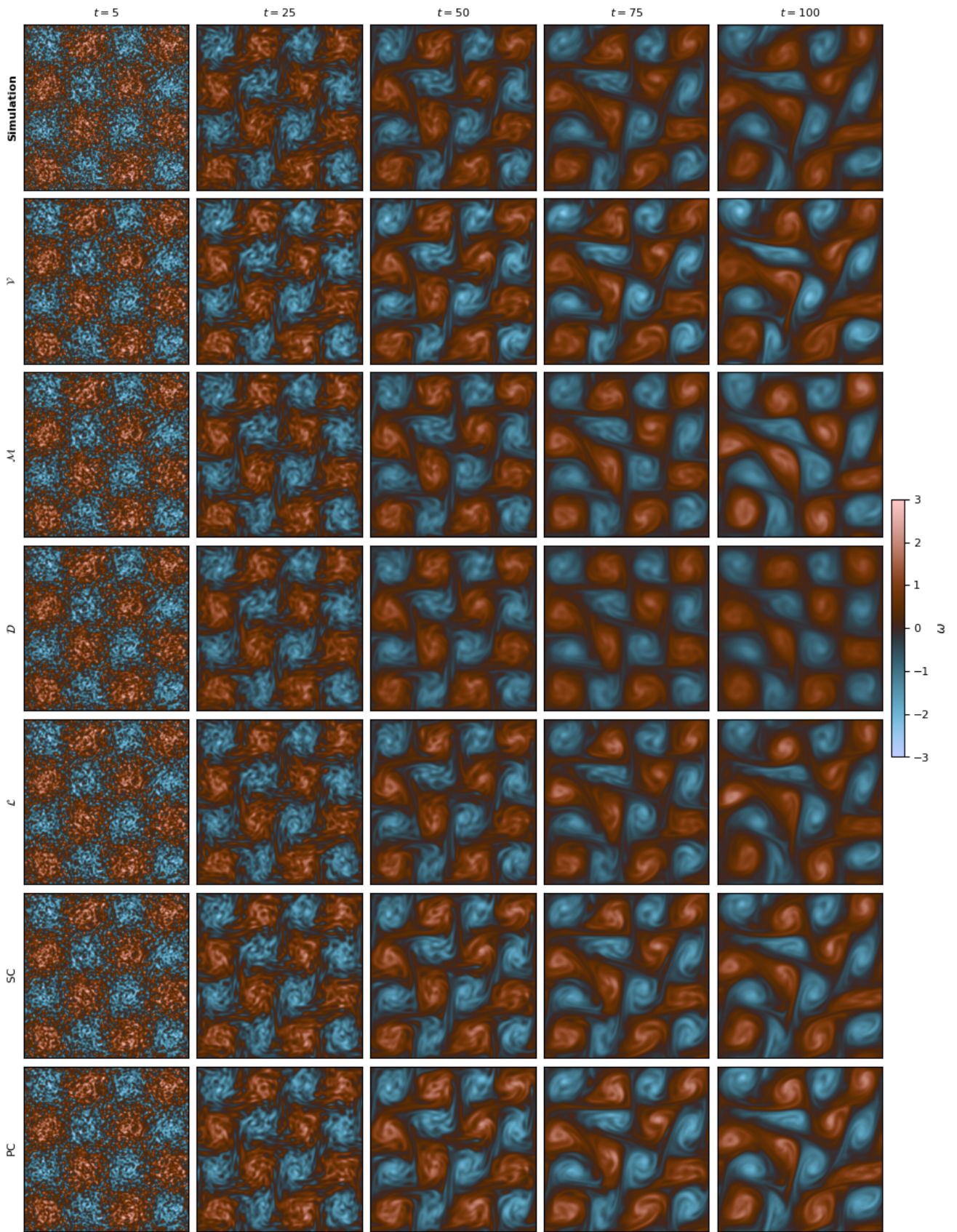


Figure I.18: OOD tests, TGV case: snapshots of the ground-truth solution (vorticity, top row) against snapshots inferred by all models (v), (M), (D), (L), (SC), and (PC).

References

- [1] Ciprian Foias, Oscar P. Manley, Ricardo Rosa, and Roger Temam. *Navier-Stokes Equations and Turbulence*, volume 83 of *Encyclopedia of Mathematics and its Applications*. Cambridge University Press, Cambridge, 2001. doi: 10.1017/CBO9780511546754.
- [2] Roger Temam. *Navier-Stokes Equations: Theory and Numerical Analysis*. AMS Chelsea Publishing, Providence RI, 2001.
- [3] James C. Robinson. The Navier-Stokes regularity problem. *Philosophical Transactions of the Royal Society A: Mathematical, Physical and Engineering Sciences*, 378(2174):20190526, 2020. doi: 10.1098/rsta.2019.0526.
- [4] Claudio Canuto, M. Yousuff Hussaini, Alfio Quarteroni, and Thomas A. Zang. *Spectral Methods in Fluid Dynamics*. Springer, Berlin, 1988. doi: 10.1007/978-3-642-84108-8.
- [5] Charles Hirsch. *Numerical Computation of Internal and External Flows*. Butterworth-Heinemann, Oxford, second edition, 2007. doi: 10.1016/B978-0-7506-6594-0.X5037-1.
- [6] Stephen B. Pope. *Turbulent Flows*. Cambridge University Press, Cambridge, first edition, 2000. doi: 10.1017/CBO9780511840531.
- [7] Alfio Quarteroni, Andrea Manzoni, and Federico Negri. *Reduced Basis Methods for Partial Differential Equations. An Introduction*. Springer, Cham, 2016. doi: 10.1007/978-3-319-15431-2.
- [8] Olivier P. Le Maître and Omar M. Knio. *Spectral Methods for Uncertainty Quantification. With Applications to Computational Fluid Dynamics*. Springer, Dordrecht, 2010. doi: 10.1007/978-90-481-3520-2.
- [9] Franco Flandoli. An introduction to 3D stochastic fluid dynamics. In *SPDE in Hydrodynamic: Recent Progress and Prospects*, volume 1942 of *Lecture Notes in Mathematics*, pages 51–150, Berlin, 2008. Springer. doi: 10.1007/978-3-540-78493-7_2.
- [10] Francis Bach. *Learning Theory from First Principles*. The MIT Press, Cambridge MA, 2024.
- [11] Carl Edward Rasmussen and Christopher K. I. Williams. *Gaussian Processes for Machine Learning*. The MIT Press, Cambridge MA, 2005.
- [12] Isaac Elias Lagaris, Aristidis C. Likas, and Dimitrios I. Fotiadis. Artificial neural networks for solving ordinary and partial differential equations. *IEEE Transactions on Neural Networks*, 9(5):987–1000, 1998. doi: 10.1109/72.712178.
- [13] Maziar Raissi, Paris Perdikaris, and George E. Karniadakis. Physics-informed neural networks: A deep learning framework for solving forward and inverse problems involving nonlinear partial differential equations. *Journal of Computational Physics*, 378:686–707, 2019. doi: 10.1016/j.jcp.2018.10.045.
- [14] Franco Scarselli, Marco Gori, Ah Chung Tsoi, Markus Hagenbuchner, and Gabriele Monfardini. The graph neural network model. *IEEE Transactions on Neural Networks*, 20(1):61–80, 2009. doi: 10.1109/TNN.2008.2005605.
- [15] Zongyi Li, Nikola Kovachki, Kamvar Azizzadenesheli, Burigede Liu, Kaushik Bhattacharya, Andrew Stuart, and Anima Anandkumar. Fourier neural operator for parametric partial differential equations. *arXiv:2010.08895*, 2021. URL <https://arxiv.org/abs/2010.08895>.
- [16] Tianping Chen and Hong Chen. Universal approximation to nonlinear operators by neural networks with arbitrary activation functions and its application to dynamical systems. *IEEE Transactions on Neural Networks*, 6(4):911–917, 1995. doi: 10.1109/72.392253.
- [17] Lu Lu, Pengzhan Jin, Guofei Pang, Zhongqiang Zhang, and George E. Karniadakis. Learning nonlinear operators via DeepONet based on the universal approximation theorem of operators. *Nature Machine Intelligence*, 3(3):218–229, 2021. doi: 10.1038/s42256-021-00302-5.
- [18] Karthik Duraisamy, Gianluca Iaccarino, and Heng Xiao. Turbulence modeling in the age of data. *Annual Review of Fluid Mechanics*, 51:357–377, 2019. doi: 10.1146/annurev-fluid-010518-040547.
- [19] Steven L. Brunton, Bernd R. Noack, and Petros Koumoutsakos. Machine learning for fluid mechanics. *Annual Review of Fluid Mechanics*, 52:477–508, 2020. doi: 10.1146/annurev-fluid-010719-060214.
- [20] Ian J. Goodfellow, Jean Pouget-Abadie, Mehdi Mirza, Bing Xu, David Warde-Farley, Sherjil Ozair, Aaron Courville, and Yoshua Bengio. Generative adversarial nets. *arXiv:1406.2661*, 2014. URL <https://arxiv.org/abs/1406.2661>.
- [21] Diederik P. Kingma and Max Welling. Auto-encoding variational Bayes. *arXiv:1312.6114*, 2013. URL <https://arxiv.org/abs/1312.6114>.
- [22] Jascha Sohl-Dickstein, Eric Weiss, Niru Maheswaranathan, and Surya Ganguli. Deep unsupervised learning using nonequilibrium thermodynamics. In *Proceedings of the 32nd International Conference on Machine Learning*, volume 37 of *Proceedings of Machine Learning Research*, pages 2256–2265, 2015.
- [23] Jonathan Ho, Ajay Jain, and Pieter Abbeel. Denoising diffusion probabilistic models. *Advances in Neural Information Processing Systems*, 33:6840–6851, 2020.

[24] John L. Lumley. The structures of inhomogeneous turbulent flow. In Akiva M. Yaglom and Valerian I. Tatarski, editors, *Atmospheric Turbulence and Radio Wave Propagation*, pages 166–178. Nauka, Moscow, 1967.

[25] Wilfried Genuist, Éric Savin, Filippo Gatti, and Didier Clouet. Autoregressive regularized score-based diffusion models for multi-scenarios fluid flow prediction. *arXiv:2505.24145*, 2025. URL <http://arxiv.org/abs/2505.24145>.

[26] Georg Kohl, Li-Wei Chen, and Nils Thuerey. Benchmarking autoregressive conditional diffusion models for turbulent flow simulation. *arXiv:2309.01745*, 2023. URL <https://arxiv.org/abs/2309.01745>.

[27] Parviz Moin and Krishnan Mahesh. Direct numerical simulation: A tool in turbulence research. *Annual Review of Fluid Mechanics*, 30(1):539–578, 1998. doi: 10.1146/annurev.fluid.30.1.539.

[28] Roland Schiestel and Bruno Chaouat. Turbulence modeling and simulation advances in CFD during the past 50 years. *Comptes Rendus. Mécanique*, 350(S1):23–51, 2022. doi: 10.5802/crmeca.114.

[29] Michele Buzzicotti. Data reconstruction for complex flows using AI: Recent progress, obstacles, and perspectives. *Europhysics Letters*, 142(2):23001, 2023. doi: 10.1209/0295-5075/acc88c.

[30] Mario Lino, Stathi Fotiadis, Anil A. Bharath, and Chris D. Cantwell. Current and emerging deep-learning methods for the simulation of fluid dynamics. *Proceedings of the Royal Society A: Mathematical, Physical and Engineering Sciences*, 479(2275):20230058, 2023. doi: 10.1098/rspa.2023.0058.

[31] Ricardo Vinuesa and Steven L. Brunton. Enhancing computational fluid dynamics with machine learning. *Nature Computational Science*, 2(6):358–366, 2022. doi: 10.1038/s43588-022-00264-7.

[32] George E. Karniadakis, Ioannis G Kevrekidis, Lu Lu, Paris Perdikaris, Sifan Wang, and Liu Yang. Physics-informed machine learning. *Nature Reviews Physics*, 3(6):422–440, 2021. doi: 10.1038/s42254-021-00314-5.

[33] Yang Song, Jascha Sohl-Dickstein, Diederik P. Kingma, Abhishek Kumar, Stefano Ermon, and Ben Poole. Score-based generative modeling through stochastic differential equations. *arXiv:2011.13456*, 2020. URL <https://arxiv.org/abs/2011.13456>.

[34] Ashish Vaswani, Noam Shazeer, Niki Parmar, Jakob Uszkoreit, Llion Jones, Aidan N. Gomez, Łukasz Kaiser, and Illia Polosukhin. Attention is all you need. *Advances in Neural Information Processing Systems*, 30, 2017.

[35] Jiaming Song, Chenlin Meng, and Stefano Ermon. Denoising diffusion implicit models. *arXiv:2010.02502*, 2020. URL <https://arxiv.org/abs/2010.02502>.

[36] Yang Song and Stefano Ermon. Generative modeling by estimating gradients of the data distribution. *Advances in Neural Information Processing Systems*, 32, 2019.

[37] Brian D. O. Anderson. Reverse-time diffusion equation models. *Stochastic Processes and their Applications*, 12(3):313–326, 1982.

[38] Ulrich G. Haussmann and Étienne Pardoux. Time reversal of diffusions. *The Annals of Probability*, 14(4):1188–1205, 1986. doi: 10.1214/aop/1176992362.

[39] Sitan Chen, Sinho Chewi, Holden Lee, Yuanzhi Li, Jianfeng Lu, and Adil Salim. The probability flow ODE is provably fast. *Advances in Neural Information Processing Systems*, 36:68552–68575, 2023.

[40] Tero Karras, Miika Aittala, Timo Aila, and Samuli Laine. Elucidating the design space of diffusion-based generative models. *Advances in Neural Information Processing Systems*, 35:26565–26577, 2022.

[41] Diederik Kingma, Tim Salimans, Ben Poole, and Jonathan Ho. Variational diffusion models. *Advances in Neural Information Processing Systems*, 34:21696–21707, 2021.

[42] Alexander Quinn Nichol and Prafulla Dhariwal. Improved denoising diffusion probabilistic models. In *Proceedings of the 38th International Conference on Machine Learning*, volume 139 of *Proceedings of Machine Learning Research*, pages 8162–8171, 2021.

[43] Jonathan Ho and Tim Salimans. Classifier-free diffusion guidance. *arXiv:2207.12598*, 2022. URL <https://arxiv.org/abs/2207.12598>.

[44] Aliaksandra Shysheya, Cristiana Diaconu, Federico Bergamin, Paris Perdikaris, José Miguel Hernández-Lobato, Richard Turner, and Emile Mathieu. On conditional diffusion models for PDE simulations. *Advances in Neural Information Processing Systems*, 37:23246–23300, 2024.

[45] Tim Salimans and Jonathan Ho. Progressive distillation for fast sampling of diffusion models. *arXiv:2202.00512*, 2022. URL <https://arxiv.org/abs/2202.00512>.

[46] Yang Song, Prafulla Dhariwal, Mark Chen, and Ilya Sutskever. Consistency models. *arXiv:2303.01469*, 2023. URL <https://arxiv.org/abs/2303.01469>.

[47] Yusuke Tashiro, Jiaming Song, Yang Song, and Stefano Ermon. CSDI: Conditional score-based diffusion models for probabilistic time series imputation. *Advances in Neural Information Processing Systems*, 34:24804–24816, 2021.

[48] Juan Miguel Lopez Alcaraz and Nils Strothoff. Diffusion-based time series imputation and forecasting with structured state space models. *arXiv:2208.09399*, 2022. URL <https://arxiv.org/abs/2208.09399>.

[49] Kashif Rasul, Calvin Seward, Ingmar Schuster, and Roland Vollgraf. Autoregressive denoising diffusion models for multivariate probabilistic time series forecasting. In *Proceedings of the 38th International Conference on Machine Learning*, volume 139 of *Proceedings of Machine Learning Research*, pages 8857–8868, 2021.

[50] Valentin De Bortoli, James Thornton, Jeremy Heng, and Arnaud Doucet. Diffusion Schrödinger bridge with applications to score-based generative modeling. *Advances in Neural Information Processing Systems*, 34:17695–17709, 2021.

[51] Yang Song, Liyue Shen, Lei Xing, and Stefano Ermon. Solving inverse problems in medical imaging with score-based generative models. *arXiv:2111.08005*, 2021. URL <https://arxiv.org/abs/2111.08005>.

[52] Hyungjin Chung, Jeongsol Kim, Michael T. Mccann, Marc L. Klasky, and Jong Chul Ye. Diffusion posterior sampling for general noisy inverse problems. *arXiv:2209.14687*, 2022. URL <https://arxiv.org/abs/2209.14687>.

[53] Xingyu Xu and Yuejie Chi. Provably robust score-based diffusion posterior sampling for plug-and-play image reconstruction. *Advances in Neural Information Processing Systems*, 37:36148–36184, 2024.

[54] Yunpeng Wang, Zhijie Li, Zelong Yuan, Wenhui Peng, Tianyuan Liu, and Jianchun Wang. Prediction of turbulent channel flow using Fourier neural operator-based machine-learning strategy. *Physical Review Fluids*, 9(8):084604, 2024. doi: 10.1103/PhysRevFluids.9.084604.

[55] Jaideep Pathak, Shashank Subramanian, Peter Harrington, Sanjeev Raja, Ashesh Chattopadhyay, Morteza Mardani, Thorsten Kurth, David Hall, Zongyi Li, Kamyar Azizzadenesheli, et al. FourCastNet: A global data-driven high-resolution weather model using adaptive Fourier neural operators. *arXiv:2202.11214*, 2022. URL <https://arxiv.org/abs/2202.11214>.

[56] Ryan Keisler. Forecasting global weather with graph neural networks. *arXiv:2202.07575*, 2022. URL <https://arxiv.org/abs/2202.07575>.

[57] Remi Lam, Alvaro Sanchez-Gonzalez, Matthew Willson, Peter Wirnsberger, Meire Fortunato, Ferran Alet, Suman Ravuri, Timo Ewalds, Zach Eaton-Rosen, Weihua Hu, Alexander Merose, Stephan Hoyer, George Holland, Oriol Vinyals, Jacklynn Stott, Alexander Pritzel, Shakir Mohamed, and Peter Battaglia. Learning skillful medium-range global weather forecasting. *Science*, 382(6677):1416–1421, 2023. doi: 10.1126/science.adi2336.

[58] Mohammed Sardar, Alex Skillen, Samuel Draycott, and Alistair Revell. Spectrally decomposed diffusion models for generative turbulence recovery. *Physics of Fluids*, 36(11):115179, 2024. doi: 10.1063/5.0231664.

[59] Marten Lienen, David Lüdke, Jan Hansen-Palmus, and Stephan Günnemann. From zero to turbulence: Generative modeling for 3D flow simulation. *arXiv:2306.01776*, 2023. URL <https://arxiv.org/abs/2306.01776>.

[60] Jing Qiu, Jiancheng Huang, Xiangdong Zhang, Zeng Lin, Minglei Pan, Zengding Liu, and Fen Miao. Pi-fusion: Physics-informed diffusion model for learning fluid dynamics. *arXiv:2406.03711*, 2024. URL <https://arxiv.org/abs/2406.03711>.

[61] Dule Shu, Zijie Li, and Amir Barati Farimani. A physics-informed diffusion model for high-fidelity flow field reconstruction. *Journal of Computational Physics*, 478:111972, 2023. doi: 10.1016/j.jcp.2023.111972.

[62] Salvatore Cuomo, Vincenzo Schiano Di Cola, Fabio Giampaolo, Gianluigi Rozza, Maziar Raissi, and Francesco Piccialli. Scientific machine learning through physics-informed neural networks: Where we are and what's next. *Journal of Scientific Computing*, 92(3):88, 2022. doi: 10.1007/s10915-022-01939-z.

[63] Taco Cohen and Max Welling. Group equivariant convolutional networks. In *Proceedings of the 33rd International Conference on Machine Learning*, volume 48 of *Proceedings of Machine Learning Research*, pages 2990–2999, 2016.

[64] Michael M. Bronstein, Joan Bruna, Taco Cohen, and Petar Veličković. Geometric deep learning: Grids, groups, graphs, geodesics, and gauges. *arXiv:2104.13478*, 2021. URL <https://arxiv.org/abs/2104.13478>.

[65] Samuel Greydanus, Misko Dzamba, and Jason Yosinski. Hamiltonian neural networks. *Advances in Neural Information Processing Systems*, 32:15379–15389, 2019.

[66] Valentin De Bortoli, Emile Mathieu, Michael Hutchinson, James Thornton, Yee Whye Teh, and Arnaud Doucet. Riemannian score-based generative modelling. *Advances in Neural Information Processing Systems*, 35:2406–2422, 2022.

[67] Chin-Wei Huang, Milad Aghajohari, Joey Bose, Prakash Panangaden, and Aaron C. Courville. Riemannian diffusion models. *Advances in Neural Information Processing Systems*, 35:2750–2761, 2022.

[68] Jae Hyun Lim, Nikola B. Kovachki, Ricardo Baptista, Christopher Beckham, Kamyar Azizzadenesheli, Jean Kossaifi, Vikram Voleti, Jiaming Song, Karsten Kreis, Jan Kautz, Christopher Pal, Arash Vahdat, and Anima Anandkumar. Score-based diffusion models in function space. *Journal of Machine Learning Research*, 26(158):1–62, 2025.

[69] Sifan Wang, Zehao Dou, Siming Shan, Tong-Rui Liu, and Lu Lu. FunDiff: Diffusion models over function spaces for physics-informed generative modeling. *arXiv:2506.07902*, 2025. URL <https://arxiv.org/abs/2506.07902>.

[70] Jack Richter-Powell, Yaron Lipman, and Ricky T. Q. Chen. Neural conservation laws: A divergence-free perspective. *Advances in Neural Information Processing Systems*, 35:38075–38088, 2022.

[71] Chiyu "Max" Jiang, Karthik Kashinath, Prabhat, and Philip Marcus. Enforcing hard physical constraints in CNNs through differentiable PDE layer. In *8th International Conference on Learning Representations, ICLR 2020–Workshop on Integration of Deep Neural Models and Differential Equations*, 2020.

[72] Ahmed A. Elhag, Yuyang Wang, Joshua M. Susskind, and Miguel Angel Bautista. Manifold diffusion fields. *arXiv:2305.15586*, 2023. URL <https://arxiv.org/abs/2305.15586>.

[73] Siming Shan, Pengkai Wang, Song Chen, Jiaxu Liu, Chao Xu, and Shengze Cai. PiRD: Physics-informed residual diffusion for flow field reconstruction. *arXiv:2404.08412*, 2024. URL <https://arxiv.org/abs/2404.08412>.

[74] Vivek Oommen, Aniruddha Bora, Zhen Zhang, and George E. Karniadakis. Integrating neural operators with diffusion models improves spectral representation in turbulence modeling. *Proceedings of the Royal Society A*, 481(2309):20240819, 2025. doi: 10.1098/rspa.2024.0819.

[75] Tim Whittaker, Romuald A. Janik, and Yaron Oz. Turbulence scaling from deep learning diffusion generative models. *Journal of Computational Physics*, 514:113239, 2024. doi: 10.1016/j.jcp.2024.113239.

[76] Marc Amorós-Trepat, Luis Medrano-Navarro, Qiang Liu, Luca Guastoni, and Nils Thuerey. Guiding diffusion models to reconstruct flow fields from sparse data. *arXiv:2510.19971*, 2025. URL <https://arxiv.org/abs/2510.19971>.

[77] Omer Rochman and Gilles Louppe. Enforcing governing equation constraints in neural PDE solvers via training-free projections. *arXiv:2511.17258*, 2025. URL <https://arxiv.org/abs/2511.17258>.

[78] Vivek Jayaram, Ira Kemelmacher-Shlizerman, Steve Seitz, and John Thickstun. Linearly constrained diffusion implicit models. In *39th Annual Conference on Neural Information Processing Systems (NeurIPS 2025)*, 2025.

[79] Guido Boffetta and Stefano Musacchio. Evidence for the double cascade scenario in two-dimensional turbulence. *Physical Review E*, 82(1):016307, 2010. doi: 10.1103/PhysRevE.82.016307.

[80] Guido Boffetta and Robert E. Ecke. Two-dimensional turbulence. *Annual Review of Fluid Mechanics*, 44:427–451, 2012. doi: 10.1146/annurev-fluid-120710-101240.

[81] Emil J. Hopfinger. Turbulence in stratified fluids: A review. *Journal of Geophysical Research: Oceans*, 92(C5):5287–5303, 1987. doi: 10.1029/JC092iC05p05287.

[82] Uriel Frisch and Andrei Nikolaevich Kolmogorov. *Turbulence: the legacy of A.N. Kolmogorov*. Cambridge University Press, Cambridge, 1995. doi: 10.1017/CBO9781139170666.

[83] Pascal Vincent. A connection between score matching and denoising autoencoders. *Neural Computation*, 23(7):1661–1674, 2011. doi: 10.1162/NECO_a_00142.

[84] Yang Song and Stefano Ermon. Improved techniques for training score-based generative models. *Advances in Neural Information Processing Systems*, 33:12438–12448, 2020.

[85] Dongjun Kim, Seungjae Shin, Kyungwoo Song, Wanmo Kang, and Il Chul Moon. Soft truncation: A universal training technique of score-based diffusion model for high precision score estimation. In *Proceedings of the 39th International Conference on Machine Learning*, volume 162 of *Proceedings of Machine Learning Research*, pages 11201–11228, 2022.

[86] Bradley Efron. Tweedie's formula and selection bias. *Journal of the American Statistical Association*, 106(496):1602–1614, 2011. doi: 10.1198/jasa.2011.tm11181.

[87] Olaf Ronneberger, Philipp Fischer, and Thomas Brox. U-Net: Convolutional networks for biomedical image segmentation. In *Medical Image Computing and Computer-Assisted Intervention–MICCAI 2015: 18th International Conference, Munich, Germany, October 5–9, 2015, Proceedings, part III 18*, pages 234–241. Springer, Cham, 2015. doi: 10.1007/978-3-319-24574-4_28.

[88] Özgün Çiçek, Ahmed Abdulkadir, Soeren S. Lienkamp, Thomas Brox, and Olaf Ronneberger. 3D U-Net: Learning dense volumetric segmentation from sparse annotation. In *Medical Image Computing and Computer-Assisted Intervention–MICCAI 2016: 19th International Conference, Athens, Greece, October 17–21, 2016, Proceedings, Part II 19*, pages 424–432. Springer, Cham, 2016. doi: 10.1007/978-3-319-46723-8_49.

[89] Uri M. Ascher and Linda R. Petzold. *Computer Methods for Ordinary Differential Equations and Differential-Algebraic Equations*. SIAM, Philadelphia PA, 1998. doi: 10.1137/1.9781611971392.

[90] Alexia Jolicoeur-Martineau, Ke Li, Rémi Piché-Taillefer, Tal Kachman, and Ioannis Mitliagkas. Gotta go fast when generating data with score-based models. *arXiv:2105.14080*, 2021. URL [http://arxiv.org/abs/2105.14080](https://arxiv.org/abs/2105.14080).

[91] Arthur Stéphanovitch, Eddie Aamari, and Clément Levraud. Generalization bounds for score-based generative models: a synthetic proof. *arXiv:2507.04794*, 2025. URL [http://arxiv.org/abs/2507.04794](https://arxiv.org/abs/2507.04794).

[92] Prafulla Dhariwal and Alexander Nichol. Diffusion models beat GANs on image synthesis. *Advances in Neural Information Processing Systems*, 34:8780–8794, 2021.

[93] Ilan Price, Alvaro Sanchez-Gonzalez, Ferran Alet, Tom R. Andersson, Andrew El-Kadi, Dominic Masters, Timo Ewalds, Jacklynn Stott, Shakir Mohamed, Peter Battaglia, Remi Lam, and Matthew Willson. Probabilistic weather forecasting with machine learning. *Nature*, 637:84–90, 2025. doi: 10.1038/s41586-024-08252-9.

[94] Ethan Perez, Florian Strub, Harm de Vries, Vincent Dumoulin, and Aaron C. Courville. FiLM: Visual reasoning with a general conditioning layer. *arXiv:1709.07871*, 2017. URL <http://arxiv.org/abs/1709.07871>.

[95] Xiaowei Jin, Shengze Cai, Hui Li, and George E. Karniadakis. NSFnets (Navier-Stokes flow nets): Physics-informed neural networks for the incompressible Navier-Stokes equations. *Journal of Computational Physics*, 426:109951, 2021. doi: 10.1016/j.jcp.2020.109951.

[96] Simon Benaïchouche, Guillaume Morel, François Rousseau, and Ronan Fablet. Divergence-free continuous normalizing flows for uncertainty quantification. *hal-03813499*, 2022. URL <https://hal.science/hal-03813499>.

[97] Nikolaj T. Mücke and Benjamin Sanderse. Physics-aware generative models for turbulent fluid flows through energy-consistent stochastic interpolants. *arXiv:2504.05852*, 2025. URL <https://arxiv.org/abs/2504.05852>.

[98] Martin Schiødt, Nikolaj T. Mücke, and Clara M. Velte. Generative super-resolution of turbulent flows via stochastic interpolants. *arXiv:2508.13770*, 2025. URL <http://arxiv.org/abs/2508.13770>.

[99] Matilde Valente, Tiago C. Dias, Vasco Guerra, and Rodrigo Ventura. Physics-consistent machine learning with output projection onto physical manifolds. *Communications Physics*, 8:433, 2025. doi: 10.1038/s42005-025-02329-1.

[100] Mengtian Li, Ersin Yumer, and Deva Ramanan. Budgeted training: Rethinking deep neural network training under resource constraints. *arXiv:1905.04753*, 2019. URL <https://arxiv.org/abs/1905.04753>.

[101] Giulio Biroli, Tony Bonnaire, Valentin De Bortoli, and Marc Mézard. Dynamical regimes of diffusion models. *Nature Communications*, 15(1):9957, 2024. doi: 10.1038/s41467-024-54281-3.

[102] Yves Dubief and Franck Delcayre. On coherent-vortex identification in turbulence. *Journal of Turbulence*, 1(11):011, 2000. doi: 10.1088/1468-5248/1/1/011.

[103] Aapo Hyvärinen. A noise-corrected Langevin algorithm and sampling by half-denoising. *arXiv:2410.05837*, 2024. URL <https://arxiv.org/abs/2410.05837>.

[104] Peter E. Kloeden and R. A. Pearson. The numerical solution of stochastic differential equations. *The ANZIAM Journal*, 20(1):8–12, 1977. doi: 10.1017/S0334270000001405.

[105] Francis Filbet and Charles Prouleur. High order time discretization for backward semi-Lagrangian methods. *Journal of Computational and Applied Mathematics*, 303:171–188, 2016. doi: 10.1016/j.cam.2016.01.024.

[106] Leonid I. Rudin, Stanley Osher, and Emad Fatemi. Nonlinear total variation based noise removal algorithms. *Physica D: Nonlinear Phenomena*, 60(1-4):259–268, 1992. doi: 10.1016/0167-2789(92)90242-F.

[107] Thomas Brox, Andrés Bruhn, Nils Papenberg, and Joachim Weickert. High accuracy optical flow estimation based on a theory for warping. In Tomás Pajdla and Jiří Matas, editors, *Computer Vision – ECCV 2004*, volume 3024 of *Lecture Notes in Computer Science*, pages 25–36. Springer, Berlin, 2004. doi: 10.1007/978-3-540-24673-2_3.

[108] Giuseppe Da Prato and Jerzy Zabczyk. *Stochastic Equations in Infinite Dimensions*, volume 152 of *Encyclopedia of Mathematics and its Applications*. Cambridge University Press, Cambridge, 2014. doi: 10.1017/CBO9781107295513.

[109] Claudia Prévôt and Michael Röckner. *A Concise Course on Stochastic Partial Differential Equations*. Springer, Berlin, 2007. doi: 10.1007/978-3-540-70781-3.

[110] Hannelore Breckner. Galerkin approximation and the strong solution of the Navier-Stokes equation. *Journal of Applied Mathematics and Stochastic Analysis*, 13(3):239–259, 2000. doi: 10.1155/S1048953300000228.